TU Braunschweig Niedersächsisches Forschungszentrum
für Luftfahrt

Berichte aus der Luft- und Raumfahrttechnik

Forschungsbericht 2016-11

Design of Efficient High-Lift Configurations with Coanda Flaps

Marco Burnazzi

TU Braunschweig
Institut für Strömungsmechanik

Diese Arbeit erscheint gleichzeitig als von der Fakultät für Maschinenbau der Technischen Universität Carolo-Wilhelmina zu Braunschweig zur Erlangung des akademischen Grades eines Doktor-Ingenieurs genehmigte Dissertation.

Diese Arbeit erscheint gleichzeitig als von der Fakultät für Maschinenbau der Technischen Universität Carolo-Wilhelmina zu Braunschweig zur Erlangung des akademischen Grades eines Doktor-Ingenieurs genehmigte Dissertation.

Herausgeber der NFL Forschungsberichte:
TU Braunschweig - Niedersächsisches Forschungszentrum für Luftfahrt
Hermann-Blenk-Straße 27 • 38108 Braunschweig
Tel: 0531-391-9822 • Fax: 0531-391-9804
Mail: nfl@tu-braunschweig.de
Internet: www.tu-braunschweig.de/nfl

Design of Efficient High-Lift Configurations with Coanda Flaps

Bei der Fakultät für Maschinenbau
der Technischen Universität Carolo-Wilhelmina zu Braunschweig

zur Erlangung der Würde
eines Doktor-Ingenieurs (Dr.-Ing.)
genehmigte Dissertation

von:	Marco Burnazzi
aus (Geburtsort):	Rimini

eingereicht am:	17. September 2015
mündliche Prüfung am:	2. März 2016
Gutachter:	Prof. Dr.-Ing. Rolf Radespiel Prof. Dr.-Ing. habil. Cord-Christian Rossow

2015

Abstract

Active flow control applied to high-lift systems is a promising solution to improve low-speed flight capabilities and reduce noise emissions of commercial aircraft. However, too high power requirements in relation to the achieved lift gains have prevented active high-lift systems from being largely employed in the aeronautical industry. In this context, this work develops technologies to enhance the aerodynamic efficiency of an active high-lift system by means of RANS numerical simulations. The transonic airfoil DLR-F15 is equipped with an active internally-blown flap, which consists of a thin air jet tangentially blown over the shoulder of a simple-hinged flap deflected by 65°. To improve the lift generated by the airfoil, the effects of a flexible droop-nose device, wall suction and unsteady blowing are investigated. The fundamentals of gap-less droop-nose design are presented, describing the aerodynamic sensitivities of the main geometrical parameters and the physical phenomena that determine the lift performance. The efficiency of the resulting droop-nose configuration is also tested on a wing-body aircraft model. The analysis reveals three-dimensional flow mechanisms that limit the lift performance in operative conditions. The airfoil efficiency is then further improved by adding a boundary-layer suction device. The effects of shape and location of the suction slot are studied to maximize the lift coefficient and pressure recovery. Finally, the effectiveness of unsteady excitation of the mixing layer by means of dynamic blowing is investigated. As a final result, a target maximum lift coefficient of 5.0 can be achieved with a 43% lower jet-momentum coefficient with respect to the baseline airfoil configuration.

Übersicht

Die Anwendung von aktiver Strömungskontrolle bei Hochauftriebssystemen ist eine vielversprechende Lösung, um die Langsamflugeigenschaften eines Verkehrsflugzeugs zu verbessern und die Lärmemissionen zu verringern. Bislang verhindert jedoch das zu geringe Verhältnis aus erzielbarem Auftriebsgewinn und eingesetztem Impuls des Ausblasens eine breite Anwendung von aktiven Hochauftriebssystemen in der Luftfahrtindustrie. Vor diesem Hintergrund werden in der vorliegenden Arbeit mit Hilfe von numerischen Strömungssimulationen neue Technologien entwickelt, um die Effizienz eines aktiven Hochauftriebssystems zu verbessern. Hierzu wird das transsonische Profil DLR-F15 mit einer angeblasenen Coanda Klappe ausgestattet, die aus einem dünnen, tangential ausgeblasenen Strahl auf der Oberseite der um 65° ausgeschlagenen Klappe besteht. Um den resultierenden Auftrieb zu erhöhen, werden die Effekte einer formadaptiven Senknase, von Wandabsaugung und einer dynamischen Ausblasung quantifiziert. Durch eine aerodynamische Sensitivitätsanalyse bezüglich der wesentlichen geometrischen Parameter sowie durch eine Beschreibung der physikalischen Phänomene, die für die Auftriebserzeugung verantwortlich sind, werden die Entwurfsgrundlagen für spaltlose Senknasen herausgearbeitet. Die Leistungsfähigkeit der resultierenden Senknase wird zudem an einer vollständigen Flügel-Rumpf-Konfiguration erprobt. Die Untersuchung ihres Überziehverhaltens zeigt zusätzliche drei-dimensionale Strömungsmechanismen, welche den Auftrieb unter Betriebsbedingungen beschränken. Mit Hilfe von Grenzschichtabsaugung kann der Profilwirkungsgrad weiter erhöht werden. Die Einflüsse der Absaugeposition und der Absaugegeometrie werden analysiert, um den Auftriebsbeiwert und den Druckrückgewinn am Ende des Einlasskanals zu maximieren. Schließlich wird die Wirksamkeit einer instationären Anregung der Mischungsschicht durch dynamisch aktuiertes Ausblasen untersucht. Als abschließendes Ergebnis kann der Zielauftriebsbeiwert von 5.0 mit einem um 43% verringerten Strahlimpuls im Vergleich zur Referenzkonfiguration erreicht werden.

Acknowledgements

Writing this thesis has been a long and exciting journey. The four years I spent working on my doctoral project passed faster than I could have ever imagined, chasing deadlines, delivering data and preparing talks. Looking back at these years I see an incredibly rich picture made of people, events, frustration and rewarding achievements that covers all aspects of my personal and professional life.

Foremost I would like to sincerely thank my doctoral supervisor, Professor Rolf Radespiel, who decided to believe in a disoriented Italian student in a rainy Autumn day five years ago. Surrounded by a complete new environment I started working on a promising project, along with many experienced colleagues who supported me since the very beginning and made possible the completion of this thesis. The Institut für Strömungsmechanik and the entire research group of the center SFB 880 provided the perfect working environment for me to find the necessary motivation and inspiration to face the scientific and personal challenges I had ahead of me. The funding of the project by the German Research Foundation, DFG, made all this possible and is thankfully acknowledged. I am particularly thankful to the Institute Secretary, Jennifer, whose help was essential in uncountable occasions to find my way in the swampy German bureaucracy.

The office atmosphere, together with the motivation to pursue the project goals is what made me leave bed in cold German winter days. In this respect I am profoundly grateful to my office colleagues Michael and Robin. The countless scientific discussions with them and the other colleagues of the Institute were a constant source of motivation and intellectual growth.

The opportunity to spend five months at NASA Langley was an undoubted highlight of these years. For the excellent scientific and personal exchange I would like to thank Catherine McGinley, Brian Allan and all the other members of the Flow Physics and Control Branch who welcomed me and made me feel part of their team. A special thanks also to all the others who with their friendship made of those months a memorable experience.

Nevertheless, the professional achievements would have been simply impossible without the support of an extraordinary team outside of the working environment. Everyday life in a foreign country can be either an amazing experience or a struggling one. In my case, well, it went beyond any possible hope and expectation. Everyday, for all these years, I have been surrounded by friends who have shared with me unforgivable moments. Their constant presence and the uncountable adventures we went through together made Braunschweig my home. I would like to specially thank my girlfriend Aida, who shared with me my achievements and gave me motivation and strength during the difficult moments with her invaluable constant support. Finally, I am sincerely thankful to my family that has been always present at my side.

Braunschweig, 2015.

Contents

Nomenclature

Latin Symbols

b	[m]	Wing span
c	[m]	Airfoil chord length in cruise configuration
C_{Fx}	[-]	Friction coefficient in x direction
C_L	[-]	Lift coefficient
C_D	[-]	Drag coefficient
C_M	[-]	Pitching moment coefficient
C_p	[-]	Pressure coefficient
C_v	$[\mathrm{J\,kg^{-1}\,K^{-1}}]$	Specific heat coefficient at constant volume
C_μ	[-]	Jet momentum coefficient
$\underline{E}$	$[\mathrm{m^2\,s^{-2}}]$	Total specific energy
$\overline{\overline{F}}$		Flux density tensor
F^+	[-]	Non dimensional signal frequency
F_j	[N]	Thrust generated by the Coanda jet
H	$[\mathrm{m^2\,s^{-2}}]$	Enthalpy
h	[m]	Coordinate normal to the local surface
h_s	[m]	Blowing slot height
$h_{\mathrm{s_{ref}}}$	[m]	Reference blowing slot height
k	$[\mathrm{m^2\,s^{-2}}]$	Turbulent kinetic energy
L_f	[m]	Flap length
L_n	[m]	Nose length
M	[-]	Mach number
$\dot{m}_\mathrm{j}$	$[\mathrm{kg\,s^{-1}}]$	Jet mass flow
$\vec{n}$		Unit vector normal to the local surface
p	$[\mathrm{N\,m^{-2}}]$	Pressure
$\vec{q}$	$[\mathrm{W\,m^{-2}}]$	Heat flux density vector
q_∞	$[\mathrm{N\,m^{-2}}]$	Dynamic pressure under freestream conditions
R	$[\mathrm{J\,kg^{-1}\,K^{-1}}]$	Specific gas constant
Re	[-]	Reynolds number
S	[m]	External surface of the control volume
$\widetilde{S}$		Strain rate tensor
S_ref	[m]	Reference surface
T	[K]	Temperature
t	[-]	Dimensionless time
U	$[\mathrm{m\,s^{-1}}]$	Magnitude of the velocity vector
$\vec{U}$		Velocity vector
u, v, w	$[\mathrm{m\,s^{-1}}]$	Components of the velocity vector
V	$[\mathrm{m^3}]$	Control volume
$\vec{W}$		Vector of conservative variables
y^+	[-]	Dimensionless wall spacing

Greek Symbols

α	$[^\circ]$	Angle of attack
Γ	$[\mathrm{m^2\,s^{-1}}]$	Circulation
δ	$[^\circ]$	Flap deflection angle
δ_2	[m]	Boundary layer momentum thickness
ϵ	$[\mathrm{m^2\,s^3}]$	Turbulent dissipation per unit mass
ζ	$[\mathrm{m^2\,s^{-1}}]$	Turbulent Enstrophy
η	[-]	Dimensionless wing-span coordinate
μ	$[\mathrm{kg\,m^{-1}\,s^{-1}}]$	Dynamic viscosity
ν	$[\mathrm{m^2\,s^{-1}}]$	Kinematic viscosity
$\widetilde{\nu}$	$[\mathrm{m^2\,s^{-1}}]$	Kinematic viscosity transform (Spalart-Allmaras turbulence model)
ρ	$[\mathrm{kg\,m^{-3}}]$	Density
τ		Viscous stress tensor
ϕ		Arbitrary flow field variable
ω	$[\mathrm{s^{-1}}]$	Specific rate of turbulent dissipation
$\vec{\omega}$		Vorticity vector
$\widetilde{\Omega}_m$	$[\mathrm{s^{-1}}]$	Rotation velocity of the reference system

Subscripts

∞	Freestream conditions
a	External flow conditions at jet exit section
bal	Balanced through the total pressure recovery in the suction duct
c	Convective
e	Effective
i, j	Vectors Components parallel to the reference system directions
iso	Quantity obtained by an isentropic process
j	Jet condition
max	Maximum value for angle of attack variations
n	Cell number for discretized equations
rms	Root mean square
stall	Stall conditions
t	Total quantity
v	Viscous

Acronyms and Abbreviations

2D	Two-dimensional
3D	Three-dimensional
ACARE	Advisory Council for Aviation Research and Innovation in Europe
CFD	Computational Fluid Dynamics
DLR	German Aerospace Center (Deutsches Zentrum für Luft- und Raumfahrt)
DNS	Direct Numerical Simulations
EASM	Explicit algebraic stress model
LES	Large Eddy Simulations
LGF	Lift Gain Factor
NACA	National Advisory Committee for Aeronautics
NASA	National Aeronautics and Space Administration

NLR	Curvature correction of SST turbulence models
PIV	Particle Image Velocimetry
RANS	Reynolds-Averaged Navier Stokes
RCC	Rotation Curvature Correction
RSM	Reynolds-Stress turbulence Models
SA	Spalart-Allmaras turbulence model
SARC	Spalart-Allmaras turbulence model with curvature correction
SFB	Collaborative Research Center (Sonderforschungsbereich)
SST	Shear-Stress Transport
SSTRC	Shear-Stress Transport with curvature correction
STOL	Short Takeoff and Landing
URANS	Unsteady Reynolds-Averaged Navier Stokes

1 Introduction

1.1 Motivation

Transportation plays a primary role in global economic development, creating a need for efficient world-wide mobility. For instance, the current expansion of international markets, along with the global urbanization, drive projections of a rapid growth of the world traffic volume. Based on these considerations, strategic drivers for the future of aviation research were identified by NASA in 2013 (NASA Blueprint for Aeronautics [115]):

- global growth in demand for air mobility;
- climate issues, sustainability, energy transition;
- technological exchange among different fields.

The main objective of the long-term vision defined by these drivers is to define concrete guidelines for improving the quality of the commercial service and solving issues arisen from the continuous growth in demand for passengers and goods transportation. Similar objectives are established by the "Vision Flightpath 2050 - Strategic Research and Innovation Agenda", published in 2011 by the Advisory Council for Aviation Research and Innovation in Europe (ACARE) [3]. In particular, the reduction of polluting emissions and door-to-door travel time are among the main goals. An effective solution to these problems is to extend commercial transport to small airports, which are currently unused for this purpose because of short runways and proximity to populated areas. In this respect, the aircraft flight performance and noise emissions during take-off and landing play a primary role. A technological challenge is therefore represented by the high-lift systems, since they are responsible for providing the required lift coefficient and delaying stall at low flight speed. Complex mechanisms have been developed throughout the aviation history, leading mostly to a single extended leading-edge slat and one or more extended trailing-edge flap(s). These extended elements are however heavy and expensive to manufacture. To address these issues, the application of active flow-control technologies to high-lift systems has the potential of enhancing the lift performance and reducing the system complexity [13]. The essential difference between passive and active high-lift systems is that passive systems are based only on a modification of the airfoil geometry into a new fixed configuration which is suited to low flight speed; whereas active systems employ mechanical power to manipulate the flow behavior, for instance energizing regions of the flow field by means of jets, or removing parts of the boundary layer through a suction slot. In this way, active systems can generate high lift without complex mechanisms. In fact, active flow control may also lead to quieter aircraft, as it can provide the required lift coefficients without employing gaps, which are identified as major sources of airframe noise during approach and landing [135]. Along this line of thought, extensive knowledge is available from about 80 years of research on active high lift (see for example [118, 52]). The recent improvements in design means and techniques have yielded substantial progress in this field, as stated by Gad El Hak in 1991 in a comprehensive review of separation control techniques [54]: "The

tremendous increases in CFD capability which have occurred as a direct result of increases in computer storage capacity and speed are transforming flow separation control from an empirical art to a predictive science."

1.2 Objectives and Outline

The overview on flow control research presented in the next section gives a glimpse of decades of experimental, theoretical and numerical efforts focused on developing effective circulation control technologies. In this scenario, however, two fundamental aspects remain to be further investigated and improved: the aerodynamic efficiency of the overall high-lift configuration and its integration into the aircraft. Shortcomings in addressing these aspects would raise major technical problems and eventually prevent the industrialization of this technology. Recent analyses proved that only a multidisciplinary approach can provide viable solutions to these issues. Following this idea, the Collaborative Research Center (Sonderforschungsbereich) SFB 880 was founded to develop active high-lift generation solutions for future civil aircraft, combining the fields of aerodynamics, flight mechanics, aeroacoustics, material science, micro-technology, turbomachinery and electrical engineering. The joint effort is coordinated on the conceptual design data of a reference transport aircraft, which represents the state of the art in CO_2 reductions, low noise emissions, and short takeoff and landing capabilities.

Within the framework of the SFB 880, the present work aimed at developing a highly effective active high-lift configuration by means of RANS numerical simulations. In particular, the following objectives and design choices defined the guideline of the project:

- assure $C_L \approx 5$ at maximum lift condition;
- avoid the use of gaps to reduce noise emissions;
- provide a configuration that meets the technical aircraft-integration requirements set by the other research teams.

The active flap device employed here was previously developed at the Institute of Fluid Mechanics of the Technische Universität Braunschweig and is based on a thin air jet tangentially blown over the curved upper surface of a simple-hinged flap deflected by 65°. Thanks to the Coanda effect, the jet follows the contour of the flap entraining the surrounding flow downward and generating lift [130]. Starting from this configuration, the present project developed new technologies to reduce the momentum required by the jet to provide effective flow turning. The overall high-lift configuration is sketched in figure 1.1. The leading edge is equipped with a flexible droop-nose device suited for the high circulation levels yielded by the Coanda flap. The boundary layer behavior over the wing is improved by a wall-suction device, based on the idea that the Coanda jet can be generated by compact electric compressors integrated into the wings and the compressor intake can be used to manipulate the flow field around the airfoil. Finally a variable nozzle geometry is employed to modulate the wall-jet momentum and enhance flow mixing over the Coanda surface. The development and testing of these three elements is the object of this thesis and is organized in dedicated chapters.

Chapter 2 briefly illustrates the numerical approach adopted for the CFD simulations, and the main physical mechanisms that characterize the Coanda-flap flow and the stall dynamics. The employed Coanda-flap configuration is also presented here, reporting the main design features and some important aerodynamic sensitivities to geometrical parameters.

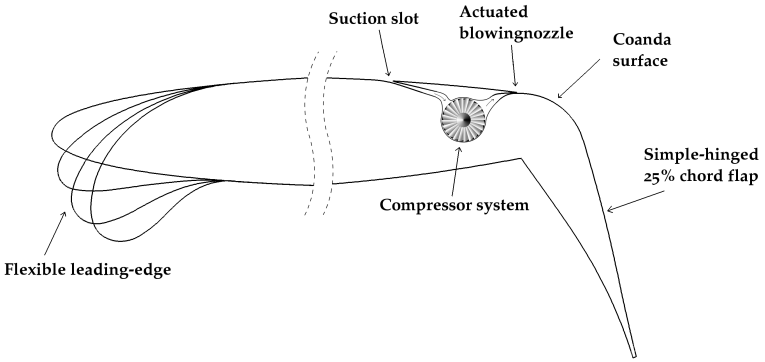

Figure 1.1: Scheme of the active high-lift configuration.

Chapter 3 describes the aerodynamic design of the droop-nose device. The geometry of the first 20% of the airfoil chord is modified to delay stall through a more efficient pressure distribution. Aerodynamic sensitivities of thickness and curvature are investigated, showing the improvement yielded by the flexible droop nose with respect to a conventional simple-hinged leading-edge flap.

The flexible device is then integrated into a high-wing wing-body aircraft configuration, as presented in chapter 4. The three-dimensional flow simulations highlight some unexpected flow phenomena at the wing root, which limit the maximum lift and cause stall at angles of attack significantly lower than for the two-dimensional analyses.

Chapter 5 focuses on the two-dimensional design of the air intake of the compact compressor. The intake duct is used here as a suction slot to manipulate the behavior of the boundary layer. Therefore, the intake slot is designed to achieve two objectives: obtaining high total pressure recovery at the end of the suction duct and increasing the maximum high-lift coefficient. A method is proposed to combine these two objectives in a single quantity, which is then used to evaluate the overall performance of different shapes and locations of the suction slot.

Chapter 6 discusses the effectiveness of unsteady actuation for the present Coanda flap application. Since the present study will be validated by water-tunnel experiments, two actuation techniques suited for incompressible flows are compared: 1) deforming the lip above the blowing nozzle and 2) controlling the total pressure in the jet plenum. The jet effectiveness obtained with the two approaches is compared analyzing the interactions with the outer flow. Next, a sensitivity study is performed to investigate the flow response to different forcing signals and the most important actuation parameters are identified.

1.3 State of the Art

1.3.1 Separation Control by Suction and Blowing

Flow separation is generally defined as the detachment of a fluid stream from a solid surface (e.g. [101, 22, 188, 54]). It can be caused by different factors, such as a severe adverse

pressure gradient [175, 176], or a sudden change of geometry [11, 80]. When the flow is still attached to the body surface, fluid particles within the boundary layer are slowed down by friction and by the increasing pressure, in case of an adverse pressure gradient. In terms of energy principles, the kinetic energy of the moving particles is gradually converted into potential energy by the adverse pressure gradient, and dissipated into heat by viscous effects through friction. If the initial kinetic energy is not sufficient to overcome the two effects, the motion of the near-wall fluid is eventually arrested. At this point the surface streamline leaves the body, and the boundary layer is said to separate [101]. Further downstream, a region of reverse flow occurs, where vorticity and velocity components normal to the surface are significantly higher. Boundary layer separation is in general associated with losses of some kind, for example losses of lift, increase of drag, reduced pressure recovery, etc. For this reason, engineers have been developing methods and devices to improve the boundary layer behavior and delay flow separation or avoid it entirely. Flatt [45] defines as boundary layer control any mechanism or process able to alter the normal behavior of the boundary layer, considering as normal behavior the natural development of the flow on a smooth straight surface. Fitting this definition are, for instance, control of transition, separation, skin friction, heat transfer, etc. Given an imposed geometry, the kernel problem in separation control is to enhance the momentum within the boundary layer. For this purpose, momentum can be transferred from the stream above the boundary layer or injected from an external powered source. The most popular flow separation control techniques are based on either passive devices, for example boundary layer tripping or vortex generators; or active ones, such as tangential blowing or wall suction. Typical applications of separation control are listed by Gad El Hak in [54]: effective low Reynolds-number airfoils for remotely piloted vehicles, propellers, windmills, helicopters, etc.; efficient inlets and diffusers; improved axial flow compressors; increased maximum lift for increased payloads; reduced engine power or noise at takeoff; shorter runways and reduced approach speeds; super maneuverability; efficient and effective stall or spin control; reduced drag on missiles, automobiles, ships and helicopters; as well as a myriad of applications in industrial aero- and hydrodynamics.

The idea of controlling flow separation is rather old. One year after the first powered flight, Prandtl pioneered the modern use of flow control in front of the audience of the Third International Congress of Mathematicians held in Heidelberg, Germany [138]. In the 8 pages required for acceptance by the Congress, Prandtl introduced the boundary layer theory, explaining the mechanics of steady two-dimensional separation, and described several experiments in which the boundary-layer behavior was manipulated. Later, in 1927 he proved the efficacy of removing a portion of the boundary layer by suction, to reduce the drag generated by a bluff body [139]. He obtained suction by means of a narrow slit located on one side of a circular cylinder, about 10° downstream of the natural separation line. As a result, separation was delayed on that side of the cylinder, yielding a great drag reduction and producing a transverse force. According to Schlichting [156], the benefit of boundary-layer suction is essentially generated by a variation of the velocity field outside of the boundary layer. The suction device creates a sink velocity distribution which is superimposed to the natural field. The flow upstream of the suction slot is therefore accelerated and separation is delayed. On the other hand, downstream of the sink the flow is decelerated, but the reduction of boundary-layer thickness due to the suction enables the boundary layer to withstand greater pressure gradients without separation. Experimental investigations of the lift performance enhancement yielded by boundary-layer suction were conducted by Schrenk in 1931 [164]. Testing of several suction-duct shapes and locations on a two-dimensional wind-tunnel model led to the conclusion that suction should be ap-

plied downstream of the suction peak in order to enable the boundary layer to withstand the adverse pressure gradient. Based on this research the German Aerodynamic Testing Establishment (AVA) decided to undertake the testing of suction in flight by designing and constructing the "suction aircraft" prototype AF1 [165, 166, 182, 207]. The lift gain yielded by suction was considerable, as the lift coefficient at takeoff of the AF1 was almost doubled and the rolling distance reduced by one half. The experience gained with the AF1 led to a second prototype in 1939, the AF2. With respect to the AF1, the improved prototype had thinner airfoils, two suction slots, and the suction blower was driven by the aircraft engine. A detailed description of the two designs, and a comparison of the flight performances can be found in Ref. [181], which was translated into English after the war and published as a NACA technical memorandum [183]. Boundary layer suction for the purpose of lift enhancement on high-lift configurations was also carried out by Walz [194], who applied suction to different airfoils and different flap chords. The necessary suction quantities, however, were too high to be of practical interest [206].

In the same years active flow control by tangential blowing was also investigated. Tangential blowing from a thin slit in the flow direction allows direct injection of momentum into the boundary layer, which enables the flow to withstand a greater pressure gradient and delays separation. Ejecting air through a backward opening slot located on the upper surface of an airfoil was first reported in the United States by Knight and Bamber in 1929 (N.A.C.A., TN 323), in France by Toussaint in 1931 (St. Cyr unpublished report) and in Germany by Baumann in the early 1920's (unpublished results reported by Wieland in 1927) [2]. This configuration received even more interest after the discovery of the Coanda effect, around 1935. According to the story, the Romanian inventor Henry Coanda employed a curved surface to deflect the exhaust of a radial piston engine from the wooden fuselage structure of an aircraft. As a result, the shielding plates entrained the hot exhaust inward, igniting and destroying the aircraft. The capability of the jet to follow a curved surface was then used in many devices, including car engines exhaust scavengers, wind tunnel turning vanes, thrust augmentors, water propulsion units, deflection surfaces, and rotary pumps [36]. The research continued during the following decades, leading to numerous attempts to apply boundary layer control to aircraft prototypes. In particular, the need for air superiority that preceded WWII provided great motivation and governments funded considerable research efforts in which high priority was given to boundary layer control. In 1944, experiments with variable blowing slot heights revealed that lift increments at equal values of blowing mass flow increased as the width of the slit was reduced [169]. When the same results were plotted in relation to the jet momentum, on the other hand, the lift performance collapsed on a single curve. The momentum coefficient was therefore introduced in 1948 to characterize blowing actuation (see Poisson-Quinton and Lepage [134]):

$$C_\mu = \frac{F_\mathrm{j}}{q_\infty S_\mathrm{ref}} = \frac{U_\mathrm{j}\dot{m}_\mathrm{j} + (p_\mathrm{j} - p_\mathrm{a})A_\mathrm{j}}{\frac{1}{2}\rho_\infty U_\infty^2 S_\mathrm{ref}} \tag{1.1}$$

where v_j and $\dot{m}_\mathrm{j}$ are the velocity and the mass flow of the jet at the exit, and S_ref is a reference surface.

The results achieved at that time had only little more than marginal success and there is no record of actual application of active flow control to operational aircraft during that period. New impetus was given to the research on boundary layer control with the introduction of jet powered aircraft in operational numbers in the military services. In particular, the use of jet fighters on Navy aircraft carriers defined new requirements in terms of takeoff and landing speeds. One of these research programs led to the high-speed blowing flap sys-

Figure 1.2: An F9F-2 of VF-21 aboard the USS Midway in 1952 [59].

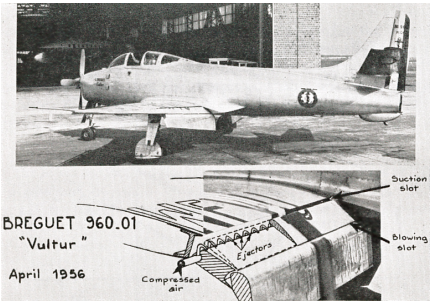

Figure 1.3: Full-scale application of suction and blowing on the Breguet "Vultur", 1956 [134].

tem proposed by Attinello in 1952 and first tested on a Grumman F9F Panther jet fighter in December 1953 [2] (figure 1.2). In that case, the compressed air was spilled from the engine, between the compressor and the combustion chamber, and yielded a decrease in stalling speed of 9 kn for takeoff and 7 kn for approach [59]. In the same period, Poisson-Quinton and Lepage utilized ejectors that enabled the use of suction and blowing combined on a two-element trailing-edge flap [134]. The upstream flap shoulder was slotted and also served as ejector inlet, providing suction. The shoulder of the second flap was instead used for blowing. The resulting lift was 56% higher than a conventional two-element Fowler flap, at $C_\mu = 0.082$. The behavior of the system was also tested in flight, on the Breguet "Vultur", resulting in stall speed reduction of 20 km/h (figure 1.3). In the following years, a large number of other experimental aircraft demonstrated the effectiveness of boundary layer control. Some of these aircraft reached the mass production, as the Lockheed's F-104 (in production from 1955 to 1983) and the MIG-21.

The enhancement of cruise performances has always been a priority for the aerodynamic research. It was suggested that laminar flow could be maintained by means of suction over a thick wing section if a favorable pressure gradient exists over most of its surface. The GLAS II airfoil, designed by Glauert in 1955 [49, 50], achieved lift to drag ratios from 250 to 550 at $C_L > 1$ and $Re \approx 10^6$. To achieve this extreme performance, however, no attention was paid to the energy needed by the suction system. Eventually, a flight test conducted with a glider revealed the problems related to the very high suction requirements, and the research was abandoned [74]. In 1956 Raspet at al. observed that the efficiency of suction was enhanced when obtained through a porous surface instead of a single slit [144]. A few years later, in 1961, Loftin tested different suction-slot shapes with the purpose of reducing drag by extending the region of laminar boundary layer [94]. From the experiments he concluded that a large slot reduces the viscous losses inside the suction duct, but also generates a detrimental disturbance in the boundary layer of the external flow.

A comprehensive review of the research performed until the 1960 on flow control was published by Lachmann [87, 88]. The two volumes provide a broad overview of theoretical and experimental efforts undertaken worldwide to develop boundary-layer control methods and represents an important milestone in the gathering and sharing of the knowledge achieved during the previous forty years of research on the topic.

In the early 1960's, flight tests performed by Schwarz and Wuest [168], and Head and Clark [56] showed that suction at the leading edge could replace a conventional leading-edge slat. An exhaustive review of prototype aircraft for boundary-layer suction research was published by Cornish in 1965 [29]. Later, further insight into the physics of boundary layer suction was provided by the experiments of Schildknecht, who measured the effects of wall suction on the turbulent flow inside a pipe [155]. When the suction device was activated, the velocity components normal to the wall were increased, generating a transport of turbulent energy towards the wall, where the energy was dissipated. As a result, the turbulent energy was drastically reduced even with low suction rates.

Meanwhile, important progress was also achieved in research on boundary-layer momentum injection. In 1960, for instance, the Japanese company Shin Meiwa built a STOL seaplane prototype equipped with active flow control. In this case, the blowing device mounted on the high-lift flaps was powered by a dedicated gas turbine, positioned inside the fuselage. The active flap were also able to deflect the propeller stream and enhance the lift performance to $C_L \approx 7$ [79]. This design reached the industrial production in the 1970's under the designation US-1A [187], and was updated in the 1990's with the new version Shin Maya US-1A "kai" ("improved US-1A"). In the 1970's the United States Air Force launched the AMST (Advanced Medium STOL Transport) project, issuing an official request for proposal in 1972. The project was intended to replace the Lokheed C-130 Hercules tactical transport, based on new STOL specifications. These included operating from a 610 m semi-prepared field with a 740 km range and a 12 t payload [122]. The C-130 of that era required a field length of about 1.2 km for this load [34]. The projects presented by Boeing and McDonnel Douglas won development contracts and resulted in two new prototypes, the YC-14 and YC-15, respectively (figure 1.4). Both aircraft met the STOL requirements by using active high-lift systems. In the case of the Boeing YC-14, the two jet engines were mounted over the wing, blowing air over the suction side of it. The jet streams would then follow the curvature of the wing and of the deflected flap, thus providing high lift [114, 195, 19, 184, 102]. This kind of active lift generation system is known as "upper surface blowing". Blowing was also applied at the leading edge of the airfoil, to delay flow separation in that area. Even with one inoperative engine, the YC-14 was able to reach $C_L \approx 4$. For the McDonnel YC-15, the required STOL capabilities were achieved by employing an "externally-blown flaps" configuration. The four turbofan engines were mounted underneath the wing and the propulsive jets were deflected downward by double-slotted flaps. Although both designs could fulfill the requirements, neither the YC-14 nor the YC-15 ever reached production, as budget limitations forced the USAF to cancel the program [77]. The YC-15, however, served as basis for the C-17, which has been the most successful active-circulation-control aircraft so far.

At the same time, NASA in collaboration with Boeing modified a Havilland C-8A with a high-lift system based on an "upper surface blowing" configuration to obtain STOL characteristics [42, 28, 141, 97]. The first flight was performed in 1978. Similarly to the YC-14, the four jet engines of the "Quite Short-haul Research Aircraft" (QSRA) were located on top of the wing, and the leading edge was equipped with a blowing slit to avoid separation [27]. The leading-edge device, however, was later replaced with a conventional slat [100]. This configuration yielded lift coefficient around 10. In order to assure sufficient control authority at very low flight speeds, part of the external engine jets was directed to the ailerons. The same configuration was later adopted for a modified version of the Kawasaki C-1 built by the Japanese National Aeronautics Laboratory in the late 1980's, named ASKA [209, 208]. In this case, the "upper surface blowing" wing was able to provide $C_L \approx 5$. Also in this configuration the flow of the external engines was partially deviated

(a) YC-14 [60]

(b) YC-15 [61]

Figure 1.4: Active high-lift prototypes resulting from the USAF Advanced Medium STOL Transport project.

to the ailerons to allow longitudinal control at low flight speed. The upper surface blowing concept was extensively investigated in the 1970's and 1980's during several other research programs, as for instance Ref. [48, 47, 96, 98, 153, 9], to name only a few. The advantages of such configurations at low speeds were balanced by disadvantages during cruise conditions [10, 104, 199]. The nozzle shape, for example, was designed to spread the jet stream over a wide portion of the wing for higher efficiency during slow flight. This, however, was affecting the thrust generated by the jet. An additional problem of the integration of the engine above the wing was the aerodynamic interference between the engine fairing and the wing [83, 173], which significantly increased drag at high flight speed ($M > 0.7$) [6, 154, 133, 73].

Zha et al. developed in 2006-2007 an airfoil configuration where suction and blowing were combined [213, 214]. The suction slot was located at the end of the suction side and the internal flow was then directed to the leading edge, where it was blown from a thin slit, tangentially to the airfoil upper surface. In this configuration suction was used to avoid separation at the trailing edge, whereas blowing was enhancing boundary layer momentum at the leading edge. This set-up was mechanically very simple, as it allowed high-lift generation without moving parts. However, the system could not be turned off during cruise condition, increasing significantly the overall energy requirements. Nevertheless, Esposito et al. came to the conclusion that this high-lift system, in combination with a simple-hinged 20° flap, could be employed on a Boeing 777-330 [43]. More recently, in 2013, Chen et al. compared the lift performances obtained by boundary layer suction and tangential blowing when applied to a thick airfoil with the purpose of trailing-edge separation control [23]. The comparison showed that suction was more effective for a low momentum of the flow through the slot; whereas for high levels of actuation tangential blowing yielded a better performance. Moreover, according to the study, the benefit of suction was enhanced by locating a wide slot downstream of the natural separation line; whereas blowing was more effective when applied from a thin slit upstream of the natural separation line. The same conclusions were drawn by Schmalzel in 2006, who tested suction and blowing devices on a

(a) Coanda circulation control with blunt trailing edge

(b) Coanda flap

Figure 1.5: Internal blowing concepts to obtain high lift coefficients.

V-22 airfoil [157] and on a powered airplane model, and observed that suction can be more effective than blowing at low rates.

The various flow control approaches were categorized by Gad El Hak based on their required energy expenditure [53]. Tangential momentum injection into the boundary layer was identified as one of the most promising flow separation control techniques. External blowing configurations, as the aforementioned "externally blown flaps" and "upper surface blowing", yield moderate powered lift augmentation for a given thrust-to-weight ratio. Larger lift gains can be achieved by blowing internally supplied air over suited convex surfaces. In both configurations sketched in figure 1.5 effective flow turning is achieved by exploiting the turbulent flow entrainment of a tangentially blown Coanda jet to avoid flow separation. The blunt trailing edge configuration, however, requires actuation also during cruise phases in order to prevent a drastic drag increase due to trailing-edge separation. This problem can be solved with a movable trailing edge device (figure 1.5b), which can provide the suited Coanda surface for takeoff and landing while maintaining the sharp trailing edge during cruise. This configuration is also referred to as "Coanda flap". The terms "Coanda flap" and "active high-lift flap" are used in the following sections interchangeably to refer to this configuration. A comprehensive overview of the state of the art in the field of circulation control by internal blowing can be found in Ref. [35].

A Coanda flap device was implemented into a supercritical airfoil by Englar in 1984 [37] and later improved for numerical validation [41, 39]. Here, a 0.7% chord flap, pivoted about a hinge located on the lower surface of the airfoil, thus exposing a low radius at the exit of the blowing slot. This configuration was named "dual radius Circulation Control Wing" (CCW), and was the object of several investigations. This airfoil yielded $C_L \approx 8$ at $C_\mu = 0.3$ in landing configuration, reducing the necessary takeoff and landing runway length by about 70-80% [40]. A Coanda-like active flap configuration was also tested by Meunier using the ONERA elsA CFD code [107]. An automated surrogate-based optimization algorithm was assessed for the design of a circulation control airfoil. The configuration consisted of a simple-hinged deflected flap and a conventional slotted slat.

More recently, Milholen et al. [108] conducted experiments in the NASA-LaRC National Transonic Facility at high Reynolds number with the "FAST-MAC" model. The tapered, swept and twisted supercritical wing model was equipped with a 15%-chord Coanda flap at 60° deflection. The Reynolds number reached $15 \cdot 10^6$ and the freestream Mach number varied from 0.1 to 0.2, for the high-lift configuration. With the Coanda jet fully attached to the flap, the circulation control nearly doubled the lift coefficient, at $\alpha = 0°$. For higher blowing momentum the lift kept increasing but at a lower rate. At $M = 0.2$, however, a supersonic expansion occurred on the Coanda surface, followed by a sudden separation of the wall jet. As a result, the lift exhibited a sudden decrease for $C_\mu > 0.1$. The FAST-MAC

model was also tested in cruise conditions, with freestream Mach number ranging from 0.7 to 0.88 and Reynolds number from $10 \cdot 10^6$ to $30 \cdot 10^6$. These measurements proved the potentials of active circulation control to positively influence the compressible flow field over the wing during cruise flight.

1.3.2 Noise Research on Tangential Blowing Devices

A major potential benefit of employing active flow control to high-lift systems is the reduction of the noise impact on the areas surrounding airports. Two aspects could yield significant improvements in this respect: (a) the possibility to avoid the use of gaps, thus reducing noise emissions [110], and (b) steep climb-out and approach flight paths, which reduce noise exposure to surrounding communities [40]. Experimental measurements of the noise generated by a high aspect-ratio jet were carried out by Munro et al. [111, 113, 112]. The experimental set-up was designed to investigate the flow dynamics and the aeroacoustic characteristics of a free jet, with the possibility of varying its width and thickness. The noise intensity was found to be proportional to the square of the jet height, for aspect ratio higher than ~ 600 and to power of 3/2 of the height, for lower aspect ratios. The jet width was found to have little effects on the noise intensity. Pollenske recently investigated the noise produced by a Coanda flap configuration very similar to the one employed in the present work [136]. A 0.3-meter chord airfoil model was equipped with a 30% chord Coanda flap, deflected by 40°. In comparison with a conventional 3-element high-lift configuration generating the same lift coefficient, the gap-less Coanda flap led to a noise reduction of 5 to 8 dB in the frequency range from 0.2 kHz to 2.0 kHz, depending on angle of attack, blowing rate and flight speed.

1.3.3 Numerical Simulation and Experimental Validation of Tangential Blowing Devices

The broad picture drawn by the large number of published research on active flow control clearly shows that several parameters need to be carefully investigated in order to assess the potential of a particular mechanism. For instance, optimal slot location and dimensions may be different for various flow conditions and airfoil geometries. Therefore, the design of an active flow control device must begin with a comprehensive investigation of the aerodynamic sensitivities to the design parameters for the specific application. For this purpose, Computational Fluid Dynamics (CFD) is an extremely powerful tool. However, the complex physics of active separation control mechanisms, along with the broad range of spatial and temporal scales that characterize the flow phenomena, may affect the accuracy of numerical simulations. Extensive research in this direction was undertaken in the last decades with the support of experimental measurements and sophisticated simulations, in parallel with the pursuit of highly efficient configurations.

An early numerical approach to account for streamline curvature was proposed by Dvorak in 1973 [32, 33], and was able to realistically predict the behavior of a turbulent boundary layer on a convex surface, as described by the experimental data of Kind and Maull [81]. Improved experiments, with the purpose of CFD-solver validation, were performed by Novak et al. on an elliptical airfoil in 1986 [123, 124]. During these campaigns Laser-Doppler-Anemometry was used to measure boundary-layer profiles and velocity fluctuations in the flow above the Coanda surface. These results remained for long time the only validation data available for calibration of numerical solvers and turbulence models. More recently,

Rumsey et al. [150] tested the accuracy of three types of turbulence model in presence of curvature effects for the flow in a U-duct. The explicit algebraic stress model led to slightly better results than the two linear eddy-viscosity models (the one-equation Spalart-Allmaras, SA, model and the two-equation shear stress transport, SST, $k-\omega$ model from Menter). However, none of these models was able to capture the suppressed turbulence near the convex wall, whereas a full Reynolds stress model was. The paper shows that the assumption of Reynolds stress anisotropy is not fulfilled in region of strong curvature. Similar conclusions were drawn by Slomski et al, who investigated the influence of turbulence models on the performance of active high-lift airfoils in 2002 [177]. Three advanced turbulence models were tested: the standard $k-\epsilon$ model, a modified $k-\epsilon$ model, and a full Reynolds stress model. For low jet momentum rates, the $k-\epsilon$ and modified $k-\epsilon$ models could predict lift reasonably well. For higher C_μ, however, only the Reynolds stress turbulence model could accurately capture the physics of the circulation control problem. A few years later, in 2006, Lee-Rausch simulated the flow around a Coanda flap configuration employing the SA model [89]. Although an angle-of-attack correction was estimated to compare numerical and experimental results, it was not possible to obtain good agreement between the two data sets. The author mentioned jet velocity and wall interactions as possible uncertainties responsible for the poor validation. More accurate results for the same configuration were obtained by Chang [21], who employed a Reynolds stress model and the Menter SST model.

In order to increase the capability of the SA model to predict high-curvature flows, Spalart and Shur proposed a modified version of the SA model referred to as SARC (Spalart-Allmaras model for Rotation and/or Curvature effects) [179]. The SARC model was finally able to match quite well experimental results from a curved channel [174]. The higher accuracy of the SARC model for rotational flows was also confirmed by Nichols [117], who compared SARC and SA results for the simulation of a free vortex. Similarly, Hellsten proposed a correction for the Menter SST model, which led to more accurate results for rotational or curved flows [58]. Both the SA and the Menter SST models, with the respective corrections were tested in a U-duct by Mani, and provided fairly good results [99]. The SARC model, in particular, led to the most accurate solution, but at higher computational costs. Performance improvements of two-equation turbulence models for curved wall jets were also achieved by Pajayakrit [127], who introduced rotation/curvature modifications to the Wilcox $k-\omega$ [201] and Wilcox multi-scale [203] models. Brandsma et al. investigated the behavior of the two-equation $k-\omega$ model for capturing the vortical structures at the leading-edge of a delta wing [12]. Two approaches were tested to improve the accuracy of the simulations. One modification consisted in limiting the production of turbulent kinetic energy in the k-equation, whereas the other modification aimed at increasing the production of dissipation in the ω equation. The comparison with experimental results showed that increasing the production of ω yielded higher accuracy. Recently, Weinman published an overview on the numerical rotation/curvature treatments available in the DLR TAU code [197].

Although the rotation/curvature corrections improved the performances of the one and two-equation turbulence models in presence of curved flows, circulation control simulations still represent a challenge. In 2006, Swanson and Rumsey published a study that aimed at identifying issues and inaccuracies for this particular class of problems [185]. The tested models were the SARC model, the Menter SST model and the $k-\zeta$ model (turbulent kinetic energy and enstrophy). All models over predicted significantly the experimental results, showing, however, very different convergence histories and reactions to mesh refinement. Results obtained with the SARC and the $k-\zeta$ models have exhibited consistency with mesh refinement, whereas the Menter SST results showed inconsistent behavior. More-

over, Menter SST steady-state computations did not reach converged solutions because of irregular fluctuations of the aerodynamic coefficients and sometimes unphysical flow fields. Only time-accurate computations were resulting in converged solutions, for the Menter SST model.

In the same year, a dedicated wind-tunnel campaign was carried out by Jones et al. to define a guideline for active high-lift experiments aiming at numerical validation [70]. The analysis focused on the physics of the flow phenomena using highly accurate measurement techniques, such as hot wire and Particle Image Velocimetry (PIV). One of the main outcomes of the study was the conclusion that for the design of numerical-validation experiments, the main driver should be a high measurement accuracy, rather than the airfoil lift performance. This includes relatively thick Coanda jets and large Coanda surfaces in order to easily measure the jet characteristics and velocity profiles at the nozzle outlet and on the Coanda surface. Moreover, the model should have an aspect ratio greater than 3, to minimize the juncture effects associated with extreme high lift. An overview of the CFD validation experiments conducted at NASA until 2008 was published by Jones [72]. Based on this experience a new model was built and tested by Georgia Tech Research Institute in collaboration with NASA with the purpose of CFD code validation [38]. Separation control was implemented by tangential blowing over a thick circular trailing edge in order to achieve accurate measurements of the flow quantities. Moreover, without a sharp trailing edge the Kutta condition is entirely determined by the blowing momentum. Under this condition the solution of a numerical simulation is particularly sensitive to the capability of the turbulence model to accurately estimate the eddy viscosity, even in the presence of high flow curvature. Allan et al. performed numerical simulations of this configuration in 2011 [1]. The numerical study started with a comparison of the bench top (i.e. $U_\infty = 0$) jet velocity profile, obtained experimentally by hot-wire measurements. The numerical solution showed, in this case, good agreement with the experiments. In presence of a $M = 0.1$ oncoming freestream flow, however, the jet velocity peak increased, due to the lower local static pressure, which creates uncertainties on both the numerical and experimental side. The one-equation Spalart-Allmaras and the two-equation Menter SST turbulence models were tested, with and without rotational/curvature correction (RCC). The SA model overestimated the airfoil lift by 70%, which was reduced to 46% by the RCC. The Menter SST model with RCC performed better, but still over predicted the lift coefficient by 25%. Low Mach number preconditioning was also tested, but it simply introduced a small amount of unsteadiness to the lift convergence history without varying the final lift coefficient. Note that these two-dimensional computations did not account for wind tunnel wall effects. In later experimental analyses, the internal shape of the plenum was modified to reduce internal turbulence and improve jet characteristics [128]. Also, a transition study highlighted the need for applying trips to both the upper and the lower surfaces of the airfoil model.

Other test cases were examined by Rumsey [152] to characterize the behavior of RANS turbulence models with active flow control. All tested models predicted too low turbulent shear stresses in the 2D separated region, resulting in a late flow reattachment, in comparison with experiments. The differences in pressure distribution among the SA, Menter SST and EASM-kω models were not large in comparison to the difference obtained with respect to the experimental data. Second order turbulent advection terms were also tested and compared with the commonly used first order terms. The improvement in accuracy were not significant and the second order terms did not always run successfully. An important issue that emerged in circulation-control airfoil simulations was the occurrence of non-physical solutions with circular trailing edges. In these critical cases a wrap-around of the jet was predicted, where the jet remained attached to the entire circular trailing edge

and part of the airfoil pressure side. The problem was addressed by Swanson in [186]. In his case, the use of rotation/curvature correction solved the problem, allowing the SA model to accurately predict separation. An insufficient grid density in stream-wise direction on the Coanda surface was also considered a possible cause of this behavior.

The shortcomings of RANS models for flows involving separation or free vortices emerged also from the work of Togiti et al. [191]. The test case was a flat plate with zero pressure gradient and with a single circular or rectangular actuator (hole or slot). DLR's $SSG/LRR-\omega$ differential Reynolds stress model was applied and its results were compared to predictions obtained with eddy-viscosity-based models (SA and Menter SST). Result comparisons revealed that the SA and Menter SST model were unable to capture the vortices further downstream of the injector, whereas the predictions by the $SSG/LRR-\omega$ model agreed well with the measurements.

A deeper understanding of the physics of wall-bounded jets on curved surfaces could provide an important contribution to the development of accurate numerical methods for active high-lift systems. Detailed information is, however, either lacking or difficult to obtain from experiments. In this context, highly accurate numerical simulations can be a useful tool to develop a reliable and comprehensive computational database. The capability of highly accurate simulation approaches to provide detailed information on boundary layer transition and separation was assessed by Yang in 2001 [210] and Li in 2003 [91], who performed Large Eddy Simulation (LES) and Direct Numerical Simulation (DNS) computations, respectively. The investigated configurations were a round leading edge at $Re = 3450$, in the first case, and a NACA 0012 at $\alpha = 4°$ and $Re = 100000$ in the second case. In both studies, the information content of the solutions was extremely rich, allowing an accurate description of the transition and separation mechanisms.

LES circulation control simulations were carried out and validated by Nishino in 2010 [119]. A very good agreement with experimental measurements was achieved at low blowing condition ($C_\mu = 0.044$), but for higher blowing rate ($C_\mu = 0.12$) the results were less accurate. However, more detailed data of the jet boundary condition at the slot exit would be required to draw firm conclusions. Also, interactions between the tunnel side walls and the jet sheet can generate streamwise vortices downstream of the model, which induce an additional component of downwash [120]. This effect increases with increasing blowing rate and was not accounted for in the presented comparison. The detailed information provided by the LES computations from Nishino was later employed for a comparison with RANS models [151]. The investigation consisted of 3D LES computations and 2D RANS computations using SA, SARC, Menter SST, Menter SST with curvature correction (SSTRC), and EASM-kω turbulence model. The study confirmed the importance of rotation and curvature corrections for the simulation of Coanda jets, since only the models able to capture these effects (SARC, SSTRC and EASM-kω) were able to predict the location of the flow separation in good agreement with LES. Among these, the most accurate velocity and turbulence profiles over the Coanda surface were provided by the SARC model. Although the flow field over the Coanda surface could be reproduced fairly well, the RANS models still predicted between 12% and 17% higher lift. Accordingly, the location of the stagnation point and the suction peak at the leading edge were not matching the experiments. The reasons for this discrepancy may be an insufficient grid resolution, a different vortex structures in the separated region, or shortcomings of the turbulence model in predicting the free-jet characteristics. The SARC model provided the most accurate results in the near-wall regions, but it performed worse than SSTRC and EASM-kω in the free-shear jet area downstream of the separation point. The publication also reported the computational cost of the employed approaches: on the order of several hours for a fine-grid RANS computation

on 6 processors, and about 2 months for a LES computation on 256 processors. As part of the same project, DNS computations were performed by Madavan [95] on the same airfoil. One major difference between the DNS approach and the LES computations is that the compressible equations were solved by the DNS solver, whereas an incompressible formulation was used in the LES. At low jet momentum coefficient, the pressure distributions of the two numerical approaches and the experiments were in very good agreement, allowing a one-on-one comparison between the LES and the DNS flow field structures. At high jet momentum, on the other hand, the comparison was not as successful. Higher pressure was reported at the leading edge and at the trailing edge by the DNS simulations. However, the suction peak on the Coanda surface matched the experiments fairly well.

From this brief overview on numerical studies on circulation control airfoils it emerges how the accuracy of the numerical solution strongly depends on the investigated configuration, flow conditions, and turbulence model with relative modifications. In this scenario, the studies published by Pfingsten in 2009 are of particular interest for the present work, as he tested both numerically and experimentally a very similar configuration to the one investigated here [132]. In these studies, the SA turbulence model performed quite well in predicting the pressure distribution around the circulation control airfoil (see section 2.3.1). 3D simulations also captured the complex vortex structures that occur at the wind tunnel walls.

1.3.4 Leading-Edge Stall Protection

The high levels of circulation yielded by an active high-lift device induce strong suction peaks at the leading edge of the airfoil, where the flow experiences a great acceleration due to the high curvature rate of the surface. This condition may affect the airfoil behavior for two reasons: 1) the resulting friction causes viscous losses within the boundary layer and 2) the boundary layer has to withstand a strong adverse pressure gradient along the airfoil upper surface. These dynamics explain the reduction of stall angle of attack typically observed for an augmentation of circulation due to a trailing-edge device. The classic means to address this problem are the droop nose and the slat, as sketched in figure 1.6. The conventional droop nose, also referred to as leading-edge flap, has the advantage of a much lower technical complexity, but it presents a new area of high curvature over the hinge line, which causes a second suction peak. This may limit the lift performance in case of particularly high circulation. An advanced variation of the leading-edge flap is the flexible droop nose. In this case, the surface curvature is gradually increased by means of an internal mechanism that deforms a flexible skin. There are currently no examples of actual use of this device on existing aircraft, but promising research on flexible materials and internal mechanisms has been successfully carried out [159, 160, 158, 149, 82].

The improvement of maximum lift coefficient and stall angle yielded by conventional stall-protection approaches depends on the baseline airfoil geometry and various design constraints. However, the results of the DLR high-lift research program (Wild, Ref. [204]) provide a representative picture. The investigated configuration was a transonic wing section equipped with a single slotted Fowler flap and different leading edge devices. The results are summarized in table 1.1 and show that a slat configuration yields much larger improvements than a flexible droop nose.

Other studies were carried out by Shmilovich and Yadlin, who compared a rigid-droop nose device and a conventional slat configuration on an active high-lift airfoil [172]. Also in this case, the slat configuration led to higher stall angles, compared to the droop-nose device. The complex flow phenomena generated by a slotted device were also discussed [171]. In

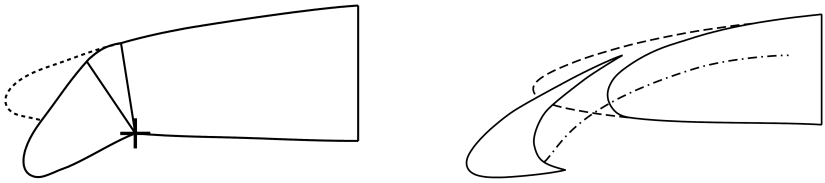

(a) Rigid droop-nose configuration **(b)** Slat configuration

Figure 1.6: Conventional leading-edge devices for stall protection.

Table 1.1: High-lift performances of the DLR F15 airfoil equipped with different leading-edge devices at $M = 0.2$ and $Re = 5 \cdot 10^6$, according to [204].

	$C_{L_{\max}}$	$\alpha_{\text{stall}}[^\circ]$
Fowler flap and clean leading edge	3.2	8.5°
Fowler flap and slat	4.6	31.0°
Fowler flap and flexible droop nose	3.6	14.0°

particular, the low momentum region of the slat wake exhibited a sudden spreading as it encountered the strong pressure gradient above the flap. Such dynamics can have a highly detrimental effect, as they can limit the lift performance even without a boundary-layer separation [211]. A rigid droop-nose device was also investigated by Jirásek and Amoignon, who proposed an approach to optimize the design and compared the resulting configuration with a Krueger flap [68]. The Krueger flap led to slightly higher lift and higher stall angles, probably thanks to the extended airfoil surface. The aeroacoustic performance of a droop nose was recently evaluated by Pollenske et al. [137], who carried out experimental measurements of a slat configuration and a flexible droop nose device in combination with a Fowler flap. The acoustic data measured with the droop nose did not show significant noise increase compared to the cruise leading-edge configuration, which correspond to a broadband reduction of 5dB with respect to the slat device. The aerodynamic efficiency of the droop nose, however, resulted about 60% lower than the slat configuration.

Published research on stall protection approaches for circulation control airfoils is limited. Some of these studies focused on the possibility of delaying stall by employing active boundary-layer control also at the leading edge [35, 67, 39, 51, 66, 170]. Although the goal of enhancing the stall angle was achieved, the overall efficiency of the system decreased considerably because of the additional blowing required by the leading-edge flow control device. Jensch carried out investigations of leading-edge blowing with the airfoil and flap configuration employed in the present work [66]. The efficiency of the system was represented by the ratio between the gain in maximum lift yielded by the active system and the required blowing momentum. The active high-lift device was a 30% chord Coanda flap, deflected by 80° and the freestream condition were $M = 0.125$ and $Re = 18 \cdot 10^6$. The minimum blowing rate to avoid flow separation from the Coanda flap was identified at 0.083. Under these conditions, maximum lift was limited by leading-edge separation at

$\alpha_{\text{stall}} = -4°$. An additional blowing slot was then located immediately downstream of the suction peak, at 0.02% of the chord. A leading-edge actuation of $C_\mu = 0.043$ increased the maximum lift coefficient by 0.045, but the overall efficiency decreased by 21% because of the higher blowing. However, this dual-slot configuration turned out to be more effective than applying the total blowing momentum, $C_\mu = 0.126$, at the Coanda flap only. Tests on a similar configuration were reported by Englar in Ref. [39]. A 10% chord Coanda flap was deflected by 90° and combined with a leading-edge blowing slot located at 0.5% chord. The leading-edge blowing was set at $C_\mu = 0.18$, while the flap momentum coefficient was varied from 0.0 to 0.28. The resulting performances were compared to a Krueger flap deflected by 60°. The pneumatic device led to higher maxium lift and stall angles over the entire range of tested flap blowing rates.

From these studies it can be concluded that the high levels of circulation yielded by an active trailing-edge system create the need for specific leading-edge devices. As a consequence, it is possible to exploit the full potential of active flow control for high-lift generation only including the leading edge into the design space of the overall system. This process should begin with a better understanding of the leading-edge flow sensitivities and target the blowing efficiency of the system, along with maximum lift and stall angle of attack.

1.3.5 Dynamic Actuation

Considerable effort has been undertaken in the last decades to reduce the power required by flow control means through periodic actuation [52]. Two studies during the mid-1970s investigated pulsed blowing associated with circulation control and proved that pulsed blowing reduces the mass flow required to control the boundary layer behavior [126, 193]. However, the physics of the phenomena remained mostly unexplained. Excitation of shear-layer instabilities was documented by Zaman and Hussain in 1981 [212]. Hot wire measurements showed that excitation could suppress turbulence up to 80%, limiting the formation of large convective structures within the mixing layer. Exciting the most unstable modes, on the other hand, increased turbulent diffusion, thereby generating smaller and less-energetic structures.

More recently, in 1996, Seifert published the results of four experimental campaigns that proved the higher efficiency of pulsed blowing with respect to constant blowing for flap angles until 40° [170]. In all configurations, a wall jet was tangentially blown in streamwise direction from the flap shoulder. Three airfoils were characterized by simple-hinged flaps, and one by a blown Fowler flap. In all cases, pulsed blowing was enhancing mixing between the near-wall flow and the momentum-rich fluid above. The jet momentum coefficient could be reduced by until 90% for the gap-less flap configurations, and 98% for the blown Fowler flap. This last case was particularly interesting to understand the physical mechanism leading such a dramatic improvement of actuation efficiency. A pulsed momentum coefficient of $C_{\mu_{\text{rms}}} = 0.00015$ was sufficient to enhance the momentum transport between the flap boundary layer and the flow that passed through the gap, yielding a 30% lift increase. At the same frequency, a $C_{\mu_{\text{rms}}} = 0.0012$ jet caused a second separation over the flap, reducing C_L to approximately unforced values. This showed that a stronger oscillation caused interaction with the wake of the airfoil main element, bringing low momentum fluid to the flap surface. Much larger oscillations (i.e. $C_{\mu_{\text{rms}}} = 0.0032$) were needed to reach the potential flow above the main element wake and restore attached flow over the flap.

More about the physics of flow separation and reattachment mechanisms emerged from an experimental study carried out by Nishri and Wygnanski [121]. The test case consisted in a deflected flat surface mounted at the end of a wind-tunnel floor. Actuation was obtained by

blowing air from a thin slit located over the flap hinge, where a flaperon provided unsteady modulation. The flap deflection angle was varied for different blowing jet characteristics, and the resulting flow behavior was investigated. The optimal actuation to reattach a separated flow was found at $F^+ = 1$ and $C_{\mu_{\mathrm{rms}}} = 0.0002$, which increased the flow-reattachment flap deflection by 9° (the flow naturally reattached at 24°). The resulting flow presented still a large separation bubble, which could be reduced by further increasing the forcing frequency. The optimal frequency to prevent flow separation was $3 < F^+ < 4$. Similar behavior was obtained with constant blowing at a C_μ about one order of magnitude higher. In the same years, Greenblatt and Wygnanski discussed the physics of shear layer excitation as basis for unsteady actuation in flow control [52]. They investigated the mixing layer between two flows at different velocities, which causes turbulent momentum exchange between the two streams. As a result the slower flow is accelerated and entrained into the mixing layer, while the faster stream slows down. They observed that momentum transfer across the mixing layer is mostly due to large quasi-deterministic vortical structures and concluded that the spreading rate, and hence the entrainment, can be altered by a two-dimensional, small amplitude excitation applied at the origin of the shear layer.

Further research on unsteady flow actuation was undertaken by Jones, who developed the GACC (General Aviation Circulation Control) model with the purpose of testing periodic blowing on a circulation control airfoil [71]. The 2D wind-tunnel model was equipped with a high-speed solenoid-actuated valve system to obtain high frequency pulsed blowing (200Hz). To minimize decay of the frequency response and avoid three-dimensional effects, the valves were located inside the model, in proximity to the exit slot. The resulting jet was blown tangentially over a circular trailing edge, which had a radius of 2% of the airfoil chord. Both experimental and numerical analyses showed that a 35Hz unsteady actuation can reduce the jet mass flow by 50%, with respect to steady blowing. Various duty cycles were also investigated, showing that the lift benefit increases at low duty cycles. Later, the lift performance of the GACC model was compared to the dual radius circulation control wing, which is a simple-hinged Coanda flap configuration [69]. In both cases pulsed blowing led to a 50% decrease of mass flow requirements in high-lift configuration. However, the circular trailing edge of the GACC airfoil needed more jet entrainment to achieve the same flow deflection. In cruise condition, the retracted flap did not require blowing, whereas the circular trailing edge needed blowing from both the upper and the lower side to create a "virtual" sharp trailing edge. Pulsed blowing for drag reduction in cruise condition led to a 55-60% mass flow reduction, with respect to constant blowing. The response of the dual radius circulation control wing to pulsed blowing was computed by Liu [92, 93]. The best lift performance was achieved at a forcing frequency of 400Hz and a duty cycle of 50%, but for the same average C_μ constant blowing was generating more lift.

Unsteady blowing from the shoulder of a leading-edge flap of a Coanda flap airfoil was tested by Melton et al. in 2005 [105]. Sinusoidal actuation was employed at both the rigid droop nose and the trailing-edge Coanda flap of a circulation-control airfoil. An important finding of the study was the effectiveness of amplitude modulation for unsteady flow excitation. The momentum coefficient required to reach a certain lift was reduced by 50% when amplitude modulation was activated. A comprehensive review of the work carried out at NASA Langley on steady and unsteady flow control for high-lift applications until 2002 can be found in Ref. [62].

Other experiments were carried out by Petz and Nitsche on a NACA 4412 airfoil with a single slotted NACA 4415 flap [129]. A pulsed jet was blown from a thin slit located at 3.5% of the flap chord, on its upper surface. Several forcing amplitudes and frequencies were tested at different flap deflection angles. Surprisingly, only little effects were observed

on lift or drag in the range of the investigated blowing momentum and frequency (i.e. $1.8 \cdot 10^{-}5 < C_{\mu} > 7 \cdot 10^{-}4$ and $0.5 < F^{+} < 2$). The flap deflection angle, on the other hand, had a large effect on the actuation. Until a deflection of 30°, the flow was naturally attached and no significant effect was caused by the blowing jet. Between 30° and 45° the actuation yielded up to 12% of lift improvement, but for higher flap deflection angles the effect of the forcing signal was no longer observed. Under these conditions, the enhanced mixing with the potential flow above the boundary layer was no longer effective, since the momentum added to the boundary layer was not sufficient to overcome the adverse pressure gradient over the flap.

An active Fowler flap configuration was also tested by Khodadoust and Shmilovich, both numerically and experimentally [78]. The 40° flap was equipped with a slot located on its upper side, blowing at an angle of 20° with respect to the flap surface. Flow separation from the flap could be reduced by a pulsed zero-mass-flow actuation that enhanced mixing with the high-momentum fluid passing through the gap. The experimental validation of numerical results showed good agreement within the linear range of the lift curve but inaccuracy at near-stall conditions. A similar problem was observed by Shmilovic and Yadlin, when testing a pulsed blowing actuation on a 40° simple-hinged flap [172]. In this case, the large recirculation area occurring downstream of the unactuated flap was manipulated by a number of suction/blowing slots distributed along the flap surface. The resulting excitation of the vortical structure caused an almost complete reattachment of the flow, increasing lift and reducing drag. Also in this case, the numerical solutions were affected by inaccuracies at angles of attack close to stall conditions, whereas the comparison showed good agreement for lower angles.

A joint research effort was undertaken in 2004 by DLR and the Institutes of Technology in Berlin, Braunschweig and Stuttgart with the foundation of the German Flow Control Network [205]. Experimental investigations were carried out on the effects of active flow separation control studying the lift performances of the two-dimensional DLR-F15 airfoil model equipped with a single-gap Fowler flap. Most of the tests were conducted at $M = 0.15$ and $Re = 2.0 \cdot 10^{6}$ in the DNW-NWB atmospheric low-speed wind tunnel. Pulsed-jet actuation was applied both at the main element, to delay leading-edge separation, and at the flap upper surface, to improve flow attachment on the flap. The leading-edge device was developed at TU-Braunschweig [161, 162, 163], and yielded a stall delay of 5° (with the Fowler flap deflected by 45° without actuation), whereas the flap actuation system, designed at TU-Berlin [129, 5], led to a lift increase of $\sim 10\%$.

The same configuration was recently tested in the ETW cryogenic transonic wind tunnel, where Reynolds number up to $Re = 7.0 \cdot 10^{6}$ could be achieved [55]. Thanks to pulsed jet actuation, the lift coefficients were increased up to $\Delta C_L \approx +0.7$. The lift gain was found essentially dependent on the momentum coefficient, as higher excitation momentum resulted in higher lift. Also, the momentum coefficient affects the optimal range of actuation frequency, causing variations. Based on these results, the optimal frequency range was between 75Hz and 200Hz.

Unsteady blowing on a slotted flap was recently investigated by Ciobaca et al. [24, 26]. The pulsed actuation was realized by a thin jet blown from the flap shoulder with an angle of 45° over the upper surface of the flap. The Menter-SST turbulence model was used to investigate the effect of different actuation signals on the lift performance. The signal amplitude was directly affecting the lift, whereas the frequency had a lower impact on the performance, within the tested frequency range. As a result, the lift coefficient was improved up to 20% within the linear range of the lift curve and by 5% at maximum lift conditions. The URANS simulations were able to predict lift with an error of about 3%

for the actuated case and 1% for the baseline, in comparison to the experiments. This configuration was then integrated into a half-span wing-body aircraft configuration. Both experimental and numerical studies were conducted on the model, proving the efficiency of the system also under operative conditions. SST numerical simulations were able to predict the main flow features considerably well, showing good agreement with the experimental trends. Difficulties were encountered when generating the squared actuation signal during the wind tunnel experiments. This was identified as the main source of discrepancy between experimental and numerical results. A comprehensive overview of the work carried out by DLR until 2013 on active flow control was published by Ciobaca and Wild [25].

1.3.6 System Efficiency Requirements

Since the birth of the boundary-layer theory, engineers have been trying to control the boundary-layer behavior for different purposes. As described in the overview on flow control research presented in the previous sections, several techniques have been developed and the related technology has been substantially improved, along with the physical understanding of the flow phenomena. However, boundary layer control never fulfilled the high expectations of the 1960s. This is mostly due to the low efficiency of the flow control systems, which require excessive additional power in order to provide meaningful lift enhancements (see e.g. [2]). Nevertheless, research on active flow control for the prevention of separation or transition continues to date. In the last decades, new analysis and design tools have become available thanks to the increase of computer storage capacity and speed. This, in combination with the new requirements of civil aviation mentioned above, has been leading to new initiatives in several fields of aerodynamic research. Among them, great progress has been achieved in active flow control technologies, yielding improved aerodynamic performance and reduced power requirement.

Acceptable values of C_μ can be determined based on the increase of engine weight caused by the active flow control, considering the engine as a viable solution to provide compressed air to the active high-lift system. The overall effects of an active high-lift system on the aircraft weight, and finally on the runway requirements, was investigated by Montanya and Marshall [109]. Approaches to estimate the takeoff and landing runway lengths were also presented in Ref. [8, 4, 196], showing that active circulation control is a viable solution to reduce runway length requirements. Recently, the preliminary design software PrADO was employed within the framework of the Collaborative Research Center SFB 880 in Braunschweig, Germany, to investigate the effects of active high-lift systems on the overall aircraft design and performance [142, 200]. Once the engine size was identified at takeoff conditions for the one-engine-out case, the software PrADO determined the corresponding optimal flap deflection angle and blowing rate. In table 1.2, results of these studies are reported, showing realistic aircraft weight growth for an advance turboprop aircraft. Two ways of generating compressed air for the high-lift system were considered: (a) bleeding air from the low-pressure compressor of the main engine core, and (b) dedicated electric compressors located inside the wing. The first solution affects directly the engine thermodynamic cycle, resulting in an engine growth of about 17%. In addition to this value, the piping needed to lead air to the active flaps brings the total weight increase to 37% of one engine weight. The solution based on electric compressors yields a better engine cycle, thus reducing the engine growth. However, the mass of the batteries and the additional compressor system causes an overall weight increase of 40%. An important outcome of the studies of Radespiel and Werner-Spatz [142, 200] was that substantial reductions of runway length requirements can be only achieved if a significant increase of maximum lift coefficient is accompanied by

Table 1.2: Overall weight increase due to active high-lift systems of a $M = 0.74$ turboprop reference aircraft, for one-engine-out takeoff conditions with $C_\mu \approx 0.025$.

Configuration	Takeoff length [m]	Passengers	Engine mass + Pipes electric compressors, generators [kg]
Turboprop, Conventional high-lift, [142]	1100	100	1256+0
Turboprop, Coanda flap, bleed air, [142]	800	100	1467+259
Turboprop, Coanda flap, electric compressors	800	100	1283+472

a moderate increase of the installed engine thrust.

Another full integration study of active flow control technology into a transport aircraft was conducted by McLean et al. in 1999 [103]. Among the numerous possible applications of flow control on the aircraft, high-lift systems were identified as the most promising in terms of potential benefits. The study team relied on active separation control to only match the performance of a conventional multi-element high-lift system. The major benefits led by flow control would therefore come from reductions of weight, complexity, and cost of the system. The benefit assessment showed potential reductions of 0.66% in airplane manufacturing cost, up to a 2.8% in weight, and about 3.1% in cruise drag, where 1% of the cruise drag reduction was attributable to the elimination of the large, external flap hinges and actuators. The system study also pointed out the lack of data available on the effectiveness of gap-less leading-edge device combined with active flow control.

The efficiency of an active high-lift device can be expressed in terms of "lift gain factor", which is defined as the ratio between the increase in lift-coefficient due to the active circulation control system and the jet momentum coefficient required to obtain that gain. The status of published lift gain factors was recently reviewed by Radespiel, Ref. [143]. The lift gain factor was first introduced by Poisson-Quinton and Lepage to describe the loss of efficiency that occurs for some configurations at high blowing (the condition also known as supercirculation regime) [134]. Later, in 1962, a lift gain factor of 10 at $Re = 0.8 \cdot 10^6$ was measured by Thomas [190]. This limited efficiency was mostly caused by the use of a very thick jet. Even lower lift gain factors were obtained in the same year by Gersten and Löhr with a leading-edge blowing configuration [46]. In 1984, however, Englar proved that larger gains were possible with a blown 23% chord high-lift flap. Recently, in 2007, the impact on the lift gain factor of blowing slot height, flap angle and Coanda contour, along with the blowing rate, were quantified by Radespiel [143]. Based on this experience, Jensch obtained lift gain factors around 60 with a steady Coanda jet configuration, at a maximum lift coefficient of 4 [67]. However, the lift gain factor decreased rapidly with higher lift coefficients. In the present work, the lift gain factor is employed to evaluate the effects of the different designs on the airfoil efficiency.

2 Test Case and Simulation Approach

2.1 The Coanda Flap Configuration

2.1.1 Flow Physics

The Coanda effect can be seen as a particular application of the capability of a flow to follow a convex surface while facing an adverse pressure gradient [116]. This effect lasts until boundary layer separation occurs and it is enhanced by the flow momentum. The term "Coanda effect" is typically employed when a stream of accelerated flow is directed tangentially over a convex surface and entrains the surrounding slower flow along the wall. In the present case, a thin air jet is tangentially blown over the shoulder of a 65° flap to delay or completely avoid boundary-layer separation. According to Poisson-Quinton and Lepage [134], a suitable quantity to characterize the jet in relation to its effects on the surrounding flow is the jet momentum, typically expressed in terms of momentum coefficient. The momentum coefficient is defined as the ratio between the thrust force produced by the jet and the freestream dynamic pressure multiplied by a reference area.

$$C_\mu = \frac{F_\mathrm{j}}{q_\infty S_\mathrm{ref}} = \frac{U_\mathrm{j}\dot{m}_\mathrm{j} + (p_\mathrm{j} - p_\mathrm{a})A_\mathrm{j}}{\frac{1}{2}\rho_\infty U_\infty^2 S_\mathrm{ref}} \tag{2.1}$$

where p_a is the local static pressure outside the blowing nozzle. For subsonic jets, the blowing air is expanded to p_a within the nozzle, and the pressure term of the jet thrust is equal to zero. However, if the ratio between the external pressure and the plenum pressure falls below the Laval pressure ratio of 0.528, the convergent nozzle chokes and limits the exit Mach number to $M_\mathrm{j} = 1$. Under these conditions, the jet static pressure is higher than the external one, and the pressure term of the jet thrust assumes positive values. For the nozzle geometry employed in the present work, such compressibility effects become significant from $C_\mu \approx 0.05$.

Figure 2.1 illustrates the operating principle of the Coanda jet. The trajectory and thickness of the tangentially-blown jet is determined by two counteracting effects. On the lower side, the high-momentum stream follows the convex surface of the flap thanks to a thin boundary layer (Coanda effect). On the upper side, the jet momentum is diffused by turbulent mixing into the outer flow, which is therefore accelerated along the direction of the jet (flow entrainment). In particular, the mixing between the two streams is strongly affected by the wake of the nozzle lip. Such a low-momentum region is generated by the thick boundary layer developed along the suction side of the main part of the airfoil and depends on the angle of attack and the leading edge configuration. In this scenario, the flow topology over the Coanda flap is determined by three co-dependent factors:

- Jet momentum coefficient. A high jet momentum enhances both the attachment

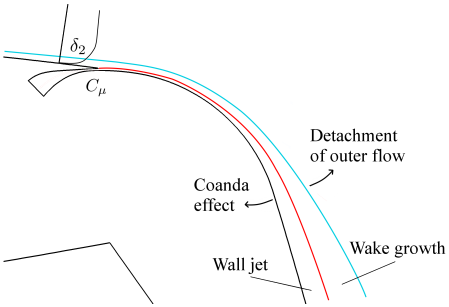

Figure 2.1: Operating principle of a Coanda flap.

of the Coanda jet to the flap surface and the mixing with the outer flow. The interaction between these two effects is discussed in the following sections, along with the influence of the leading-edge configuration and the angle of attack.

- Leading-edge configuration. The characteristics of the flow that is mixed with the Coanda jet are essential for the operation of the active high-lift system. In particular, the momentum losses within the boundary layer upstream of the blowing slot have a strong detrimental effect on the efficiency of the system. These are primarily determined by the behavior of the flow at the leading edge.
- Angle of attack. The angle of attack has a double effect. At the leading edge, the circulation determines the stagnation point location, which affects the flow around the leading edge and consequently the boundary layer upstream of the blowing slot. Further downstream, the angle of attack determines the pressure gradient along the Coanda flap.

Figure 2.2 illustrates the flow evolution above the Coanda flap for two angles of attack at $C_\mu = 0.0245$, which is not sufficient to completely avoid flow separation from the flap. The interaction of the three factors mentioned above is visible in the different flow topologies above the flap. Velocity profiles show the structure of the flow at four different location along the flap, which are referred to as BL1, 2, 3 and 4. At high angles of attack, figure 2.2b, the viscous losses at the leading edge and the pressure gradient in streamwise direction degrade the momentum of the flow that reaches the blowing slot and is mixed with the jet, as shown by the velocity profiles at BL1. This causes also a slightly lower jet velocity with respect to the flow at lower angles of attack. At BL2, the outer flow and the jet are partially mixed, but the high velocity of the jet is still visible in the near-wall region for both angles of attack. A large momentum deficit can be observed at $\alpha = 18.0°$ around $h/c = 0.01$. Note that this distance from the wall is much larger than the jet thickness, which suggests that the lower region of the boundary layer developed along the main wing is accelerated by the Coanda jet and a momentum deficit remains in the upper region of the boundary layer. This area of low kinetic energy cannot overcome the adverse pressure gradient along the flap and evolves in a separation between the lower and the upper region of the mixing layer, as shown by the profiles in BL3 and BL4 and in figure 2.2b. In the case of $\alpha = 0.0°$, the flow at BL2 does not present such a large momentum deficit thanks to the thinner boundary layer of the outer flow. As a consequence, the reverse flow appears

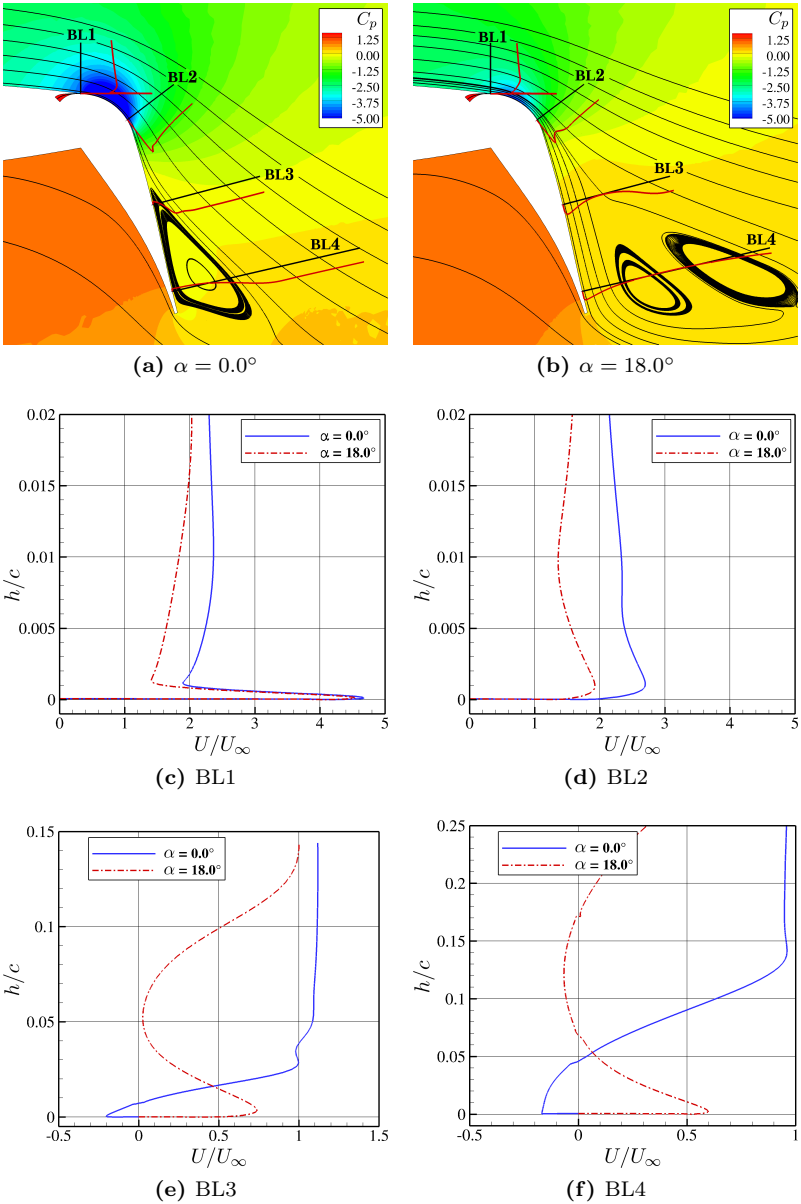

(a) $\alpha = 0.0°$ **(b)** $\alpha = 18.0°$

(c) BL1 **(d)** BL2

(e) BL3 **(f)** BL4

Figure 2.2: Evolution of the interaction between the Coanda jet and the outer flow at high angles of attack for low blowing rates, $C_\mu = 0.0245$, $Re = 12 \cdot 10^6$, $M = 0.15$.

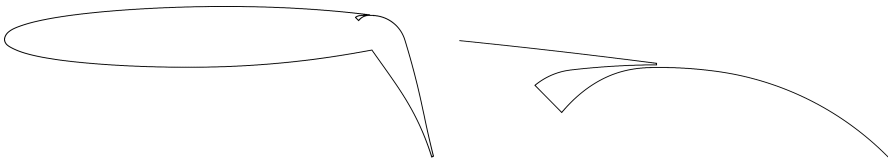

(a) DLR F15 airfoil, modified with the 65° active Coanda flap

(b) Close up of the blowing slot

Figure 2.3: DLR-F15 transonic airfoil equipped with an internally-blown Coanda flap: baseline of the present work.

between the jet and the wall, causing the typical flow separation topology shown in figure 2.2a. A higher jet momentum coefficient would enhance the momentum transfer to the outer flow and delay these phenomena or prevent them entirely.

2.1.2 Coanda-Flap Design

Previous Work

The present Coanda flap configuration is the result of previous numerical and experimental work that aimed at improving the device efficiency by careful design adjustments of the trailing edge configuration while keeping the leading-edge geometry fixed [67, 66, 132]. The free flow conditions employed during these previous analyses were $Re = 20 \cdot 10^6$ and $M = 0.15$. From the study, it emerged that the blowing slot height, the jet momentum and the flap deflection angle are the most important design parameters [66]. Required jet momentum and flap deflection angle increase for an increased target lift; whereas the optimal slot height should be determined based on considerations about the power source of the flow-control system, as discussed in the next section. Another important parameter is the flap length, which should be chosen between 25% and 30% of the airfoil chord [67]. The study also proved that the curvature of the flap suction side, used as Coanda surface, has modest effect on the system efficiency. Curvature radii about 0.07 times the chord length are reasonable design choices. The upper and lower boundaries of the blowing slot were designed parallel to each other, at the exit section, and a contraction rate of 15 was given to the internal duct shape in order to obtain a realistic velocity profile. The transonic airfoil DLR-F15 equipped with the Coanda flap resulting from these design choices and a 65° flap deflection angle is illustrated in figure 2.3. The highest lift gain factor (lift gain over blowing momentum) is typically obtained by adapting the blowing momentum coefficient to the flap deflection angle, in order to achieve the minimum momentum that provides attached flow until the trailing edge. For the configuration tested by Jensch in [67] and [66], the optimal jet momentum coefficients were 0.025 and 0.078, for flap deflection angles of 50° and 80° respectively. With the flap set at 50° and a lift coefficient around 4, a lift gain factor of 66 was obtained, which was reduced to 48 for a flap deflection of 80° and a lift coefficient of 6. Another meaningful parameter to characterize the level of actuation of

the Coanda flap is the velocity ratio between the jet and the freestream flow, which in these cases were ~ 4.4 for $C_\mu = 0.025$ and ~ 6 for $C_\mu = 0.078$. During the preliminary design studies, it was also noticed that the angle of attack of maximum lift drops significantly at higher blowing rates, as shown in figure 2.4. This is due to the rapid growth of the suction peak at the leading edge and the adverse pressure gradient along the suction side of the airfoil with the angle of attack. The resulting thick boundary layer upstream of the blowing slot creates a large momentum deficit in the flow mixing region above the Coanda surface, which is detrimental to the efficiency of the system. Manipulating the flow at the leading edge by means of additional blowing devices succeeded in delaying the angle of maximum lift, but it decreased the lift gain factor because of the higher overall blowing momentum requirements, as briefly described in section 1.3.4.

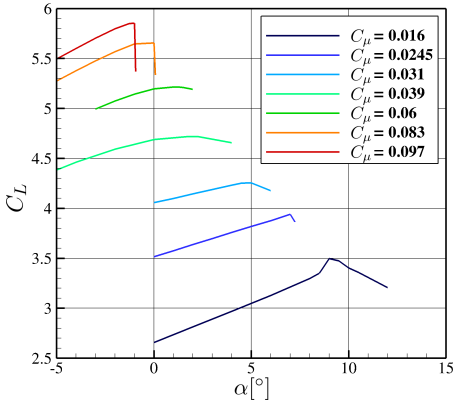

Figure 2.4: Effect of the jet momentum on the angle of maximum lift for the DLR F15 airfoil with 65° flap angle, computed for $Re = 12 \cdot 10^6$, $M = 0.15$.

Effects of the Slot Height

During the present work, new effort was undertaken to adapt the Coanda-flap configuration to a possible future integration into an aircraft system structure. For this purpose, the on-board supply of compressed air is a primary issue and the adopted solution also affects the design of the Coanda flap. One possibility is to spill air from the low-pressure engine compressor, which would however cause a reduction of the engine thrust. In this case, it would be appropriate to design the active high-lift system aiming at minimizing the Coanda jet-momentum requirement, as the jet momentum coefficient would directly represent the reduction in engine thrust. On the other hand, if the compressed air is obtained by other means, e.g. a dedicated compressor, the power of the Coanda jet may be a more meaningful design driver. To estimate the impact of this choice on the flap design, different slot heights are tested here by tuning the plenum total pressure in order to obtain $C_{L_{\max}} = 5.0$ (see figure 2.5). The resulting jet requirements were then computed with the following

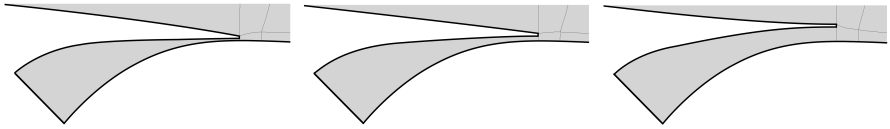

(a) $h_\mathrm{s} = 0.25\, h_{\mathrm{s}_\mathrm{ref}}$ **(b)** $h_\mathrm{s} = h_{\mathrm{s}_\mathrm{ref}} = 0.06\%$ c **(c)** $h_\mathrm{s} = 3.0\, h_{\mathrm{s}_\mathrm{ref}}$

Figure 2.5: Some of the tested blowing nozzles with different slot heights.

expressions:

$$\begin{aligned} C_\mu &= \frac{F_\mathrm{j}}{q_\infty S_\mathrm{ref}} = \frac{U_\mathrm{j}\dot{m}_\mathrm{j} + (p_\mathrm{j} - p_\mathrm{a})A_\mathrm{j}}{\frac{1}{2}\rho_\infty U_\infty^2 S_\mathrm{ref}} \\ C_\mathrm{Power} &= \frac{E_\mathrm{j}\dot{m}_\mathrm{j} + p_\mathrm{j}U_\mathrm{j}A_\mathrm{j} - (E_\mathrm{a}\dot{m}_\mathrm{a} + p_\mathrm{a}U_\mathrm{a}A_\mathrm{a})}{\frac{1}{2}\rho_\infty U_\infty^3 S_\mathrm{ref}} \end{aligned} \tag{2.2}$$

where $E = c_v T + \frac{U^2}{2}$. The power computation is based on the conservation of total energy and mass flow rate for a virtual control volume in which the flow above the blowing slot represents the inflow pressure and the jet represents the outflow condition. Therefore, the inlet density and temperature are computed considering an isentropic compression from the external stagnation pressure, $p_{\mathrm{a}_\mathrm{t}}$, to the jet stagnation properties, $p_{\mathrm{j}_\mathrm{t}}$ and $\rho_{\mathrm{j}_\mathrm{t}}$. A_a represents the inlet area of the virtual volume and is obtained by imposing conservation of the mass flow $\dot{m}_\mathrm{j}$:

$$\begin{aligned} \rho_{\mathrm{a}_{\mathrm{t,iso}}} &= \left(\frac{p_{\mathrm{a}_\mathrm{t}}\,\rho_{\mathrm{j}_\mathrm{t}}^\gamma}{p_{\mathrm{j}_\mathrm{t}}}\right)^{1/\gamma} & \rho_{\mathrm{a}_\mathrm{iso}} &= \rho_{\mathrm{a}_{\mathrm{t,iso}}}\left(1 + \frac{\gamma-1}{2}M_\mathrm{a}^2\right)^{\frac{1}{1-\gamma}} \\ T_{\mathrm{a}_\mathrm{iso}} &= \frac{p_\mathrm{a}}{\rho_{\mathrm{a}_\mathrm{iso}} R} & E_\mathrm{a} &= c_v T_{\mathrm{a}_\mathrm{iso}} + \frac{U_\mathrm{a}^2}{2} & A_\mathrm{a} &= \frac{\dot{m}_\mathrm{j}}{U_\mathrm{a}\,\rho_{\mathrm{a}_\mathrm{iso}}} \end{aligned} \tag{2.3}$$

Figure 2.6 shows the effects of different slot heights on stall angle of attack and jet requirements. As reference slot height, the one identified by Jensch [66] was employed, $h_{\mathrm{s}_\mathrm{ref}}/c = 0.0006$. $C_{L\mathrm{max}} = 5.0$ was obtained at higher angles with thinner jets and the required momentum coefficient rises linearly with the slot height, confirming that a thinner jet is more effective. On the other hand, a thinner jet requires higher velocity, which increases drastically the jet power. These results prove the importance of defining the correct design driver at the beginning of the geometry optimization. The present work was based on the slot height found in Ref. [66], as it is a good compromise between the two approaches.

2.2 Numerical Modeling

2.2.1 Governing Equations

All continuum fluid motions can be described by the general integral form of the Navier-Stokes equations. The integral system of equation is derived from the conservation principles

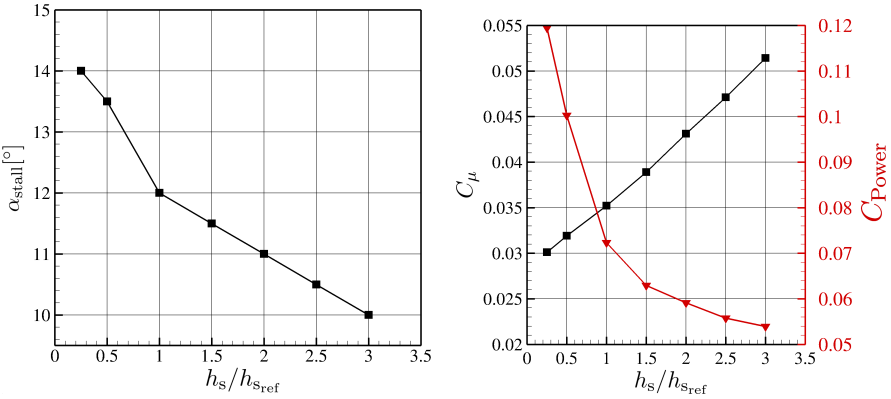

(a) Stall angle of attack **(b)** Blowing requirements

Figure 2.6: Effects of the blowing-slot height on the stall angle of attack and the blowing requirements to obtain $C_{L_{\max}} = 5.0$, for $\delta = 65°$, $Re = 12 \cdot 10^6$, $M = 0.15$.

of mass, momentum and total energy within an arbitrary finite region in space, referred to as control volume V limited by the surface S. The conserved quantities are here the unknowns of the problem, represented by the vector $\vec{W}$. A macroscopic description of the dynamic and thermodynamic behavior of the gas is adopted, meaning that all the scale lengths characteristic of the flow are large with respect to the mean free path of the molecules constitutive of the gas. It is also assumed that 1) the gas consists of only one species (atomic or molecular) or possibly of several species, given that these species are chemically inert and that the thermodynamic state of gas is at equilibrium and can be described using only one temperature, and 2) the density of the fluid is sufficiently low so that the effects of gravity can be neglected. Based on these assumptions, the conservation principles can be written as

$$\frac{\partial}{\partial t}\int_V \vec{W}\,\mathrm{d}V + \oint_S \overline{\overline{F}}\cdot\vec{n}\,\mathrm{d}S = 0 \tag{2.4}$$

where $\vec{n}$ is the outward-pointing unit normal vector and $\overline{\overline{F}}$ represents the density of fluxes through the volume boundary S. According to the conservation principles, the conservative variables, per unit volume, are the density ρ, the momentum $\rho\vec{U} = \rho[u, v, w]^T$, and the total energy ρE:

$$\vec{W} = \begin{bmatrix} \rho \\ \rho\vec{U} \\ \rho E \end{bmatrix} \tag{2.5}$$

The flux density can be considered as composed of two parts, the convective transport $\overline{\overline{F_c}}$,

and the viscous diffusion and dissipation $\overline{\overline{F_v}}$:

$$\overline{\overline{F}} = \overline{\overline{F_c}} - \overline{\overline{F_v}} \quad \text{with} \quad \overline{\overline{F_c}} = \begin{bmatrix} \rho\vec{U} \\ \rho\vec{U}\vec{U}^T + \overline{\overline{I}}p \\ \rho H\vec{U} \end{bmatrix} \quad \text{and} \quad \overline{\overline{F_v}} = \begin{bmatrix} 0 \\ \overline{\overline{\tau}} \\ \overline{\overline{\tau}}\vec{U} + \vec{q} \end{bmatrix} \tag{2.6}$$

The total energy equation has been written in terms of total enthalpy $H = E + p/\rho$, viscous stresses $\overline{\overline{\tau}}$ and heat flux $\vec{q}$. The equation system, however, involves quantities that are not known a priori, and need to be expressed as functions of the conservative variables. This additional set of information is commonly referred to as the "problem closure", and requires assumptions based on the nature of the fluid and its dynamic behavior. The present work employed standard air as working fluid, thus defining the problem closure based on the following assumptions:

- The thermodynamic characteristics of the fluid are deduced by the calorically perfect gas model, leading to the relations $p = p(\rho, \vec{U}, E)$ and $\vec{q} = \vec{q}(T)$. For this purpose, the equation of state $p = \rho RT$ is written considering the thermodynamic relations $e = c_v T$ and $E = e + \frac{|\vec{U}|^2}{2}$, where e is the specific internal energy and c_v is the specific heat coefficient at constant volume. Now, thanks to the definition of adiabatic index $\gamma = \frac{c_p}{c_v}$ and specific gas constant $R = (c_p - c_v)$, it is possible to obtain the required expression

$$p = \rho(\gamma - 1)\left(E - \frac{|\vec{U}|^2}{2}\right). \tag{2.7}$$

  The heat flux is described by Fourier's law for heat conduction $\vec{q} = -k\vec{\nabla}T$. The thermal conductivity can be expressed through the Prandtl number (Pr=0.72 for air), $k = \frac{\mu C_p}{\mathrm{Pr}}$, leading to

$$\vec{q} = -\frac{\mu\, R\, \frac{\gamma}{\gamma - 1}}{\mathrm{Pr}}\, \vec{\nabla}T. \tag{2.8}$$

  In case of perfect gas, the coefficient of dynamic viscosity μ can be considered dependent only on the temperature, since the effects of the pressure are negligible. For air this dependency is given by Sutherland's law

$$\frac{\mu}{\mu_\infty} = \left(\frac{T}{T_\infty}\right)^{\frac{3}{2}} \frac{T_\infty + 110.4}{T + 110.4} \tag{2.9}$$

  valid for temperatures within the range from 170K to 1900K.

- The fluid mechanical behavior of the gas defines the expression for the viscous stress tensor $\overline{\overline{\tau}}$. For a Newtonian fluid such as air, the dynamic viscosity describes the linear proportionality between the stress tensor and the strain rate [180]. The viscous stress tensor can thus be written as

$$\overline{\overline{\tau}} = \mu\left(\vec{\nabla}\vec{U}^T + \left(\vec{\nabla}\vec{U}^T\right)^T\right) + \left(\beta - \frac{2}{3}\mu\right)\overline{\overline{I}}(\vec{\nabla}\cdot\vec{U}) \tag{2.10}$$

  where β is the bulk viscosity.

2.2.2 Reynolds-Averaged Navier Stokes Equations

The direct solution of the Navier-Stokes equation system (2.4) yields to an exact representation of the motion of any fluid fulfilling the initial assumptions, as the system resolves every spatial and temporal scale without involving physical modeling. This approach is referred to as Direct Numerical Simulation, DNS. However, the required amount of storage and computational resources is beyond the capabilities of current calculators, for most practical applications at full-scale Reynolds numbers. A first simplification is introduced with the Large Eddy Simulation approach, LES, which is based on filtering the smallest scales in order to reduce the required spatial and temporal resolution. As a result, the large turbulent structures are resolved, whereas the smallest are modeled. This technique is rooted in the Kolmogorov theory, which categorizes the turbulent structures based on their dimension and dynamic behavior. The large scales carry most of the fluid kinetic energy and their dimensions and dynamics are strictly related to the problem in question. These large eddies receive energy from the velocity gradient of the mean flow and are anisotropic. The kinetic energy is then transferred to smaller and smaller structures in a cascade process. The smallest scales, called Kolmogorov scales, are responsible for the dissipation of the turbulent kinetic energy into heat and they are assumed isotropic and only dependent on the Reynolds number. These properties make the Kolmogorov scales important for the energy balance of the flow, but also relatively easy to model. However, although the LES approach is significantly less costly than the DNS, the required computational effort is still considerably high. A further simplification consists in entirely modeling the effects of turbulence. This is achieved by an average procedure that separates the flow into a mean flow and turbulent fluctuations. This approach is known as Reynolds-Averaged Navier Stokes [146], RANS, and allows to treat turbulence separately from the mean flow. Therefore, the conservation principles that define the Navier-Stokes equations are only applied to the mean-flow quantities reducing drastically the computational requirements. Hybrid LES/RANS methods are becoming popular, as they combine the higher accuracy of the LES approach for highly separated flows with the more affordable RANS approach used in boundary layers and shear layers. The coupling between the two techniques, however, still raises practical issues and makes the numerical set-up quite dependent on the specific simulated flow. For these reasons, the present work is performed solving the RANS and URANS (unsteady-RANS) equations, whose derivation is briefly described in the following paragraphs.

According to the decomposition proposed by Reynolds in 1883 [146], the flow field $\phi(x,t)$ is decomposed into a time-averaged mean $\overline{\phi}$ and the relative fluctuations ϕ'.

$$\phi = \overline{\phi} + \phi' \,, \qquad \text{with} \qquad \overline{\phi} = \frac{1}{\Delta t} \int_{t}^{t+\Delta t} \phi \, \mathrm{d}t \qquad \text{and} \qquad \overline{\phi'} = 0. \tag{2.11}$$

For compressible flows it is useful to introduce a density-weighted mean. This technique was proposed by Reynolds and extended to compressible flows by Favre [44].

$$\phi = \widetilde{\phi} + \phi'' \,, \qquad \text{with} \qquad \widetilde{\phi} = \frac{\overline{\rho\phi}}{\overline{\rho}} \qquad \text{and} \qquad \widetilde{\phi''} = 0. \tag{2.12}$$

Both average techniques are used to obtain the Navier Stokes equation system in the form

solved by TAU for the mean-flow field:

$$\begin{aligned} \rho &= \overline{\rho} + \rho', & \overline{\rho'} &= 0 \\ p &= \overline{p} + p', & \overline{p'} &= 0 \\ T &= \widetilde{T} + T'', & \overline{\rho T''} &= 0 \\ u_i &= \widetilde{u_i} + u_i'', & \overline{\rho u_i''} &= 0 \\ E &= \widetilde{E} + E'', & \overline{\rho E''} &= 0 \end{aligned} \tag{2.13}$$

where the subscript i represents here the three spatial coordinate directions.

The velocity products in the convective terms of the momentum and energy equations are solved as

$$\overline{u_i u_j} = \widetilde{u_i}\widetilde{u_j} + \overline{u_i'' u_j''} \tag{2.14}$$

where the non-linearity causes the fluctuation terms to remain in the averaged formulation as $\overline{u_i'' u_j''} \neq 0$, describing the statistical effect of the turbulence on the mean flow. For the present formulation, the fluctuation terms due to the convective fluxes will be included in the viscous fluxes. The resulting system is

$$\frac{\partial}{\partial t}\int_V \overline{\vec{W}}\,\mathrm{d}V + \oint_S \overline{\overline{\vec{F}}}\cdot\vec{n}\,\mathrm{d}S = 0 \tag{2.15}$$

known as the Reynolds-Averaged Navier-Stokes equation system. The unknowns vector and the fluxes are now

$$\overline{\vec{W}} = \begin{bmatrix} \overline{\rho} \\ \overline{\rho}\widetilde{\vec{U}} \\ \overline{\rho}\widetilde{E} \end{bmatrix} \qquad \overline{\overline{\vec{F}}} = \overline{\overline{\vec{F}_c}} - \overline{\overline{\vec{F}_v}} \tag{2.16}$$

with

$$\overline{\overline{\vec{F}_c}} = \begin{bmatrix} \overline{\rho}\widetilde{\vec{U}} \\ \overline{\rho}\widetilde{\vec{U}}\widetilde{\vec{U}^T} + \overline{\overline{I}}\,\overline{p} \\ \overline{\rho}\widetilde{H}\widetilde{\vec{U}} \end{bmatrix} \tag{2.17}$$

and

$$\overline{\overline{\vec{F}_v}} = \begin{bmatrix} 0 \\ \overline{\overline{\tau}} - \overline{\rho\vec{U}''\vec{U}''^T} \\ \overline{\overline{\tau}}\widetilde{\vec{U}} + \overline{\overline{\tau}\vec{U}''} - \overline{\rho h''\vec{U}''} - \overline{\rho\left(\widetilde{\vec{U}^T}\vec{U}''\right)\vec{U}''} - \frac{1}{2}\overline{\rho\vec{U}''^T\vec{U}''\vec{U}''} + \widetilde{\vec{q}} \end{bmatrix} \tag{2.18}$$

The new equation system is formally similar to the Navier-Stokes equation (2.4), with the exception of additional terms containing fluctuating quantities:

- $\overline{\rho\vec{U}''\vec{U}''^T}$ is the Reynolds stress tensor, which represents the propagation of momentum operated by the turbulent fluctuations;
- $\overline{\rho h''\vec{U}''}$ represents the turbulent heat transport;
- $\overline{\overline{\tau}\vec{U}''} - \frac{1}{2}\overline{\rho\vec{U}''^T\vec{U}''\vec{U}''}$ describes the turbulent diffusion and dissipation into heat.

Computing fluctuating components of the flow field requires additional information, or equations. This problem can be addressed either by directly computing the Reynolds stress

tensor or by modeling its effects on the mean flow. The first approach involves seven additional equations and rises considerably the computational cost. Modeling the turbulence effects, on the other hand, represents a considerable simplification, as it relies on strong assumptions that can limit the applicability of the specific model or parameter calibration. Differences between these two approaches in terms of computational effort, stability, and final results are briefly discussed at the end of this section, for the application investigated during this work.

Modeling the effects of turbulent fluctuations requires a relation between the mean-flow quantities and the Reynolds-stress tensor. Even before Reynolds illustrated the connection between turbulent stresses and velocity fluctuations, Boussinesq introduced a turbulent isotropic viscosity, $\mu^{(t)}$, (also referred to as eddy viscosity). Similarly to the molecular viscosity μ, this scalar quantity represents the linear proportionality between the turbulent stress tensor and the strain rate of the mean flow. The turbulent stresses can thus be defined as functions of the mean flow:

$$\overline{\overline{\tau^{(t)}}} = \overline{\rho \vec{U}'' \vec{U}''^T} = \mu^{(t)} \left(\widetilde{\vec{\nabla} \vec{U}^T} + \left(\widetilde{\vec{\nabla} \vec{U}^T} \right)^T - \frac{2}{3} \overline{\overline{I}} \left(\widetilde{\vec{\nabla} \cdot \vec{U}} \right) \right) - \frac{2}{3} \overline{\overline{I}} \widetilde{\rho} \widetilde{k}. \tag{2.19}$$

The prediction of physical flow phenomena such as boundary layer separation, wall friction or shock-boundary layer interactions, strongly depends on the choice of the turbulence model [202]. Most of first-order models rely on the assumption of local equilibrium to directly specify the turbulent viscosity in terms of known quantities of the mean flow. Among these, the algebraic models are robust and cheap, but their fundamental assumptions limit the physical complexity of the flows that can be adequately simulated. Two-equation models are independent of an algebraic length scale and take into account history effects through transport equations. A considerable number of two-equation models have been proposed in the literature and they have provided reasonably accurate results for a large variety of flows. However, this kind of models needs corrections in case of complex turbulent flows because they do not naturally account for streamline curvature and rotation, and they cannot describe the anisotropy of turbulence. Some modifications are also needed to predict adverse pressure gradient flows. To overcome some of these drawbacks Menter proposed the Shear Stress Transport (SST) correction for the $k-\omega$ model, which is tested in the present work. However, stiff source terms and complex boundary or freestream conditions restrict their general applicability. One-equation models seem to be a good compromise between the algebraic and two-equation models. In particular, the Spalart-Allmaras (SA) model, which solves a transport equation for the turbulent viscosity, provides fairly accurate results for a large range of flow topologies and has good numerical properties. The SA model with curvature and rotation correction, SARC, is the model generally employed in the present work.

The additional transport equations required to close the RANS problem can be specified in the form

$$\frac{\mathrm{d}}{\mathrm{d}t} \int_V \vec{W}^{(t)} \mathrm{d}V + \oint_S \vec{F}_c^{(t)} \cdot \vec{n} \mathrm{d}S - \oint_S \vec{F}_v^{(t)} \cdot \vec{n} \mathrm{d}S = \int_V Q^{(t)} \mathrm{d}V \tag{2.20}$$

where $\vec{W}^{(t)}$ is the vector of the turbulence variables. In particular, considering the transported quantities $e_1 \dots e_n$, the terms of the (2.20) are

- the vector of the turbulent variables $e_1 \dots e_n$:

$$\vec{W}^{(t)}_{(e_1 \dots e_n)} = [e_1 \dots e_n]^T \tag{2.21}$$

- the convective flux:

$$\oint_S \vec{F}^{(t)}_{c_{(e_1 \dots e_n)}} \cdot \vec{n} \mathrm{d}S = \oint_S \begin{bmatrix} e_1 \\ \vdots \\ e_n \end{bmatrix} \vec{U} \cdot \vec{n} \mathrm{d}S \tag{2.22}$$

- the viscous flux:

$$\oint_S \vec{F}^{(t)}_{v_{(e_1 \dots e_n)}} \cdot \vec{n} \mathrm{d}S = \oint_S \begin{bmatrix} \left(\mu + \dfrac{\mu^{(t)}}{\sigma_{e_1}}\right) \vec{\nabla} e_1 \\ \vdots \\ \left(\mu + \dfrac{\mu^{(t)}}{\sigma_{e_n}}\right) \vec{\nabla} e_n \end{bmatrix} \cdot \vec{n} \mathrm{d}S \tag{2.23}$$

  where $\sigma_{e_1} \dots \sigma_{e_n}$ are generally constant parameters, except in some models of the layer type, as Menter, where field functions are used instead.

The source term $\int_V Q^{(t)} \mathrm{d}V$ has a specific expression which depends on the model considered.

Spalart-Allmaras One-Equation Turbulence Model

The Spalart-Allmaras model is based on a single transport equation for the kinematic viscosity transform $\widetilde{\nu}$ which, far from the walls, merges with $\nu^{(t)} = \mu^{(t)}/\rho$ [178]. The principle is to relate the turbulence production to the mean flow vorticity. The equation for $\widetilde{\nu}$ results from a step by step construction by addition of terms intended for taking into account more and more physical effects. On the basis of a "convection = production + diffusion" form, the Spalart-Allmaras model adds the terms necessary to obtain a logarithmic zone in the boundary-layer velocity profile. The model was then calibrated using typical test cases, such as 2D-mixing-layers, wakes, and flat-plate boundary layers.

The Spalart-Allmaras transport equation is composed of the following terms, according to the form (2.20):

- the vector of the turbulent variable:

$$\vec{W}^{(t)}_{(\widetilde{\nu})} = \rho \widetilde{\nu} \tag{2.24}$$

- the convective flux:

$$\oint_S \vec{F}^{(t)}_{c_{(\widetilde{\nu})}} \cdot \vec{n} \mathrm{d}S = \oint_S \rho \widetilde{\nu} \vec{U} \cdot \vec{n} \mathrm{d}S \tag{2.25}$$

- the viscous flux:

$$\oint_S \vec{F}^{(t)}_{v_{(\widetilde{\nu})}} \cdot \vec{n} \mathrm{d}S = \oint_S \frac{1}{\sigma_{\widetilde{\nu}}} (\mu + \rho \widetilde{\nu}) \vec{\nabla} \widetilde{\nu} \cdot \vec{n} \mathrm{d}S \tag{2.26}$$

- the source term:

$$\begin{aligned} &\int_V \vec{Q}^{(t)}_{(\widetilde{\nu})} \mathrm{d}V = \\ &\int_V \left(C_{b1}(1 - f_{t2}) \widetilde{S} \rho \widetilde{\nu} + \frac{C_{b2}}{\sigma} \vec{\nabla}(\rho \widetilde{\nu}) \cdot \vec{\nabla} \widetilde{\nu} - \left(C_{W1} f_\omega - \frac{C_{b1}}{k^2} f_{t2} \right) \rho \frac{\widetilde{\nu}^2}{\eta^2} \right) \mathrm{d}V \end{aligned} \tag{2.27}$$

with:

$$\begin{cases} \widetilde{S} = |\vec{\omega}| + \dfrac{\widetilde{\nu}}{k^2\eta^2} f_{v2} \quad ; \quad f_{v2} = 1 - \dfrac{\chi}{1+\chi f_{v1}} \quad ; \quad \chi = \dfrac{\rho\widetilde{\nu}}{\mu} \\ f_W = g\left(\dfrac{1+C_{W3}^6}{g^6+C_{W3}^6}\right)^{1/6} \quad ; \quad g = r + C_{W2}(r^6 - r) \quad ; \quad r = \dfrac{\widetilde{\nu}}{\widetilde{S}k^2\eta^2} \\ f_{t2} = C_{T3}\exp(-C_{t4}\chi^2) \end{cases} \tag{2.28}$$

in which η is the wall distance and the constants take the values

$C_{b1} = 0.1355$ $\quad \sigma = 2/3$ $\quad C_{W3} = 2$ $\quad C_{T3} = 1.2$

$C_{b2} = 0.622$ $\quad k = 0.41$ $\quad C_{v1} = 7.1$ $\quad C_{t4} = 0.5$

$C_{W1} = C_{b1}/k^2 + (1 + C_{b2})/\sigma$ $\quad C_{W2} = 0.3$

Finally the eddy viscosity is evaluated with the following relations:

$$\mu^{(t)} = \rho\widetilde{\nu} f_{v1} \quad ; \quad f_{v1} = \frac{\chi^3}{\chi^3 + C_{v1}^3} \quad ; \quad \chi = \frac{\rho\widetilde{\nu}}{\mu} \tag{2.29}$$

Curvature Correction The Boussinesq relation between turbulent stresses and mean flow strain rate does not take into account effects of streamline curvature and system rotation. In order to improve the behavior of the Spalart-Allmaras turbulence model under these conditions, Spalart and Shur proposed a modification of the production term of the eddy-viscosity transport equation [179, 174]. The correction is controlled by the ratio of the magnitude of the strain rate tensor and the magnitude of vorticity, $r^* = \frac{\widetilde{S}}{|\vec{\omega}|}$. In shear layers the velocity distribution is dominated by the gradient in the normal direction, so that $r^* \approx 1$; whereas in the core of a vortex the flow approaches pure rotation, implying that $r \ll 1$. Therefore, in the equation (2.27) the production term $C_{b1}\widetilde{S}\rho\widetilde{\nu}$ becomes $C_{b1}\widetilde{S}\rho\widetilde{\nu} f_{r1}$, with

$$f_{r1} = (1 + C_{r1})\frac{2r^*}{1+r^*}\left(1 - C_{r3}\tan^{-1}(C_{r2}\widetilde{r})\right) - C_{r1} \tag{2.30}$$

and

$$\widetilde{r} = 2\omega_{ik}S_{jk}\left[\frac{DS_{ij}}{Dt} + (\varepsilon_{imn}S_{jn} + \varepsilon_{jmn}S_{in})\widetilde{\Omega}_m\right]\frac{1}{D^4}\,;\, D = \sqrt{\frac{1}{2}\left(|\vec{S}|^2 + |\vec{\omega}|^2\right)} \tag{2.31}$$

where $\widetilde{\Omega}_m$ is the rotation velocity of the reference system. The resulting curvature correction is named SARC (Spalart-Allmaras model for Rotation and Curvature effects). Test-case analyses and comparisons of the SARC correction with DNS, RSM, and experimental data can be found in [174].

Two-Equation Turbulence Model

Wilcox Model In $k-\omega$ models the transported quantities are the kinetic energy of turbulence k and the specific rate of dissipation $\omega = \epsilon/(\beta^* k)$ [202]. Where $\beta^* = 0.09$ is a constant and ϵ is the isotropic rate of dissipation. The resulting unknown variables vector

and source term, in the form of (2.20), are

$$\vec{W}^{(t)}_{(k\omega)} = [\rho k, \rho\omega]^T \qquad \text{with} \qquad \begin{cases} k: \text{ kinetic energy of turbulence} \\ \omega: \text{ specific rate of dissipation} \end{cases} \tag{2.32}$$

and

$$\int_V \vec{Q}^{(t)}_{(k\omega)}\,\mathrm{d}V = \int_V \begin{bmatrix} \left(\bar{\bar{\tau}}^{(t)}\left(\vec{\nabla}\vec{U}^T\right)\right) - \beta^*\rho k\omega \\ \left(\frac{\gamma}{\mu^{(t)}}\rho\bar{\bar{\tau}}^{(t)}\left(\vec{\nabla}\vec{U}^T\right)\right) - \beta\rho\omega^2 \end{bmatrix} \mathrm{d}V \tag{2.33}$$

where the eddy viscosity is defined as

$$\mu^{(t)} = \frac{\rho k}{\omega} \tag{2.34}$$

and the constants of the model are as follows:

$$\beta^* = 0.09 \qquad \sigma^* = 0.5 \qquad \sigma_{e_1} = \frac{1}{\sigma^*} \qquad \gamma = \frac{\beta}{\beta^*} - \sigma\frac{k^2}{\sqrt{\beta^*}}$$
$$\beta = 0.075 \qquad \sigma = 0.5 \qquad \sigma_{e_2} = \frac{1}{\sigma} \qquad k = 0.41$$

Baseline Menter Model The main problem with the Wilcox $k-\omega$ model is its sensitivity to the ω value at the edge of boundary layers and wakes. To avoid this problem, Menter developed the BSL (Baseline) model in order to preserve the good behavior of the Wilcox model in the near-wall area of boundary layers and to obtain an outer edge condition insensitive to the ω_∞ value. To do so, he replaced the Wilcox model in the outer region of the boundary layers and in wakes with the $k-\epsilon$ model from Launder and Sharma written in terms of $k-\omega$ variables [106]. This requires the introduction of a blending function F_1 between the models. Therefore, the source term of the model is written as

$$\int_V \vec{Q}^{(t)}_{(k\omega)}\mathrm{d}V = \int_V \begin{bmatrix} \left(\bar{\bar{\tau}}^{(t)}\left(\vec{\nabla}\vec{U}^T\right)\right) - \beta^*\rho k\omega \\ \left(\frac{\gamma}{\mu^{(t)}}\rho\bar{\bar{\tau}}^{(t)}\left(\vec{\nabla}\vec{U}^T\right)\right) - \beta\rho\omega^2 + 2\frac{\rho\sigma_\omega}{\omega}\vec{\nabla}k\cdot\vec{\nabla}\omega \end{bmatrix} \mathrm{d}V \tag{2.35}$$

where the constants are obtained through a weighted average of the constants of each model, using the blending function F_1:

$$C_{ste} = F_1 C_{ste1} + (1-F_1)C_{ste2} \tag{2.36}$$

with

$$\sigma_1^* = 0.5 \qquad \sigma_1 = 0.5 \qquad \beta_1 = 0.075 \qquad \sigma_{\omega 1} = 0$$
$$\sigma_2^* = 1.0 \qquad \sigma_2 = 0.856 \qquad \beta_2 = 0.0828 \qquad \sigma_{\omega 2} = 0.856$$
$$\beta^* = 0.09 \qquad k^* = 0.41 \qquad \gamma = \frac{\beta_i}{\beta^*} - \sigma_i\frac{k^{*2}}{\sqrt{\beta^*}}; \qquad i = 1,2$$

In particular the blending function F_1 is defined as

$$\begin{aligned} F_1 &= \tanh\left(\zeta^4\right) \\ \zeta &= \min\left[\max\left(\frac{\sqrt{k}}{0.09\omega y}\,;\,\frac{500\nu}{\omega y^2}\right) \quad ; \quad \frac{4\rho\sigma_{\omega 2}k}{D_{k\omega}y^2}\right] \\ D_{k\omega} &= \max\left(\frac{\rho\sigma_{\omega 2}}{\omega}\vec{\nabla}k\cdot\vec{\nabla}\omega \quad ; \quad 10^{-20}\right) \end{aligned} \tag{2.37}$$

SST Correction of the Menter Model The SST correction of Menter relies on the observation that in two-transport-equation models based on the eddy viscosity the ratio of the shear stress $\tau^{(t)}$ to ρk is equal to the quantity $a_1\sqrt{P_k/D_k}$ (ratio of production over dissipation of k, with $a_1 \approx 0.31$), whereas experimental measurements rather show $\tau^{(t)}/(\rho k) \approx a_1$ in a large part of the boundary layer. In the case of positive pressure gradient, the ratio P_k/D_k can be definitely larger than one, leading to over-estimate the shear stress. To cure this inconsistency Menter proposed to limit the eddy viscosity coefficient by using the function

$$\begin{aligned} \mu^{(t)} &= \frac{\rho k}{\max\left(\omega\,,\,\mathrm{rot}(\vec{U})F_2/a_1\right)} \qquad \text{where} \qquad a_1 = \sqrt{\beta^*} \\ F_2 &= \tanh\left(\iota^2\right) \qquad \text{with} \qquad \iota = \max\left(\frac{2\sqrt{k}}{0.09\omega y}\,,\,\frac{500\nu}{y^2\omega}\right) \end{aligned} \tag{2.38}$$

The SST correction of the Menter model can, in theory, correct any model of the $k-\epsilon$ type that tends to underestimate the effect of adverse pressure gradient.

Curvature Correction The curvature correction employed for the two-equation turbulence model was developed at the Dutch National Aerospace Laboratory (NLR). The original work aimed at reducing the production of eddy viscosity in vortex cores [12]. For this purpose two approaches were tested. One approach limited the production term of turbulent kinetic energy, whereas the other approach increased the production of specific turbulent dissipation rate. The second approach turned out to provide better results, so it was adopted for the present study. As for the one-equation turbulence model, the curvature sensor is based on $r^* = \frac{\widetilde{S}}{|\vec{\omega}|}$, which becomes lower than one when the vorticity is not accompanied by sufficient rate of strain. Therefore, the production term in the ω-equation is divided by $\min\left(r^{*2},1\right)$, which results in

$$\int_V \vec{Q}_{(k\omega-corr)}\mathrm{d}V = \int_V \begin{bmatrix} \left(\overline{\overline{\tau}}^{(t)}\left(\vec{\nabla}\vec{U}^T\right)\right) - \beta^*\rho k\omega \\ \gamma\max(\widetilde{S}^2,|\vec{\omega}|^2) - \beta\rho\omega^2 + 2\dfrac{\rho\sigma_\omega}{\omega}\vec{\nabla}k\cdot\vec{\nabla}\omega \end{bmatrix}\mathrm{d}V \tag{2.39}$$

Initial tests and calibration of the $k-\omega$ model with the NLR curvature correction can be found in [12] and [31].

Reynolds Stress Turbulence Models

The Boussinesq hypothesis is based on the assumption that the main axes of the Reynolds stress tensor and the strain-rate tensor are the aligned, and it exists a linear dependency

between them. Although these assumptions provide acceptable accuracy in quite a broad range of flows, there are cases where they are no longer valid, such as flows with sudden variations of the strain rate, high streamline curvature, rotating systems, or separated boundary layers [202]. Reynolds stress models assure good accuracy also under these conditions, since they are not based on the Boussinesq hypothesis and every $\tau_{ij}^{(t)}$ components is separately computed. Also, this enables the RSM model to resolve turbulence anisotropy. Algebraic Reynolds stress models compute the 6 components of the Reynolds stress tensor by means of local quantities, assuming local equilibrium between production and dissipation of turbulence. Approaches based on transport equations, on the other hand, are also able to model turbulence convection. However, the number of equations rises considerably, making this class of models numerically more expensive than the previous ones. The differential-equation model RSM JHh-v2 tested here is based on the work of Jakirlić and Hanjalić [63] and further calibrated by DLR and Technische Universität Braunschweig [20]. The direct computation of the $\overline{\rho}\widetilde{u_i''u_j''}$ is also referred to as second moment closure of the Navier Stokes equations. The resulting transport equations are

$$\begin{aligned} &\frac{\mathrm{d}}{\mathrm{d}t}\int_V \overline{\rho}\widetilde{u_i''u_j''}\,\mathrm{d}V + \oint_S \overline{\rho}\widetilde{u_i''u_j''}\,\vec{U}\cdot\vec{n}\mathrm{d}S = \\ &\int_V \left(\overline{\rho}P_{ij} + \overline{\rho}\Pi_{ij} - \overline{\rho}\epsilon_{ij} + \overline{\rho}D_{ij}^{v} + \overline{\rho}D_{ij}^{t} + \overline{\rho}M_{ij}\right)\cdot\mathrm{d}V \end{aligned} \tag{2.40}$$

where the production term can be exactly computed as follows:

$$\overline{\rho}P_{ij} = \overline{\rho}\widetilde{u_i''\vec{U}''}\cdot\vec{\nabla}\widetilde{u_j''} + \overline{\rho}\widetilde{u_j''\vec{U}''}\cdot\vec{\nabla}\widetilde{u_i''} \tag{2.41}$$

The other terms of the transport equation are the redistribution term, $\overline{\rho}\Pi_{ij}$, the dissipation rate, $\overline{\rho}\epsilon_{ij}$, the viscous and turbulent diffusion, $\overline{\rho}D_{ij}^{v}$ and $\overline{\rho}D_{ij}^{t}$, and the term that accounts for density variations due to compressibility, $\overline{\rho}M_{ij}$. Details about the employed RSM model can be found in [140].

2.2.3 Flow Solver DLR TAU-Code

The CFD solver employed to perform the present analyses is the DLR TAU-Code [85, 167, 30], which solves the Reynolds Averaged Navier-Stokes (RANS) equations with a compressible three-dimensional finite-volume approach. The mean-flow inviscid flux is discretized with a second order central scheme with scalar dissipation to assure stability, whereas a second order upwind Roe scheme is employed for the convective flux of the turbulence transport. A Lower-Upper Symmetric Gauss Seidel (LU-SGS) scheme is used to solve the backward Euler implicit system employed for the time stepping. The flow calculation algorithm is based on the dual grid approach, which is well suited for hybrid grids. Convergence is accelerated by local time stepping and multigrid techniques. The effects of turbulence on the mean flow are modeled adopting the approach developed by Spalart and Allmaras (SA) [178] with an additional correction to account for curvature and rotation effects (SARC) [179, 174]. This extension enhances the accuracy of the turbulence modeling in regions of the flow field where the streamlines present high curvature. This is of primary importance for the simulation of the Coanda effect, since the flow behavior is determined by viscous momentum transport in direction normal to the curved flap surface [131]. In this section, the main features of the solution approach are briefly described.

The integral conservation principles are applied to each control volume V_n, associated to

the mesh point n, defining the equation for the unknowns $\vec{W}_n$. A general numerical scheme can be defined as a system of ordinary differential equations in time by

$$\frac{\mathrm{d}}{\mathrm{d}t}\vec{W}_n\, V_n = -\sum_{Faces} \vec{F}^* \cdot \Delta\vec{S} + \vec{Q}_n^* V_n \equiv -\vec{R}_n \tag{2.42}$$

where the fluxes $\vec{F}^*$ represent the approximated fluxes on the faces of the control volume, and the source term $\vec{Q}_n^*$ is averaged in space within V_n. The specific form of the numerical flux $\vec{F}^*$ depends on the numerical scheme, which defines the way the time-averaged physical fluxes are approximated at each cell face. The right hand side defines the residual, which represents the balance of fluxes over the cell. This balance, in absence of source terms, must tend to zero at convergence for a steady-state problem.

Flux Approximation

In the present work, a central scheme and an upwind Roe scheme are employed to approximate the convective fluxes and the viscous fluxes, respectively. Both schemes are second-order accurate in space. The central scheme yields more physically accurate solutions but suffers from odd-even decoupling of the solution and wiggles at regions of high gradients. This problem is addressed by adding an artificial viscosity flux according to the method of Jameson, Schmidt, and Turkel [64], commonly referred to as JST scheme.

Central Discretization The principle of a central scheme is to compute the fluxes through the interface $n+\frac{1}{2}$ between the cells n and $n+1$ from the arithmetic average of the fluxes calculated in n and $n+1$ [7].

$$\vec{F}^*_{n+1/2} = \frac{1}{2}\Big(\vec{F}^*\big(\vec{W}_n\big) + \vec{F}^*\big(\vec{W}_{n+1}\big)\Big). \tag{2.43}$$

This approach was shown to be less dissipative than the flux of the averaged quantities in n and $n+1$ [84]. Introducing F^J to refer to the central-scheme numerical flux with JST artificial viscosity, the flux through the interface $n+\frac{1}{2}$ can be written as

$$\vec{F}^J_{n+1/2} = \vec{F}^*_{n+1/2} - \vec{d}_{n+1/2} \tag{2.44}$$

where the dissipation flux is defined by

$$\mathrm{d}_{n+1/2} = \epsilon^{(2)}_{n+1/2}\big(\vec{W}_{n+1} - \vec{W}_n\big) - \epsilon^{(4)}_{n+1/2}\big(\vec{W}_{n+2} - 3\vec{W}_{n+1} + 3\vec{W}_n - \vec{W}_{n-1}\big). \tag{2.45}$$

The coefficients $\epsilon^{(2)}_{n+1/2}$ and $\epsilon^{(4)}_{n+1/2}$ are used to locally adapt the dissipation flux. The dependence on the local solution is given by the scale factor $r_{n+1/2}$, which is defined as the average of the spectral radius of the Jacobian matrix associated to the solution in the cells n and $n+1$:

$$\begin{aligned} \epsilon^{(2)}_{n+1/2} &= k^{(2)} r_{n+1/2}\, \nu_{n+1/2} \\ \epsilon^{(4)}_{n+1/2} &= \max\big(0, k^{(4)} r_{n+1/2} - \epsilon^{(2)}_{n+1/2}\big) \end{aligned} \quad \text{with} \quad r_{n+1/2} = \frac{1}{2}\Big(\lambda(\overline{\overline{A}})^I_n + \lambda(\overline{\overline{A}})^I_{n+1}\Big) \tag{2.46}$$

where $\lambda\big(\overline{\overline{A}}\big)^I_n$ is the spectral radius of the Jacobian matrix $\overline{\overline{A}} = \frac{\partial\left(\vec{F}^*(\vec{W}_n)\cdot\vec{s}_n\right)}{\partial\vec{W}_n}$ calculated at the cell center with the averaged surface vector $\vec{s}_n = \frac{1}{2}(\vec{s}_{n+1/2} + \vec{s}_{n-1/2})$. The sensor

$\nu_{n+1/2}$ activates the second order dissipation only in presence of high gradients and can be obtained by the normalized second order pressure derivative:

$$\mu_n = \left| \frac{p_{n+1} - 2p_n + p_{n-1}}{p_{n+1} + 2p_n + p_{n-1}} \right| \qquad \text{from which} \qquad \nu_{n+1/2} = \max\left(\mu_n, \mu_{n+1}\right). \tag{2.47}$$

The accuracy of the numerical scheme is therefore reduced to first order in the proximity of discontinuities. In such areas the forth-order derivative term is switched off, as it would lead to overshoots of the solution. For transonic steady flows typical values of k^2 are around 0.5, while k^4 can vary from 0.01 to 0.03. For subsonic flows the second order artificial viscosity can be fixed to zero. In the case of incompressible flows the definition of ϵ_2 and ϵ_4 needs to be modified to adapt the dissipation fluxes to the convection fluxes.

Upwind Roe Flux The Roe upwind flux is based on a linearization of the Riemann problem at the interface of two cells, in order to reduce the computational effort. The linear matrix A^* is calculated as $\overline{\overline{A}}^*\left(\vec{W}_{n-1}, \vec{W}_{n+1}\right) = \overline{\overline{A}}(\vec{W}^*(\vec{W}_{n-1}, \vec{W}_{n+1}))$, where $\vec{W}^*$ is an intermediate state between $\vec{W}_{n-1}$ and $\vec{W}_{n+1}$. The variables of $\vec{W}^*$ are obtained by a density-weighted average, known as *Roe Average*, $< \cdot >_{\sqrt{\rho}}$:

$$\begin{aligned}
\rho^* &= <\rho^*>_{\sqrt{\rho}} = \sqrt{\rho_{n+1}\rho_{n-1}} \\
u_l^* &= <u_l^*>_{\sqrt{\rho}} = \frac{\left(\sqrt{\rho}u_l\right)_{n+1} + \left(\sqrt{\rho}u_l\right)_{n-1}}{\sqrt{\rho_{n+1}} + \sqrt{\rho_{n-1}}} \\
H^* &= <H^*>_{\sqrt{\rho}} = \frac{\left(\sqrt{\rho}H\right)_{n+1} + \left(\sqrt{\rho}H\right)_{n-1}}{\sqrt{\rho_{n+1}} + \sqrt{\rho_{n-1}}}.
\end{aligned} \tag{2.48}$$

Hence, the Roe flux at the interface $n + 1/2$ is defined by

$$\vec{F}_{n+1/2} = \frac{1}{2}\overline{\overline{A}}\Big(\vec{W}^*\left(\vec{W}_n, \vec{W}_{n+1}\right)\Big)\left(\vec{W}_n - \vec{W}_{n+1}\right) \tag{2.49}$$

This formulation is only first-order accurate in space, so it requires an extension to a higher order. The Van Leer's MUSCL (Monotone Upwind Schemes for Conservation Laws) method allows to extend an upwind scheme to the second order maintaining the TVD (Total Variation Diminishing) property. The extension to the second order with the MUSCL approach is based on the use of extrapolated boundary conditions to calculate the interface flux, considering a linear evolution of the variables u_n and u_{n+1} within the cells n and $n + 1$. In particular, the solution slope in each cell is calculated with respect to the local gradient of the solution field. This method provides a second order solution in space, but it involves fluctuations in high gradient regions, as new extrema may occur. To maintain the TVD condition, some slope limiters are required. For a more extensive description of these techniques the author recommends [90].

Time Integration

The time integration of the equation system (2.42) to a steady state is performed here with an implicit backward Euler scheme. This approach allows the use of larger time steps, with respect to an explicit scheme, at the cost of a higher computation effort per iteration. The resulting equation system is solved with a LU-SGS (Lower-Upper Symmetric Gauss Seidel) method, as derived from the work of Jameson and Turkel [65]. The convergence to steady

state is accelerated by a local time-stepping approach. Hence, the timestep is computed locally based on the user-defined Courant number and the cell dimension. The solution can thus evolve more rapidly in regions with larger cells. The damping of the residual is then improved with the multigrid technique. The residual of (2.42) vanishes when no further changes occur in the flow, which represents a steady-state solution. Time accurate simulations are based on a dual time stepping approach [64]. With this method, at each time step an internal loop brings the solution from an initial state, which is extrapolated from the previous time step, to a steady-state converged solution for the current time instant. Therefore, the internal loop can be accelerated using the acceleration techniques available for steady-state problems.

Low Mach Number Preconditioning

A freestream Mach number of 0.15 may represent a challenge for compressible solvers such as TAU. The issue arises from the large difference between the velocity of the flow and the speed of the acoustic waves, which increases the stiffness of the equation system. One approach to solve this problem improving convergence and accuracy is to use preconditioning. This technique consists in altering the eigenvalues of the compressible flow equation system in order to reduce the speed of the acoustic waves [192]. For the present simulations, however, preconditioning did not succeed as it induced instability in the numerical solution and prevented convergence to a steady solution [15]. These fluctuations disappeared when an unsteady time integration approach was used. This suggests that preconditioning makes the numerical solution more sensitive to local flow unsteadiness, e.g. at the blunt trailing edges of the flap and of the blowing nozzle lip where solution plots showed higher residuals. It is worth mentioning that the solution obtained by unsteady time integration and preconditioning did not show significant difference from the steady approach without preconditioning. Hence, all results presented in the following sections were obtained without preconditioning. Similar conclusions on the use of preconditioning for a circulation control airfoil at low Mach number were drawn by Allan and discussed in Ref. [1].

2.2.4 Numerical Grid

The spatial discretization has a major influence on the accuracy of the numerical solution and on the duration of the simulation. A good compromise, in terms of grid density, should be identified in order to achieve sufficiently accurate results at a reasonable computational cost. An estimation of the space discretization error was obtained here by employing the Richardson extrapolation [147, 148]. The analysis was based on combining and comparing the maximum lift coefficients obtained from three meshes with different point density [15]: about 70000, 230000 and 920000 points. All three grids predicted maximum lift at $\alpha_{\text{stall}} = 3.0°$ but delivered different lift coefficients: 4.410, 4.456 and 4.480, respectively. From these results, the Richardson extrapolation provided a maximum lift coefficient of 4.496, which represents an estimation of using an infinite number of grid points. With this value, it was possible to determine the space discretization errors caused by the three grid resolutions: 1.91%, 0.89% and 0.36%, respectively. As such, the middle value was considered as an acceptable compromise and the 230000-point grid was chosen for the following studies. This analysis was performed with a jet momentum coefficient of $C_\mu = 0.0356$, as this value represents the optimal blowing rate for the present Coanda flap configuration, as discussed in section 3.2.2. The grid is composed of a structured and an unstructured region, as shown in figure 2.7. The structured mesh covers the areas near the airfoil surface, where

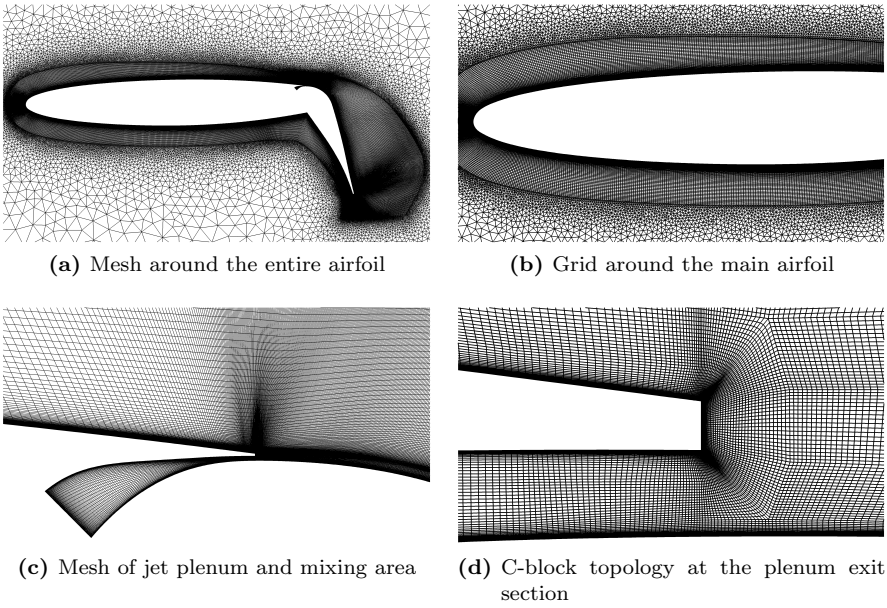

(a) Mesh around the entire airfoil

(b) Grid around the main airfoil

(c) Mesh of jet plenum and mixing area

(d) C-block topology at the plenum exit section

Figure 2.7: Numerical hybrid grid used for the two-dimensional analyses.

major viscous phenomena are expected; whereas an unstructured point distribution is used to discretize the rest of the numerical domain. The external boundaries of the domain are located at a distance of about 45 airfoil chords from the airfoil in all directions. The structured grid topology used near the walls makes possible achieving high resolution in the viscous sublayer. The cell height at the airfoil surface is such that y^+ is everywhere lower than 1. The extent of the structured layers is increased downstream of the Coanda flap, in order to accurately resolve the vortical structures that would occur in case of flow separation from the flap, as illustrated in figure 2.7a. Another important feature of the grid is the high point density along the pressure side of the main airfoil, see figure 2.7b. Such a high resolution is needed to accurately capture the flow attachment at the front stagnation point, which is expected to move quite far from the leading edge because of the high levels of circulation. A C-block topology is employed around the trailing edge of the flap and the edge of the lip over the blowing slot (figure 2.7d). With this topology it is possible to obtain high resolution only in regions of major interest and avoid propagation of high point density into areas where grid points are not needed and could slow convergence down [16].

2.2.5 Convergence Criteria and Boundary Conditions

Many of the simulation results presented in the following sections are partially separated flows and contain vortical structures. Such flows are in nature inherently unsteady, but the Reynolds averaging process together with the addition of artificial dissipation to stabilize

the numerical solution of the RANS equations can result in steady flow solutions. Such inaccuracy is considered a fair compromise for an acceptable computational cost and the integral performance of the airfoil, such as lift and drag, were proven to be reasonably accurate. Nevertheless, it was not always possible to establish a steady converged solution. The unsteadiness was visible in the convergence history of the lift coefficient, where constant amplitude fluctuations were present after an initial transient period. However, the maximum observed amplitude of the fluctuations was always well below 1% of the average lift coefficient, and time-accurate simulations do not result in significant variations. For this reason, it was decided that more costly time-accurate simulations were not necessary and average lift coefficients were used instead. Convergence was assumed achieved when the lift coefficient variation dropped below 10^{-6} within the last 500 iterations. Under this constraint, density residuals were reduced by about 5 orders of magnitude with respect to the initial state. The initial solution were obtained by applying the freestream flow condition to the entire numerical field.

The lift, drag and pitching moment coefficients were determined by integrating the pressure and shear stress distributions over the airfoil surface, excluding the jet plenum walls. Hence, the contribution from the jet momentum was not included. The Coanda jet was obtained by imposing the total pressure at the base of the modeled blowing nozzle. Previous studies showed that the total temperature of the jet has no significant impact on the jet behavior, so for the present work the jet total temperature was set equal to the farfield static temperature. The momentum coefficient was then computed by integrating flow quantities over the nozzle exit section:

$$C_\mu = \frac{1}{q_\infty S_{\text{ref}}} \int_0^{h_{slot}} |\vec{U}(y)|\, \rho(y)\, \vec{U}(y) \cdot \vec{n}\, \mathrm{d}y. \tag{2.50}$$

Note that the pressure component of the thrust generated by the jet is not considered in this formulation. This is the approach commonly employed in the literature for both subsonic and transonic jets, therefore it is used in this thesis for all jet momentum coefficients, although compressibility effects are observed from $C_\mu \approx 0.05$.

2.3 Numerical Validation

2.3.1 Previous Work

The overall numerical set-up employed in the present work was previously assessed by comparison to wind tunnel experiments [130, 132]. Figure 2.8 shows one typical comparison performed by Pfingsten and published in Ref. [130]. The numerical simulations were conducted with the same airfoil and a similar flap configuration as employed in the present work (the flap chord was 30% of the airfoil chord and the deflection was 45°, whereas the flap employed here is 25% of the airfoil chord set at 65°), using the same solver and the same numerical approach. The assessment study highlighted the need for a curvature correction module in order to improve the accuracy of the turbulence modeling in case of separated flow from the flap. Moreover, it was observed that the flow of the wind tunnel experiment could be accurately predicted only by three-dimensional simulations that included the sidewall boundary layers. In these cases, a maximum difference of 5% was observed between the numerical and experimental data, comparing the velocity profiles extracted just upstream of the blowing slot. The flow topologies were similar also near the tunnel walls, were complex vortical structures occurred.

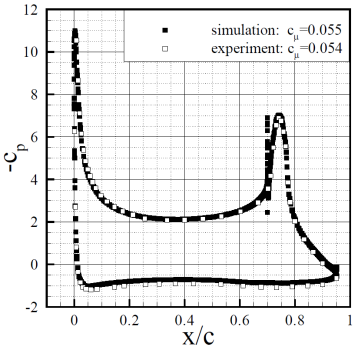

Figure 2.8: Experimental validation of C_p distributions obtained by numerical simulations, from Ref. [130], $M = 0.15$, $Re = 1 \cdot 10^6$, $\alpha = 0°$, flap deflection 45°.

2.3.2 Effect of Turbulence Modeling

A further estimation of the accuracy of the employed Spalart-Allmaras model [178] with rotation/curvature correction SARC [179] (in the following sections simply referred to as SARC) is here performed through a preliminary comparison with two other RANS turbulence models: 1)Menter-SST [106] with NLR curvature correction [12] and 2)RSM JHh-v2, developed by Jakirlić and Hanjalić [63] and calibrated by DLR and Technische Universität Braunschweig [20]. The comparison focuses on three blowing rates: a low blowing condition, where the flow is largely separated from the flap; the condition of optimal blowing, where the jet has enough momentum to nearly avoid flow separation; and a higher blowing condition, which assures fully attached flow. Moreover, two leading-edge configurations are tested, thus addressing all flow topologies relevant for the present work. The droop-nose configuration differs from the baseline in the suction peak at the leading edge. The adverse pressure gradient over the airfoil upper surface is much lower in the case of droop nose, causing a different development of the boundary layer in this area and different interactions between the Coanda jet and the outer flow.

The convergence behavior of the three models is significantly different, as the stability of the computation is strongly affected by the turbulence modeling. For most of the cases presented here, the SST-NLR and the RSM models only provide converged solutions when a time-resolving simulation approach is employed. A similar behavior was observed by Swanson and Rumsey and discussed in Ref. [185]. As a result, the required computation time increases considerably and makes these models much more expensive than the SARC model (a 10-hour simulation with steady SARC takes about one week with unsteady SST-NLR and two weeks with unsteady RSM). The results compared in this section, however, are obtained with the same temporal approach and time step for all methods. Figure 2.9 shows a typical convergence history, where the time is non-dimensionalized by the freestream velocity and the airfoil chord. A first phase of the simulation is performed with a large timestep, $\Delta T U_\infty/c = 1.5$, in order to accelerate the transient from the initial solution. Once the average of the lift coefficient fluctuations appears approximately constant, the timestep is reduced to $\Delta T U_\infty/c = 0.015$, which corresponds to about 67 timesteps per convective period. As a result, the lift-fluctuation amplitude is reduced, or disappears

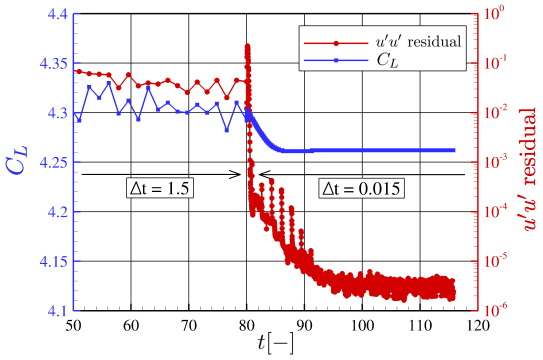

Figure 2.9: Convergence behavior of a RSM computation, baseline configuration, $C_\mu = 0.036$, $\alpha = 0.0°$, $Re = 12 \cdot 10^6$, $M = 0.15$.

Table 2.1: Jet momentum coefficients obtained with the tested turbulence models, for different jet boundary conditions.

$P_{\text{tot, plenum}} / P_\infty$	1.326	1.513	2.152
SARC, baseline	0.0247	0.0358	0.0597
SST-NLR, baseline	0.0251	0.0356	0.0598
RSM, baseline	0.0255	0.0357	0.0599
SARC, droop nose	0.0246	0.0357	0.0597
SST-NLR, droop nose	0.0244	0.0350	0.0598
RSM, droop nose	0.0254	0.0354	0.0599
Max Standard deviation	1.7%	0.8%	0.1%

completely, and the residuals drop by about 4 orders of magnitude. Note that the final value of the lift coefficient can differ significantly from the values obtained with the large timestep, which makes the second phase of the simulation necessary.

A first result comparison is based on the jet momentum coefficients obtained with the different turbulence models for the same plenum total pressure. The momentum coefficient of the Coanda jet is affected by the development of the flow inside the nozzle and by the flow condition outside, which depends on the flow field around the airfoil. The resulting C_μ deviations are limited to about 1.7%, as summarized in table 2.1.

Figure 2.10 reports the pressure coefficient distribution for some selected cases. The comparison shows for all cases a fairly good agreement, although some discrepancies appear at the leading edge and on the Coanda surface. The RSM model predicts generally a somewhat lower pressure in these areas, which corresponds to a slightly higher circulation. The droop-nose case at $C_\mu = 0.036$, figure 2.10d, exhibits the largest differences among the three turbulence models. In this case, a significantly lower circulation is obtained by the SST-NLR model, whereas the SARC model predicts attached flow until the trailing edge, yielding the highest circulation value. On the other hand, the flow separation for the low blowing cases, figures 2.10a and 2.10b, is predicted slightly earlier by the SARC model.

For three of these simulations, the RSM model did not provide a fully converged solution (figure 2.10a, 2.10b, 2.10d). In these cases, the Coanda jet exhibits unphysical fluctuations downstream of the nozzle exit section, which propagate over the Coanda surface. In particular, the low blowing cases, $C_\mu = 0.025$, seem critical in this respect. With $C_\mu = 0.036$ the fluctuations appear only for the droop nose configuration, whereas the baseline provides a very good agreement among the three turbulence models. The fluctuations seen for the highest blowing (2.10e, 2.10f), on the other hand, are due to compressibility effects related to the sonic condition of the jet.

More detailed information about the flow in the mixing area are reported in figures 2.11 and 2.12, which display the profiles of velocity and turbulent shear stresses on the Coanda surface at about 2% chord downstream of the blowing nozzle. The SARC model predicts higher turbulent stresses and low velocity than the other models. This behavior is a consequence of the higher diffusion of the SARC model, in agreement with what reported by Rumsey in Ref. [152]. The irregular velocity profiles of the non-converged RSM simulations suggest that the numerical problem affects the mixing between the two flows, producing unsteady structures not observed with other models. The low amount of Reynolds shear stresses shown in figures 2.12a, 2.12b, 2.12d for the RSM results confirms that these solutions are not physical. The mixing layers of the RSM computations of figures 2.10c and 2.10d are reported in 2.13a and 2.13b, respectively, showing an example of physical and unphysical RSM solution for the same jet momentum. The droop nose case, on the right hand side, exhibits unphysical local peaks of eddy viscosity near the nozzle exit, and disturbances that propagate in direction normal to the wall surface preventing the mixing layer to develop as occurs for the baseline case. Possible causes of these numerical issues can be the setting of boundary layer transition inside the blowing nozzle, which might in some cases induce numerical instability, or a too large time step employed for the time-accurate solution of the equation system.

The resulting lift performances are summarized in figure 2.14. The low blowing case exhibits a higher sensitivity to the turbulence model, since the circulation is strongly dependent on the flow separation from the flap or the detachment between the jet and the outer flow. At low angles of attack, the SST-NLR and RSM models do not predict flow separation from the flap, which results in higher lift compared to the separated SARC solution. At higher angles, all models predict a recirculation area between the jet and the outer flow. The flow topology and its effects on the overall circulation, however, is different for the three models. In SST-NLR and RSM solutions, a system of three vortices appears downstream of the flap, whereas the SARC simulation presents only two counter-rotating vortices. For higher blowing rates these differences are reduced, since the flow topology becomes more simple thanks to the enhanced capability of the jet to avoid flow separation.

In conclusion, this brief turbulence model analysis highlights some significant differences among the tested models, as well as some numerical issues observed in RSM computations at low blowing rates. A new set of numerical parameters should be tested to address the numerical instabilities, including new locations of the numerical tripping inside the blowing nozzle and smaller time steps. A solution to better evaluate the accuracy of the different turbulence models is including experimental data in the comparison, or testing numerically a similar configuration for which experimental data are available, e.g. [130]. For the purpose of validation of the numerical approach used for the present work, it can be concluded that the Spalart-Allmaras model with SARC curvature correction assures a good qualitative prediction of the main flow mechanisms and the resulting performances.

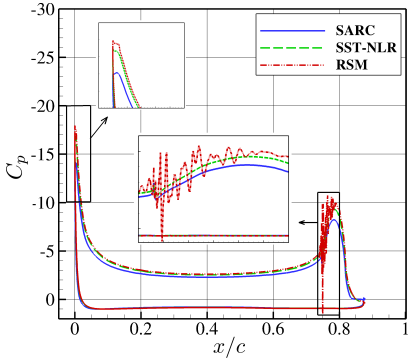

(a) Baseline, $C_\mu = 0.025$, $\alpha = 0.0°$

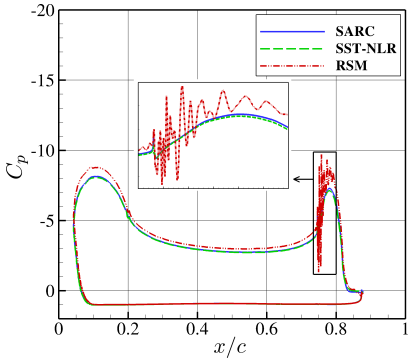

(b) Droop nose, $C_\mu = 0.025$, $\alpha = 10.0°$

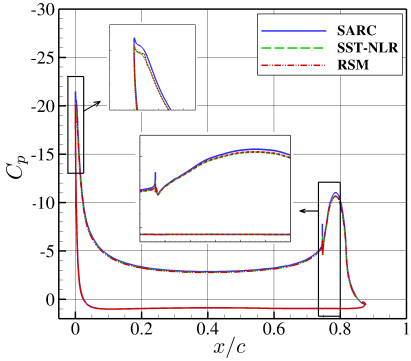

(c) Baseline, $C_\mu = 0.036$, $\alpha = 0.0°$

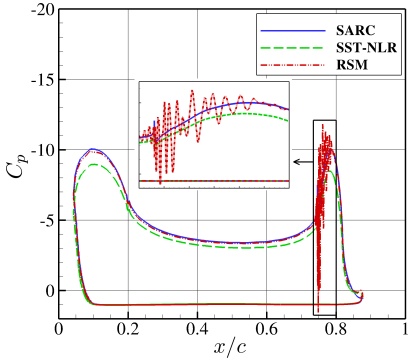

(d) Droop nose, $C_\mu = 0.036$, $\alpha = 10.0°$

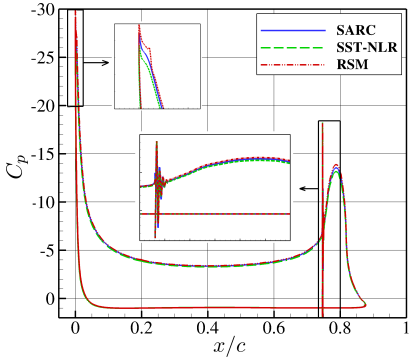

(e) Baseline, $C_\mu = 0.060$, $\alpha = 0.0°$

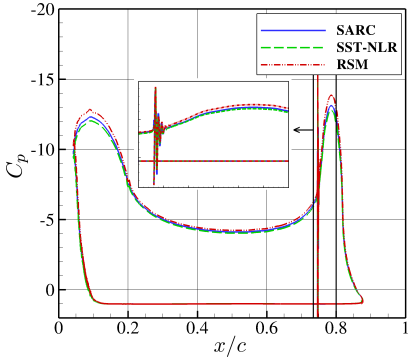

(f) Droop nose, $C_\mu = 0.060$, $\alpha = 10.0°$

Figure 2.10: Effect of the turbulence modeling on the pressure coefficient distribution.

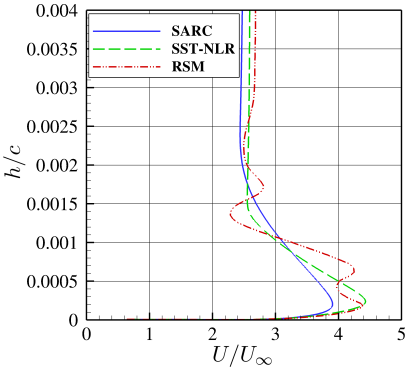

(a) Baseline, $C_\mu = 0.025$, $\alpha = 0.0°$

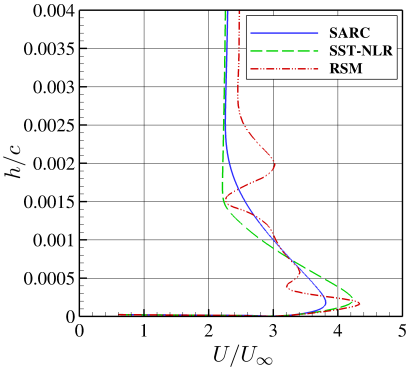

(b) Droop nose, $C_\mu = 0.025$, $\alpha = 10.0°$

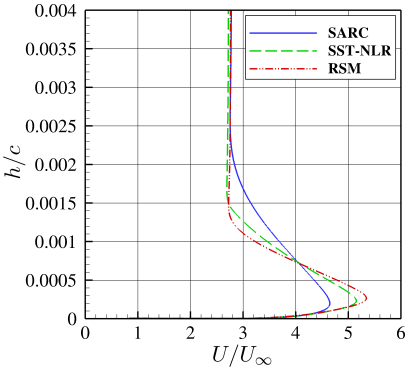

(c) Baseline, $C_\mu = 0.036$, $\alpha = 0.0°$

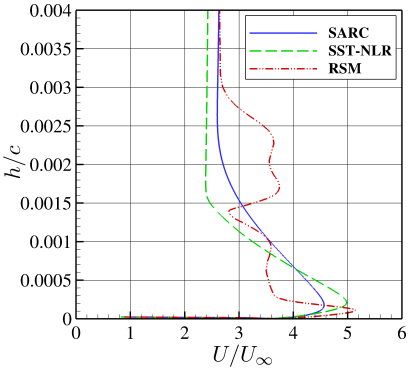

(d) Droop nose, $C_\mu = 0.036$, $\alpha = 10.0°$

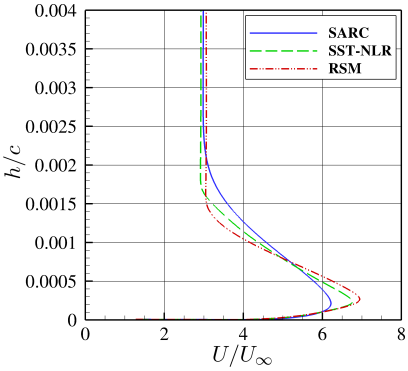

(e) Baseline, $C_\mu = 0.060$, $\alpha = 0.0°$

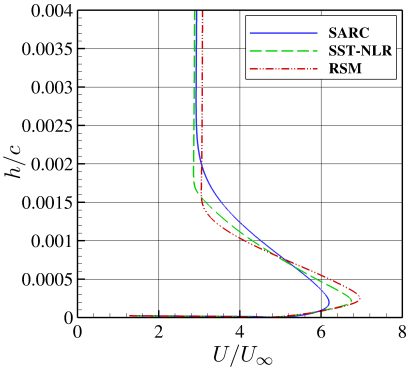

(f) Droop nose, $C_\mu = 0.060$, $\alpha = 10.0°$

Figure 2.11: Effect of the turbulence modeling on the velocity x-component over the Coanda surface.

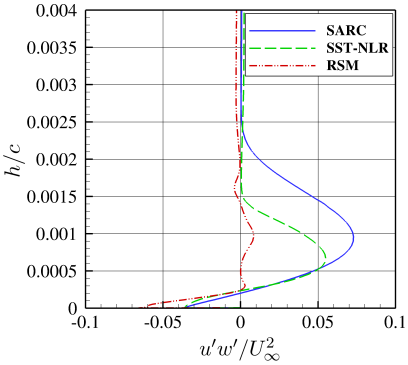

(a) Baseline, $C_\mu = 0.025$, $\alpha = 0.0°$

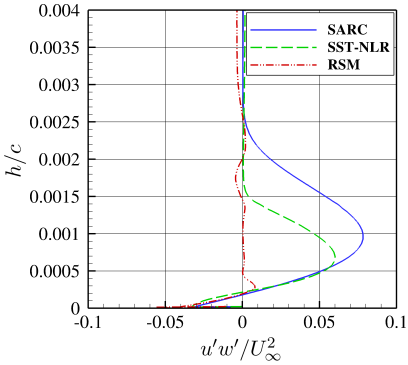

(b) Droop nose, $C_\mu = 0.025$, $\alpha = 10.0°$

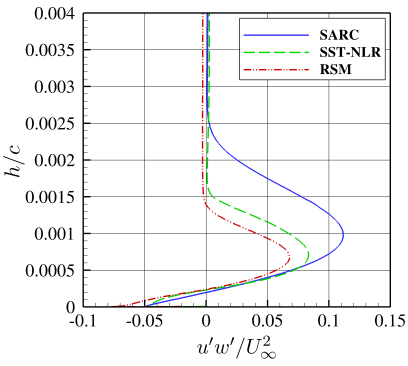

(c) Baseline, $C_\mu = 0.036$, $\alpha = 0.0°$

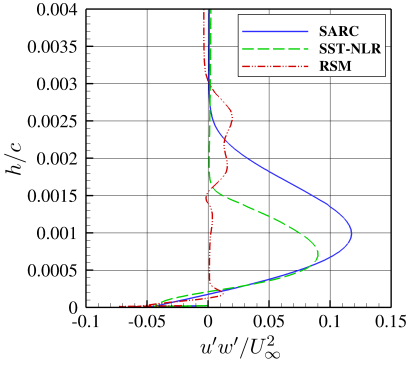

(d) Droop nose, $C_\mu = 0.036$, $\alpha = 10.0°$

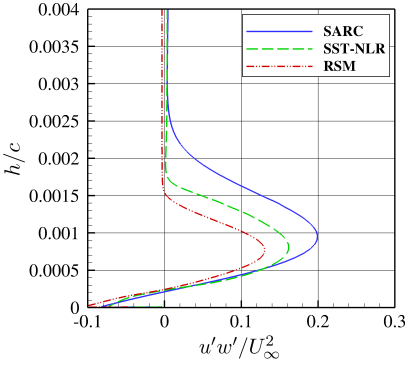

(e) Baseline, $C_\mu = 0.060$, $\alpha = 0.0°$

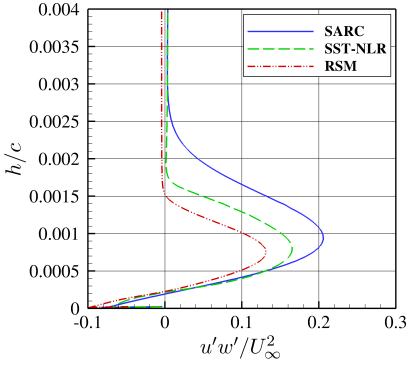

(f) Droop nose, $C_\mu = 0.060$, $\alpha = 10.0°$

Figure 2.12: Effect of the turbulence modeling on the shear stresses over the Coanda surface.

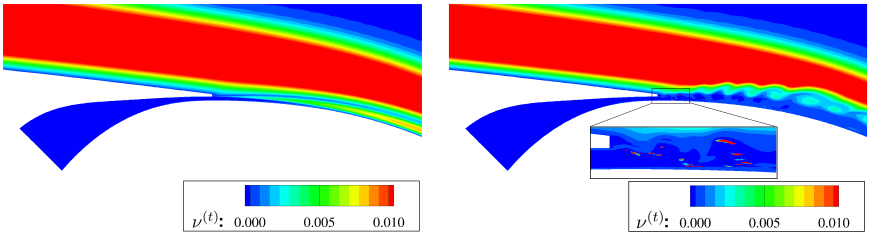

(a) RSM, baseline, $C_\mu = 0.036$, $\alpha = 0.0°$ **(b)** RSM, droop nose, $C_\mu = 0.036$, $\alpha = 10°$

Figure 2.13: Coanda jets simulated with the RSM turbulence model; a physical and well converged solution (left) and a numerically unstable case (right).

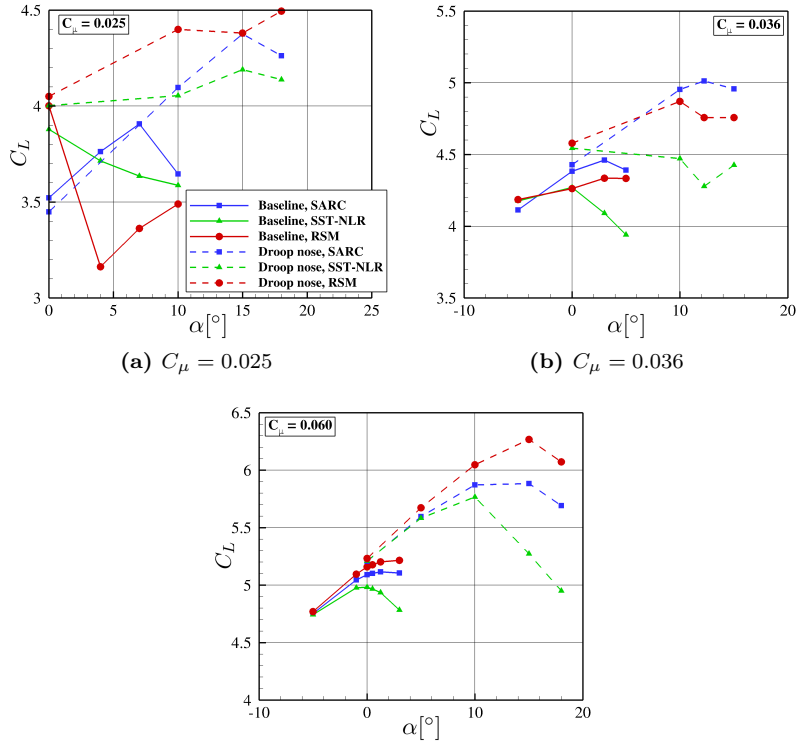

(a) $C_\mu = 0.025$ **(b)** $C_\mu = 0.036$

(c) $C_\mu = 0.060$

Figure 2.14: Lift performances predicted by the three URANS turbulence models.

3 Leading-Edge Configuration

The present chapter discusses the fundamentals of droop-nose design for active high-lift applications. As mentioned above, the need for a stall protection device arises from the high circulation yielded by the Coanda flap, which reduces significantly the stall angle of attack. The main reason behind the choice of developing a droop nose instead of using a conventional slat configuration is the higher noise emissions generated by the slat gap [137]. In the following sections, a geometrical sensitivity study describes the effects of the main geometrical parameters on the airfoil flow dynamics and lift performances for a fixed blowing rate [16]. Next, the resulting droop-nose geometries are compared with a conventional slat configuration and the baseline airfoil [15]. The analysis focuses on maximum lift performance at different blowing rates and the corresponding stall mechanisms. Finally, the efficiency of the different configurations is evaluated in terms of lift gain factor for the target lift coefficient $C_{L_{\max}} = 5.0$.

3.1 Droop-Nose Design

Following structural guidelines, the droop-nose configurations are designed keeping the length of the modified airfoil surface equal to the length of the baseline configuration. Studies aiming at assessing the potentials of flexible materials with stretching capabilities for high-lift generation can be found in Ref. [86], where Kühn and Wild discussed the benefit of a flexible droop nose in combination with a Fowler flap. In the present work, the search for an effective shape begins with a rigid deflection of the original nose shape. Next, the thickness is increased and the mean-line camber gradually augmented. The target quantities used to evaluate the performance of the different configurations are the maximum lift coefficient and the corresponding angle of attack. The flow conditions and flap settings are kept constant at $Re = 20 \cdot 10^6$, $M = 0.15$, $C_\mu = 0.06$ ($U_j/U_\infty = 6.1$), $\delta = 65°$, $L_f/c = 25\%$. The portion of airfoil chord modified to obtain the droop-nose configurations is fixed at $L_n/c = 20\%$.

3.1.1 Rigid Droop Nose

The first droop-nose configuration relies on an existing technology to create a gap-less leading-edge stall protection device. The new shape is obtained by rotating the first 20% of the airfoil chord around a rotation point, without altering its shape. The only skin deformation required for this configuration is at the hinge-cover sheet at the lower surface of the nose. Similar devices are currently employed in commercial transport aircraft, such as the Airbus A380, because of their effectiveness and mechanical simplicity. The enhancement of maximum lift and stall angles yielded by the rigid droop-nose configuration are shown in figure 3.1, where the angle β represents the nose deflection with respect to the baseline configuration. The maximum performance improvement is achieved for $\beta = 30°$, as larger deflection angles yield lower maximum lift and lower stall angles. Physical insight into the

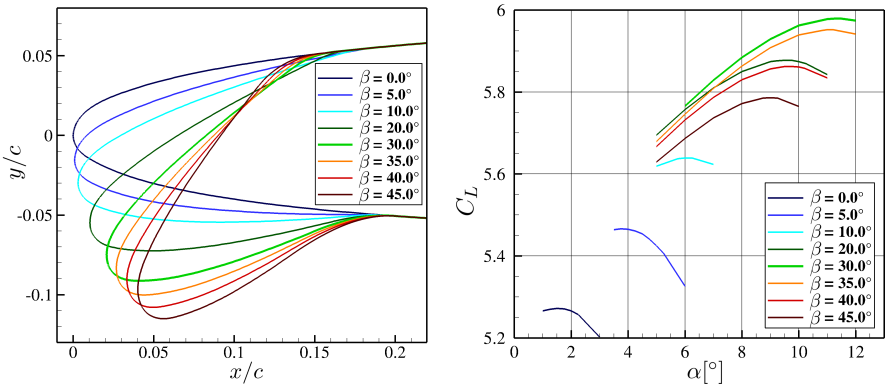

Figure 3.1: Shapes and performance of rigid droop-nose configurations, $Re = 20 \cdot 10^6$, $M = 0.15$, $C_\mu = 0.06$.

flow around the airfoil is provided by the pressure coefficient distributions reported in figure 3.2a. The C_p distributions describe a gradual load transfer from the leading edge to the high curvature region over the rotation point for increasing β. The effect of this behavior on the boundary layer is shown in figure 3.2b, where the momentum thickness of the boundary layer at 22% of the airfoil chord (just downstream of the hinge location) is reported for $\alpha = 6°$.

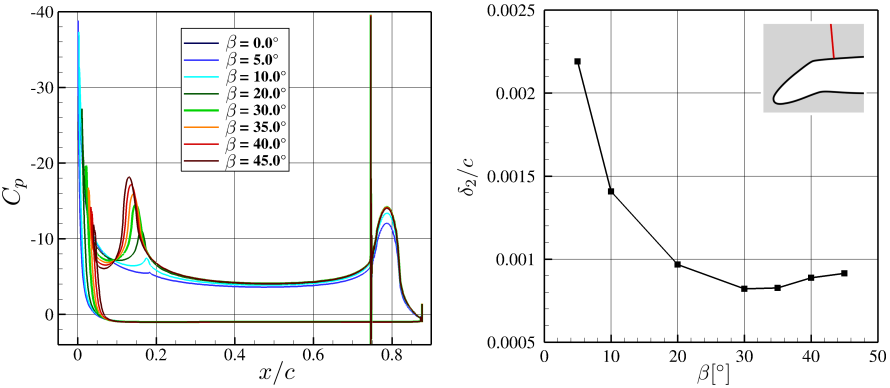

(a) Pressure coefficient distributions for different rigid nose settings

(b) Boundary-layer momentum thickness on the suction side at 22% chord

Figure 3.2: Pressure coefficient and boundary-layer momentum thickness for different rigid nose deflection angles, $\alpha = 6°$, $Re = 20 \cdot 10^6$, $M = 0.15$, $C_\mu = 0.06$.

The initial decreasing trend of the momentum thickness proves that the viscous losses upstream of this location are reduced by increasing the nose deflection until 30°; whereas the rising momentum deficit for higher nose angles shows the detrimental effect of the strong suction peak over the nose hinge. The increase of performance resulting from the nose deflection is also related to the reduction of the transonic area at the leading edge. For nose deflections lower than $\sim 25°$, the pressure coefficient at the leading edge is below -25.5, which is the critical value corresponding to sonic flow [15].

Figure 3.3a describes the effect of angle of attack variations on the load distribution. The higher circulation yielded by higher angles of attack reduces the pressure coefficient both at the leading edge and over the nose hinge. Nevertheless, the flow does not separate from the airfoil even at high flow incidence (figure 3.3b). As a result, a nose deflection of $\beta = 30°$ increases the maximum lift coefficient from 5.27 to 5.98 and delays the stall angle of attack from 1.5° to 11.3°. Such improvements, yielded by a rigid droop-nose device in combination with a Coanda flap, are significantly larger than those reported from applications of similar leading-edge devices on airfoils with conventional Fowler flaps [145].

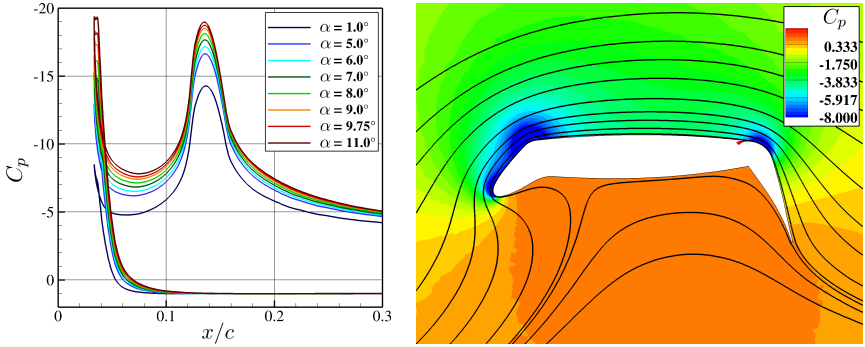

(a) Variation of pressure coefficient distribution with angle of attack

(b) Pressure coefficient flow field and stream lines in post-stall condition, $\alpha = 11°$

Figure 3.3: Pressure coefficient for increasing angle of attack and corresponding flow field at $\beta = 40°$, $Re = 20 \cdot 10^6$, $M = 0.15$, $C_\mu = 0.06$.

3.1.2 Thickness Increase

The pressure distribution over the airfoil can be further improved by employing actual deformation of the nose contour. In particular, the suction peaks at the leading edge and over the nose hinge can be significantly reduced by increasing the thickness of the droop nose. As described in Ref. [16], the new nose geometry is obtained by multiplying the distance of each point of the contour from the camber line by a function f such that

$$f(x_{\text{wingbox}}) = 1 \quad ; \quad \frac{\mathrm{d}f(x_{\text{wingbox}})}{\mathrm{d}x} = 0 \quad ; \quad f(x_{\text{leading-edge}}) = th_{\text{le}} \tag{3.1}$$

where th_{le} is the control parameter used to define different shapes. The resulting thickness increase is symmetric with respect to the camber line. For the configurations presented here, the thickness is increased with a parabolic function. Once the new thickness distribution is defined, the skin length is adjusted to meet the baseline-length requirement. This is performed by shifting each contour point in direction parallel to the camber line of a factor proportional to the distance from the wingbox. The process results in the shapes and performances shown in figure 3.4.

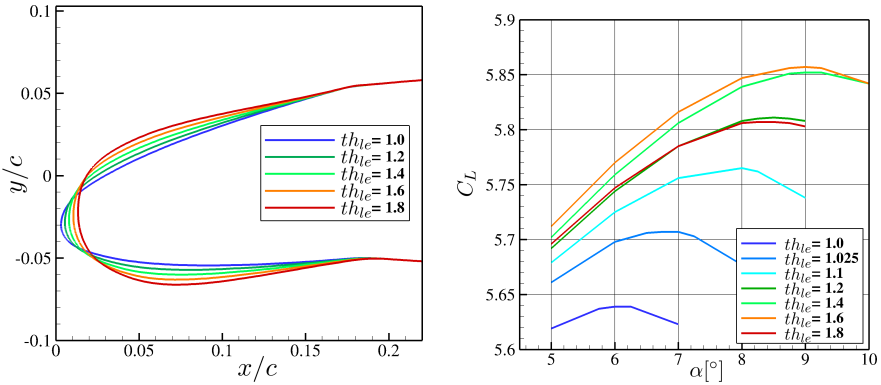

Figure 3.4: Thickness increase applied to a rigid nose deflected by $\beta = 10°$, shapes and performances, $Re = 20 \cdot 10^6$, $M = 0.15$, $C_\mu = 0.06$.

The thickness increase yields a reduction of the local curvature of the contour, which results in lower suction peaks and increased stall angles. Applied to a rigid nose deflected by 10°, the highest improvement is achieved with $th_{\mathrm{le}} = 1.6$, which leads to the performance reported in table 3.1.

Table 3.1: Effect of the thickness variation on the stall performance of a rigid nose deflected by 10°.

	$C_{L_{\max}}$	α_{stall} [°]
Droop nose $\beta = 10°$, $th_{le} = 1.0$	5.64	6.3
Droop nose $\beta = 10°$, $th_{le} = 1.6$	5.86	9.0

3.1.3 Camber Increase

A more effective surface curvature distribution can be achieved by gradually varying the mean-line camber rather than concentrating the camber increase at a hinge point. The first 20% of the airfoil chord is therefore modified by using a new camber line, which is

defined by a constant curvature radius. The control parameter is the angle of the camber line at the leading edge with respect to the x-axis, expressed by γ. The skin length is then adjusted with the same scaling method employed for the thickness variation and described in the previous section.

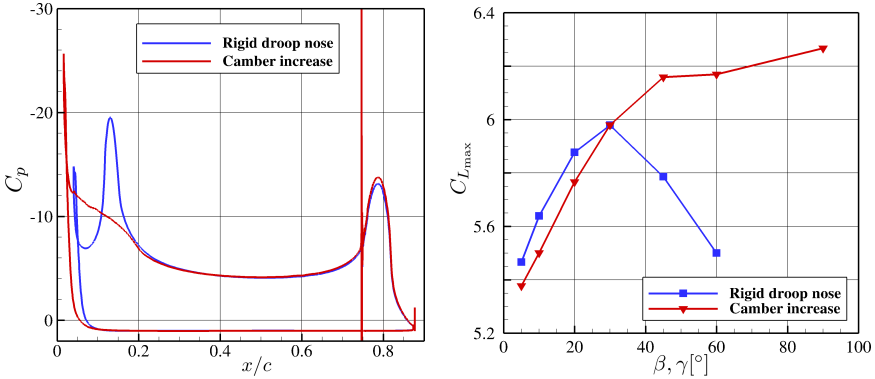

(a) Pressure coefficient distributions for equal leading edge angles: $\beta = \gamma = 30^\circ$, $\alpha = 5^\circ$

(b) Comparison based on maximum lift coefficient and leading-edge angle

Figure 3.5: Comparison between a gradual camber increase and a rigid nose deflection ($Re = 20 \cdot 10^6$, $M = 0.15$, $C_\mu = 0.06$).

Figure 3.5 reports a comparison between the pressure coefficient distributions and the resulting maximum lift performances obtained from the rigid droop nose and the smooth camber configuration. The performance of the rigid droop nose geometry is limited by the suction peak over the hinge, which causes substantial momentum losses for high nose deflection angles. A smooth camber increase solves this problem and yields much larger lift thanks to the possibility of using higher camber values. The best performance obtained by camber increase, without any thickness variation, is achieved with the highest curvature tested here, $\gamma = 90^\circ$, and is reported in table 3.2.

Table 3.2: Lift performance achieved by gradually increasing the mean-line camber to an angle of 90° at the leading edge.

	$C_{L_{\max}}$	$\alpha_{\text{stall}}[^\circ]$
Baseline configuration	5.27	1.5
Camber increase $\gamma = 90^\circ$	6.267	15.0

3.1.4 Camber and Thickness Increase

Combining thickness and camber variations leads to the final flexible droop-nose configuration investigated here, as illustrated in figure 3.6. Referring to the morphing techniques described above, the final geometry is defined by $th_{\mathrm{le}} = 1.6$ and $\gamma = 90°$ for the thickness increase and camber increase, respectively. Further studies aimed at optimizing the nose shape and revealed that using different curvature distributions or asymmetric thickness variations has little effects on the lift performance. Figure 3.7 displays a comparison between the baseline configuration and the final droop-nose design. The distributions of pressure coefficient represent stall conditions, and the resulting lift coefficients are reported in table 3.3. The pressure distributions show that the suction peak is drastically reduced by the droop-nose shape, and the low pressure is distributed over a larger surface. Moreover, the maximum pressure gradient is significantly lower, reducing the risk of boundary-layer separation. Also, this new load distribution results in different stall behaviors, as explained in the following sections [16]. The term "flexible droop nose" will be used to refer to the final droop-nose geometry described in this section, whereas "rigid droop nose" will refer to the shape described in section 3.1.1 with $\beta = 30°$.

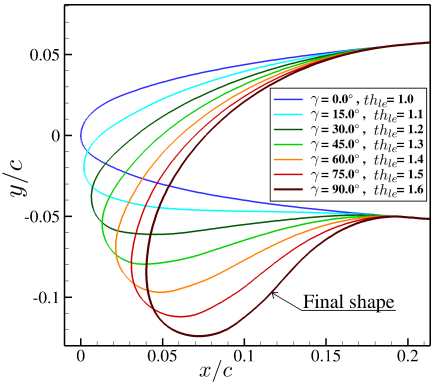

Figure 3.6: Flexible droop nose configurations obtained by thickness and camber variations.

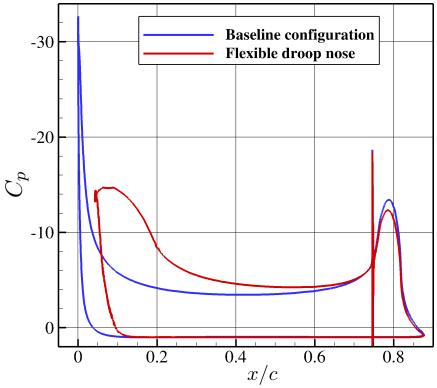

Figure 3.7: C_p distributions at stall conditions, $Re = 20{\cdot}10^6$, $M = 0.15$, $C_\mu = 0.06$.

Table 3.3: Improvements achieved by increasing the camber and the thickness of the first 20% of the airfoil chord.

	$C_{L_{\max}}$	$\alpha_{\mathrm{stall}}[°]$	$C_{D,\,\mathrm{stall}}$	$C_{M,\,\mathrm{stall}}$
Baseline configuration	5.27	1.5	0.0886	-2.184
Camber + thickness increase	6.30	15.0	0.107	-2.44
Relative variation	+19.5%	+13.5	+20.8%	-11.7%

3.1.5 Slat Configuration

The performance analysis of the different leading-edge configurations includes a conventional slat geometry for reference. The employed slat configuration was designed by Wild with the present airfoil, the DLR-F15, for a generic three-dimensional wing in landing configuration equipped with a trailing-edge Fowler flap [204]. Slat angle and gap were determined by using numerical optimization of the two-dimensional flow. Optimal settings for the application tested here would most probably be different because of the particularly high levels of circulation generated by the active flap. However, optimizing the slat configuration is not among the objectives of the present study, and the employed configuration is deemed representative of the flow features and performance trends that an optimized geometry would yield [15].

3.2 Aerodynamic Performances

3.2.1 Effects of the Leading-Edge Configuration on the Coanda Flap

In this section, the effects of variations of jet momentum and angle of attack on the flow behavior are investigated with four leading-edge configurations: the baseline, the rigid droop nose with $\beta = 30°$, the flexible droop nose with $\gamma = 90°$ and $th_{\mathrm{le}} = 1.6$, and the slat configuration. Boundary-layer velocity profiles and momentum thicknesses are evaluated near the trailing edge and over the blowing slot. Figure 3.8a shows the boundary layer momentum thickness just before the jet reaches the trailing edge for variations of flow incidence. An increase in jet momentum coefficient enhances the Coanda effect, thereby reducing the boundary-layer momentum thickness at the trailing edge. An increase of angle of attack also reduces the boundary-layer momentum thickness over the flap, since the higher adverse pressure gradient over the suction side of the airfoil increases the boundary layer thickness upstream of the blowing slot. As a result, a gradual detachment occurs between the outer flow and the jet, which enhances jet attachment to the wall. Examples of this phenomenon are discussed in the following sections.

The momentum thickness of the boundary layer upstream of the blowing slot is reported in Figure 3.8b for different blowing rates and angles of attack. It can be observed that an augmentation of the angle of attack induces larger viscous losses upstream of this location for all leading-edge configurations. The blowing rate, on the other hand, has different effects on the boundary layer depending on the nose geometry. In comparison to the baseline configuration, the droop-nose devices exhibit a significantly lower sensitivity to jet momentum variations (see also figure 3.9). In particular, the boundary layer thickness in the case of flexible droop nose remains nearly unchanged for variations of the blowing rate. This behavior is the key factor to explain the high performance yielded by the flexible droop-nose device, as discussed in section 3.2.2. The boundary-layer thickness of the slat configuration exhibits an opposite trend in relation to the blowing rate with respect to the other configurations, i.e. higher C_μ results in lower boundary-layer momentum thickness. This behavior is due to the increase of mass flow through the slat gap induced by the higher jet momentum. However, a higher circulation also induces greater viscous losses on the slat surface, which result in a larger momentum deficit in the slat wake (figure 3.9d at about h/c=0.25).

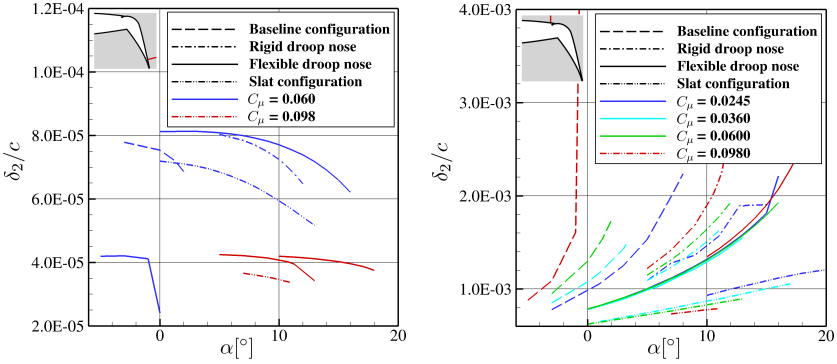

(a) Boundary layer momentum thickness at the trailing edge

(b) Boundary layer momentum thickness over the blowing slot

Figure 3.8: Momentum thickness of the boundary layer at the trailing edge and over the jet nozzle, for a range of C_μ and α, $Re = 12 \cdot 10^6$, $M = 0.15$ [15].

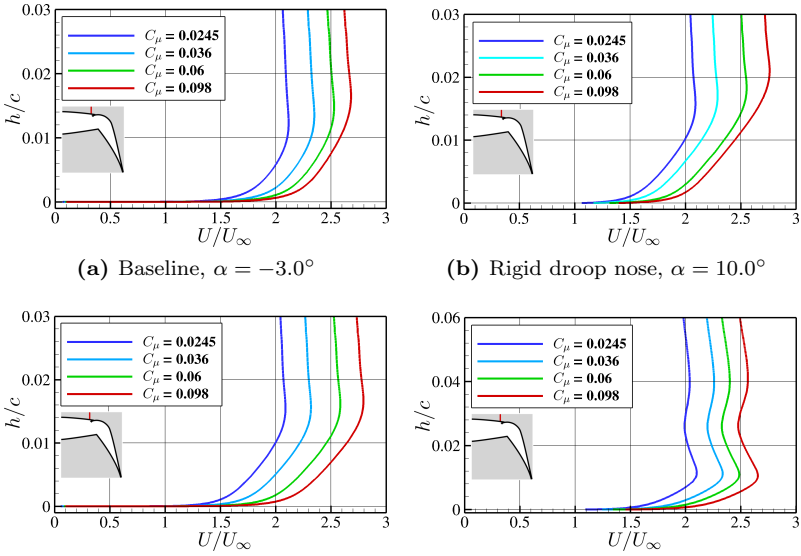

(a) Baseline, $\alpha = -3.0°$

(b) Rigid droop nose, $\alpha = 10.0°$

(c) Flexible droop nose, $\alpha = 10.0°$

(d) Slat nose, $\alpha = 10.0°$

Figure 3.9: Velocity profiles over the jet slot, at constant angles of attack, $Re = 12 \cdot 10^6$, $M = 0.15$ [15].

Another important outcome of the boundary-layer analysis is the boundary-layer behavior at stall conditions. Although the ranges of angle of attack plotted in figure 3.8 include post-stall conditions, the trends do not exhibit abrupt variations. This suggests that stall is driven by a gradual mechanism rather than a sudden flow detachment. Leading-edge flow separation was observed only with the baseline configuration at very high blowing momentum. Section 3.2.2 provides more detailed insight into these phenomena.

3.2.2 Maximum Lift Performance

This section focuses on the maximum lift performances of the four previously introduced configurations for different blowing rates. For the sake of completeness, results of no-blowing conditions are also included in the analysis; however, these values are considered less accurate than the blowing cases because of the shortcomings of the numerical approach employed here in simulations of largely separated flows. Without active flow control, the region over the 65°-deflected flap is dominated by unsteady vortical structures, which cannot be accurately predicted with a steady RANS simulation. These separated cases typically present the lift fluctuations mentioned in section 2.2.5 so the average lift coefficient is taken as a representative result.

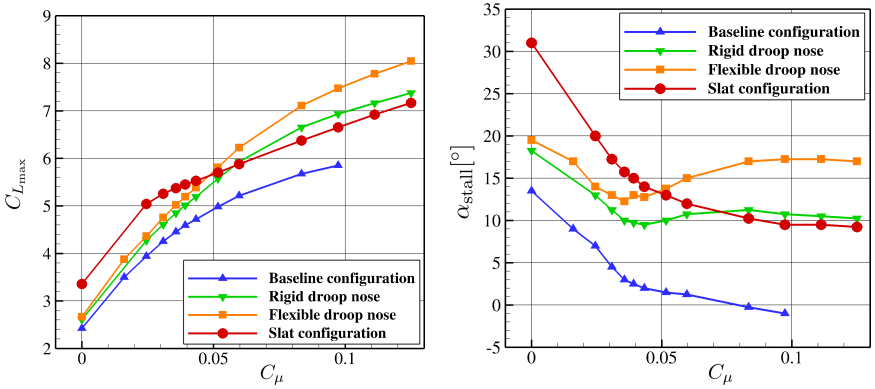

(a) Effect of C_μ on the maximum lift coefficient

(b) Effect of C_μ on the stall angle of attack

Figure 3.10: Response of the four airfoils to different momentum coefficients, $M = 0.15$, $Re = 12 \cdot 10^6$.

An increase of jet momentum enhances the circulation, which results in higher maximum lift, figure 3.10a. However, the blowing efficiency decreases at high C_μ. At low blowing rate the flow over the flap is partially separated and even a small increase of C_μ delays flow separation, resulting in a significant lift improvement. This condition is referred to as "boundary-layer control regime" and occurs until the separation location reaches the trailing edge, which approximately results in the lift value predicted by the potential theory for inviscid flow. The operation of the flap with higher levels of jet momentum is named

"supercirculation regime". The increase of lift is now achieved by a further deflection of the streamlines due to the jet effect downstream of the trailing edge. This explains the lower efficiency of this regime, as a larger increase of blowing power is needed in order to obtain the same lift improvement. The different mechanisms of the two regimes are observed also in the trends of maximum-lift angles shown in figure 3.10b. Within the boundary-layer control regimes the stall angle drops quickly with C_μ, whereas this trend is significantly reduced, or even inverted, in supercirculation regime. A more detailed discussion of the stalling behaviors is presented in the following paragraphs.

Optimal Blowing Rate

The minimum jet momentum that ensures fully attached flow, i.e. the border between boundary-layer control and supercirculation regime, corresponds to the optimal blowing rate, since it yields the highest lift gain without significant loss of efficiency. A lower blowing rate would provide more flow turning with a lower flap deflection, which would lead to attached flow. In the same way, a higher blowing rate could be employed with a higher flap angle [15]. This observation defines a natural relation between jet momentum and flap deflection angle. However, in the present chapter the flap angle is kept constant for the entire range of tested C_μ since the main purpose of the study is the analysis of the leading-edge device. Moreover, in order to investigate and understand the overall behavior of the high-lift configuration, it is worthwhile to consider the flow topologies generated by non-optimum blowing rates.

In figure 3.10a, the transition between boundary layer control and supercirculation regimes causes a gradual change of slope. This is due to the fact that the condition of fully attached flow is also affected by the angle of attack. Figure 3.11 shows the evolution of the flow field for angles of attack close to stall. For all the configurations the optimal momentum coefficient is around 0.036. A small trailing-edge separation occurs for the baseline and the two droop nose configurations until a few degrees before stall, whereas the flow is completely attached at the maximum-lift angle.

Stall Mechanisms

The flow behavior around the angle of maximum lift appears strongly dependent on the leading-edge configuration. This section describes the evolution of the flow at high angles of attack and explains the trends shown in figure 3.10. Figures 3.13 to 3.16 report flow fields that describe the stall mechanisms of the four configurations. The pictures are organized in tables where the three rows correspond to different jet momentum coefficients: 0.0245, 0.06 and 0.098. The central picture of every row displays the flow at maximum lift, whereas the first column shows the flow a few degrees before stall and the third column represents stalled conditions.

The first row of figures 3.13-3.16 illustrates the stall mechanism within the boundary-layer control regime (i.e. with separated flow due to low C_μ). At low angles of attack the jet separates from the flap surface and follows the same path as the outer flow. As the angle of attack increases, both the positive pressure gradient over the airfoil and the viscous losses at the leading-edge increase [16]. As briefly explained in section 2.1.1, the adverse pressure gradient causes a larger flow separation over the flap, whereas the viscous losses at the leading edge promote the reattachment of the jet to the flap surface through a gradual separation of the jet from the outer flow. The result of these effects is described in figure 3.12, which illustrates the behavior of the wall jet near the separation point for

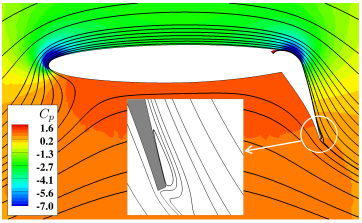

(a) $\alpha = 1.0°$, $C_L = 4.413$, baseline configuration

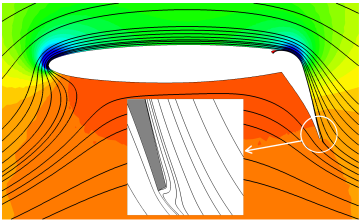

(b) $\alpha_{\text{stall}} = 3.0°$, $C_{L_{\max}} = 4.456$, baseline configuration

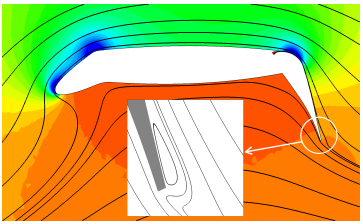

(c) $\alpha = 8°$, $C_L = 4.805$, rigid droop nose

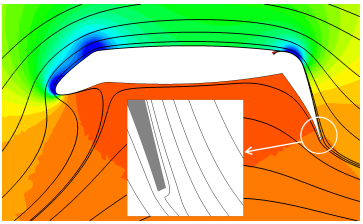

(d) $\alpha_{\text{stall}} = 10°$, $C_{L_{\max}} = 4.851$, rigid droop nose

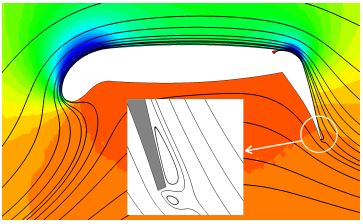

(e) $\alpha = 10.0°$, $C_L = 4.948$, flexible droop nose

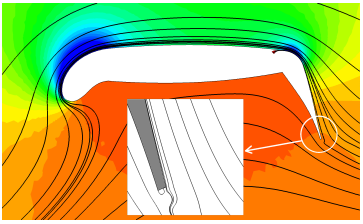

(f) $\alpha_{\text{stall}} = 12.25°$, $C_{L_{\max}} = 5.018$, flexible droop nose

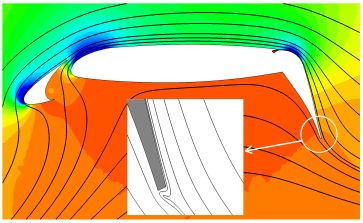

(g) $\alpha = 14.0°$, $C_L = 5.362$, slat configuration

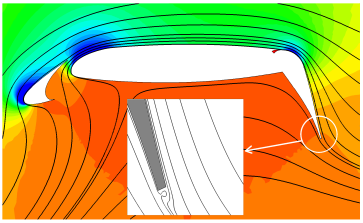

(h) $\alpha_{\text{stall}} = 16.0°$, $C_{L_{\max}} = 5.372$, slat configuration

Figure 3.11: Flow evolution near stall conditions at optimum blowing rate, $C_\mu = 0.0356$, $M = 0.15$, $Re = 12 \cdot 10^6$.

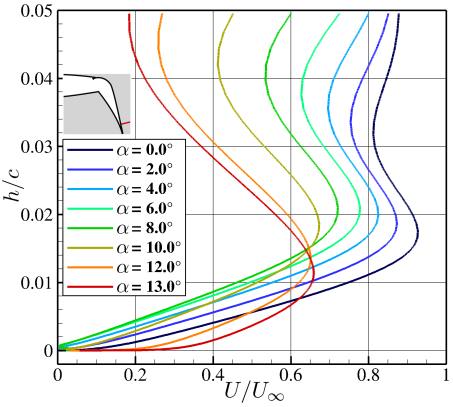

Figure 3.12: Velocity profiles at 5% chord ahead of the trailing edge for $C_\mu = 0.0356$, flexible droop nose, $M = 0.15$, $Re = 12 \cdot 10^6$.

$C_\mu = 0.0356$. Until $\alpha = 8.0°$ the positive pressure gradient enlarges the flow separation, whereas for higher angles of attack the flow is dominated by the viscous losses at the leading edge. As a consequence, the attachment between the jet and the outer flow becomes weaker, and the jet moves towards the flap surface. This phenomenon can cause the flap separation to disappear. In some cases a recirculation area occurs between the jet and the outer flow [15]. This happens typically for low blowing rates, as shown in figures 3.13b, 3.13c, 3.14b, 3.14c, 3.15c. Note that, the very high losses at the leading edge caused by high jet momentum for the baseline configuration can cause a similar flow topology (figure 3.13i). An increase in C_μ improves both the Coanda effect and the momentum transferred to the outer flow. As a result, the separation point is moved toward the trailing edge. This increases the lift coefficient but decreases the stall angle of attack, as the local adverse pressure gradient is more sensitive to α.

In supercirculation regime, the jet momentum is sufficient to completely avoid flow separation from the flap. Under this condition, the jet trajectory does not vary much, contrarily to the previous case. For the baseline configuration, a higher C_μ significantly increases the boundary layer momentum thickness over the slot, whereas for the slat configuration the momentum losses occur in the wake of the slat (figure 3.9d). As a result, for both the baseline and the slat geometries, high blowing rates lead to a reduction of the stall angle, as observed in figure 3.10b. With the droop-nose devices, on the other hand, the momentum losses in the outer flow caused by high C_μ are significantly lower. Therefore the outer flow will overcome stronger adverse pressure gradients, and stall is delayed. This behavior is sustained until $C_\mu \approx 0.08$.

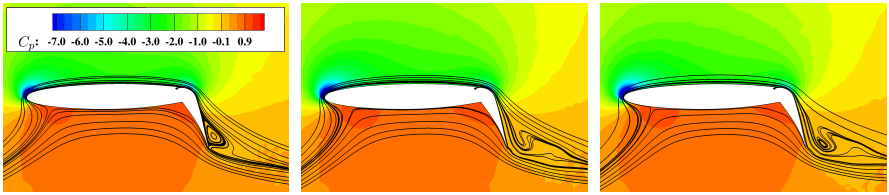

(a) $C_\mu = 0.0245$, $\alpha = 5.0°$, $C_L = 3.818$ **(b)** $C_\mu = 0.0245$, $\alpha = 7.0°$, $C_{L_{\max}} = 3.939$ **(c)** $C_\mu = 0.0245$, $\alpha = 8.0°$, $C_L = 3.857$

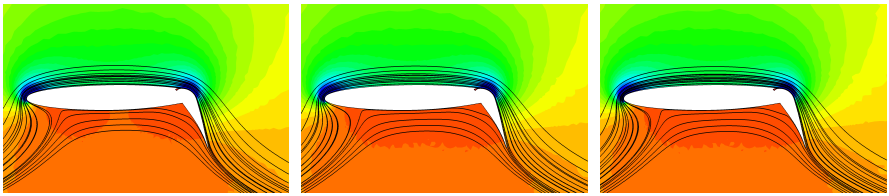

(d) $C_\mu = 0.06$, $\alpha = 0.0°$, $C_L = 5.195$ **(e)** $C_\mu = 0.06$, $\alpha = 1.25°$, $C_{L_{\max}} = 5.214$ **(f)** $C_\mu = 0.06$, $\alpha = 2.0°$, $C_L = 5.191$

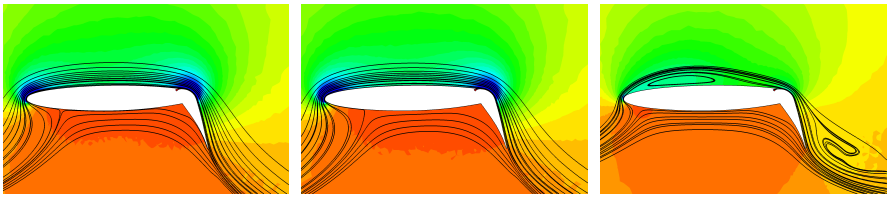

(g) $C_\mu = 0.098$, $\alpha = -3.0°$, $C_L = 5.703$ **(h)** $C_\mu = 0.098$, $\alpha = -1.0°$, $C_{L_{\max}} = 5.853$ **(i)** $C_\mu = 0.098$, $\alpha = 0.0°$, $C_L = 3.777$

Figure 3.13: Baseline configuration, C_p contour and streamlines, $M = 0.15$, $Re = 12 \cdot 10^6$.

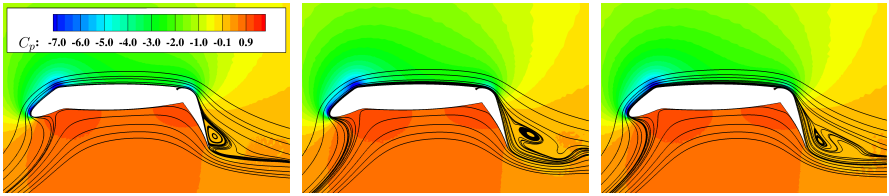

(a) $C_\mu = 0.0245$, $\alpha = 11.0°$, $C_L = 4.162$ **(b)** $C_\mu = 0.0245$, $\alpha = 13.0°$, $C_{L_{\max}} = 4.273$ **(c)** $C_\mu = 0.0245$, $\alpha = 15.0°$, $C_L = 4.213$

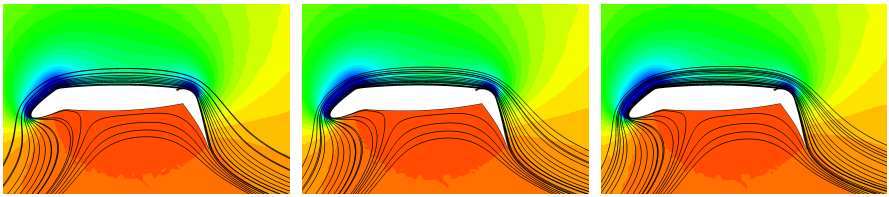

(d) $C_\mu = 0.06$, $\alpha = 9.0°$, $C_L = 5.898$ **(e)** $C_\mu = 0.06$, $\alpha = 10.75°$, $C_{L_{\max}} = 5.928$ **(f)** $C_\mu = 0.06$, $\alpha = 12.0°$, $C_L = 5.909$

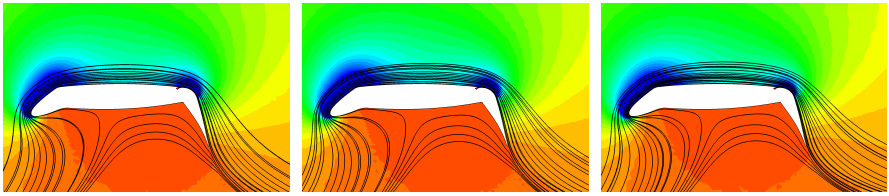

(g) $C_\mu = 0.098$, $\alpha = 9.0°$, $C_L = 6.861$ **(h)** $C_\mu = 0.098$, $\alpha = 10.75°$, $C_{L_{\max}} = 6.934$ **(i)** $C_\mu = 0.098$, $\alpha = 13.0°$, $C_L = 6.549$

Figure 3.14: Rigid droop nose configuration, C_p contour and streamlines, $M = 0.15$, $Re = 12 \cdot 10^6$.

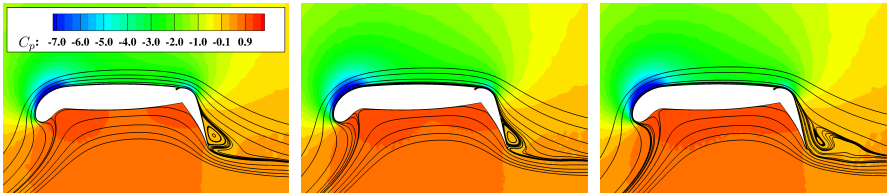

(a) $C_\mu = 0.0245$, $\alpha = 12.0°$, $C_L = 4.224$ **(b)** $C_\mu = 0.0245$, $\alpha = 14.0°$, $C_{L_{\max}} = 4.361$ **(c)** $C_\mu = 0.0245$, $\alpha = 15.0°$, $C_L = 4.357$

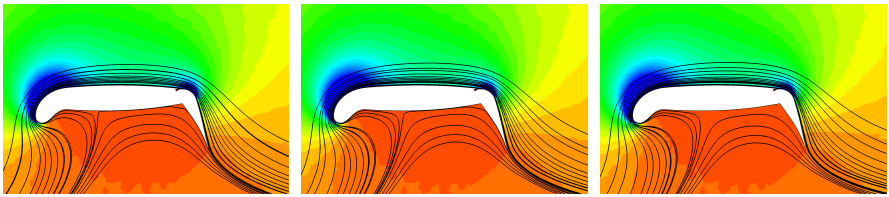

(d) $C_\mu = 0.06$, $\alpha = 13.0°$, $C_L = 6.192$ **(e)** $C_\mu = 0.06$, $\alpha = 15.0°$, $C_{L_{\max}} = 6.226$ **(f)** $C_\mu = 0.06$, $\alpha = 16.0°$, $C_L = 6.215$

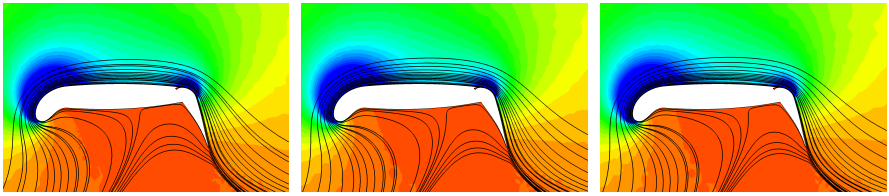

(g) $C_\mu = 0.098$, $\alpha = 15.0°$, $C_L = 7.393$ **(h)** $C_\mu = 0.098$, $\alpha = 17.0°$, $C_{L_{\max}} = 7.471$ **(i)** $C_\mu = 0.098$, $\alpha = 18.0°$, $C_L = 7.455$

Figure 3.15: Flexible droop nose configuration, C_p contour and streamlines, $M = 0.15$, $Re = 12 \cdot 10^6$.

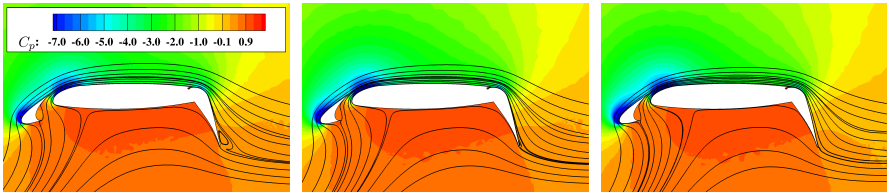

(a) $C_\mu = 0.0245$, $\alpha = 18.0°$, $C_L = 4.945$ **(b)** $C_\mu = 0.0245$, $\alpha = 20.0°$, $C_{L_{\max}} = 5.043$ **(c)** $C_\mu = 0.0245$, $\alpha = 22.0°$, $C_L = 4.998$

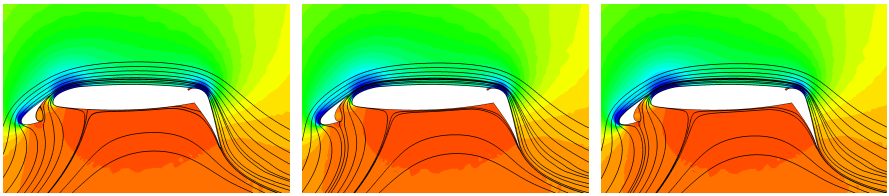

(d) $C_\mu = 0.06$, $\alpha = 10.0°$, $C_L = 5.860$ **(e)** $C_\mu = 0.06$, $\alpha = 12.0°$, $C_{L_{\max}} = 5.880$ **(f)** $C_\mu = 0.06$, $\alpha = 13.0°$, $C_L = 5.874$

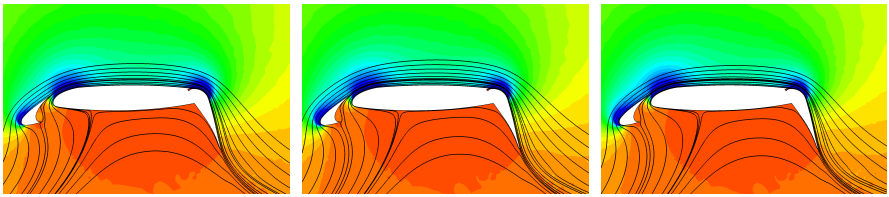

(g) $C_\mu = 0.098$, $\alpha = 7.0°$, $C_L = 6.589$ **(h)** $C_\mu = 0.098$, $\alpha = 9.5°$, $C_{L_{\max}} = 6.653$ **(i)** $C_\mu = 0.098$, $\alpha = 11.0°$, $C_L = 6.638$

Figure 3.16: Slat configuration, C_p contour and streamlines, $M = 0.15$, $Re = 12 \cdot 10^6$.

3.2.3 Overall Lift Gains

As mentioned in the introduction, a suitable parameter to evaluate the efficiency of the active high-lift system is the ratio between the increase of lift coefficient yielded by the active flow control and the momentum coefficient required to obtain that gain:

$$\text{Lift Gain Factor (LGF)} = \frac{C_{L_{\text{max, blowing}}} - C_{L_{\text{max, reference}}}}{C_\mu} \tag{3.2}$$

The reference $C_{L_{\max}}$ employed here is 1.87, which is the maximum lift coefficient obtained by the airfoil in cruise configuration (with flap and leading-edge device retracted). Figure 3.17 reports the variation of the lift gain factor in relation to the blowing rate, for the different leading-edge configurations. The slat configuration yields the highest benefit for C_μ lower than 0.05; whereas the flexible droop-nose is the most effective configuration for higher blowing. The slat curve shows a more rapid loss of efficiency with the blowing rate, compared to the other three configurations. This suggests that the slat setting employed here is not suited to the high circulation generated by strong Coanda jets. A new positioning of the slat would, in this case, significantly improve the performance at high jet momentum.

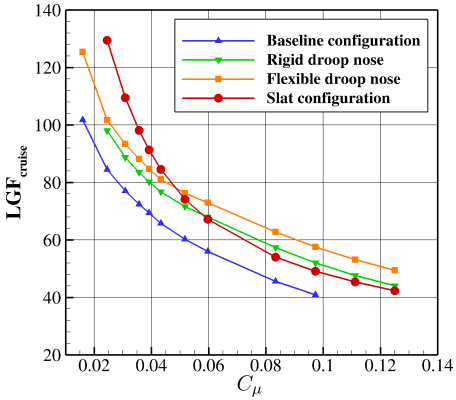

Figure 3.17: Effects of blowing rates on lift gain factor, $M = 0.15$, $Re = 12 \cdot 10^6$.

A further estimate of the gains yielded by the stall protection devices is obtained by examining the blowing rate required to generate a target maximum lift [15]. Using the present computational data-base for this estimate leads to approximate results in the following sense:

- The flap deflection angle is not varied. As a consequence, the potential of the blowing jet are fully exploited only around $C_\mu = 0.0356$, which is the optimal blowing rate for all investigated leading-edge configurations (section 3.2.2). Other blowing rates would require adjustments in the flap deflection angle.
- Only a discrete number of blowing rates has been tested. Therefore a linear interpolation was performed to obtain the result for a given target lift coefficient.

Table 3.4: Aerodynamic coefficients and blowing requirements at same maximum lift, $M = 0.15$, $Re = 12 \cdot 10^6$.

	C_μ	α_{stall}	$C_{L_{\max}}$	$C_{M_{\text{stall}}}$	$\text{LGF}_{5,\text{ cruise}}$
Baseline	0.0522	1.5°	5.0	-0.880	60.0
Rigid droop nose	0.0389	10.0°	5.0	-0.764	80.5
Flexible droop nose	0.0353	12.3°	5.0	-0.724	88.7
Slat configuration	0.0232	20.6°	5.0	-0.304	135.0

Even if not rigorously accurate, the present analysis points out the benefits of the different leading-edge devices expected in realistic STOL aircraft applications. A target maximum lift coefficient of $C_{L_{\max}} = 5.0$, yields the results summarized in table 3.4. All leading-edge devices reduce the required jet momentum coefficient by significant amounts. The slat configuration results in the lowest blowing requirements, followed by the flexible droop nose. The pitching moment around the reference point 25% chord is also given. Again, the slat configuration provides the best improvement, thanks to the high load on the slat and the extended chord.

In conclusion, the slat configuration turns out to be the most effective, with respect to lift and pitching moment performance. However, major issues may arise from the noise emissions generated by the high-velocity flow at the slat trailing-edge. The behavior of the slat wake facing the adverse pressure gradient over the Coanda flap should also be more thoroughly investigated. Ying reported in Ref. [211] the risk of sudden spreading of the slat wake when exposed to a strong adverse pressure gradient. For this purpose, experimental or numerical approaches able to accurately capture the dynamics of the free shear-layer and the flow curvature should be used.

4 Droop-Nose Performance on a 3D Aircraft Wing

The active high-lift configuration investigated in chapter 3 is here integrated into a high-wing transport aircraft model. The high circulation yielded by the Coanda flap generates three-dimensional flow mechanisms that limit the lift performance to values significantly lower than the two-dimensional design analyses [18]. This chapter presents a study of these dynamics for the baseline and the flexible droop-nose leading-edge configurations based on the results obtained by Thiemeier within the framework of his Master Thesis at Technische Universität Braunschweig [189].

4.1 Geometry and Grid

The aircraft geometry employed to assess the two-dimensional droop-nose design is the result of a preliminary overall aircraft design process performed with the software PrADO [57, 198]. The model is characterized by the tapered, twisted and swept wing illustrated in figure 4.1a. The connections between the movable surfaces and the wing are smoothed in order to facilitate the structured meshing process, as reported in detail by Thiemeier in Ref. [189]. A constant deflection angle of 65° is used for the flap, and 30° for the aileron, which is also equipped with the Coanda blowing device.

Similarly to the two-dimensional studies, the numerical mesh is realized by using the grid generator Pointwise Gridgen. Such tool allows an accurate point distribution also in regions of complex geometry thanks to a manual definition of the structured mesh topology. As shown in figures 4.1c and 4.1d, structured blocks are employed to discretize the volume from the surface of the model until a distance of about half of the wing-tip chord. The volume from the structured mesh to the outer boundaries is filled with tetrahedra but divided into four sub-volumes in order to adapt the grid density to the expected local flow topology, as displayed in figure 4.1b. The resulting grid is made of about 50 million points, and the dimensions of the external shell are about 400 times the reference cord length, in vertical and streamwise directions, and 130 times in spanwise direction.

4.2 Results

The freestream flow conditions used for the simulations presented in this section represent a typical landing phase: $Re = 12 \cdot 10^6$ and $M = 0.15$. Under these conditions, according to two-dimensional computations, a jet momentum coefficient of about $C_\mu = 0.035$ is required to achieve fully attached flow over the flap, which is deflected by 65°. This value of jet momentum coefficient is applied over the entire wing span, although the aileron deflection

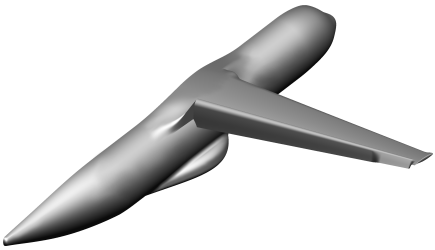

(a) Wing-body aircraft model

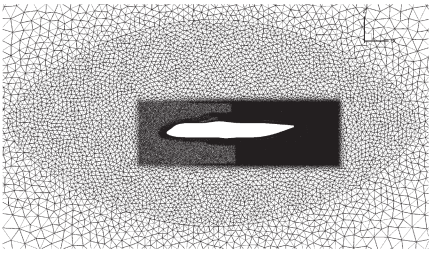

(b) Overview of the grid inner subvolumes

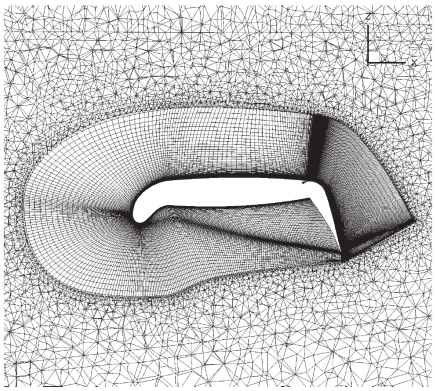

(c) Grid of the wing section

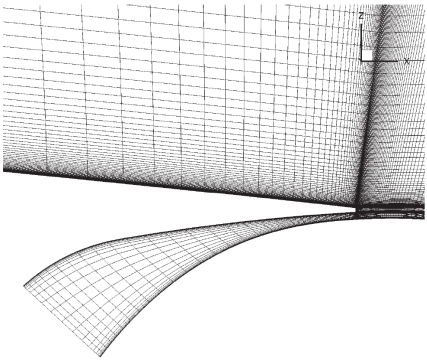

(d) Close-up of the blowing slot grid

Figure 4.1: 3D model geometry and numerical mesh.

angle is 45° and could thus be operated with a lower blowing rate. This assures attached flow also during the movements of the aileron and during all flight conditions. Details on longitudinal stability of the present configuration are discussed by Keller in [75, 76].

Figure 4.2 reports the lift curves of the baseline and the flexible droop-nose configurations over the angle of attack [189]. As expected from the previous 2D studies, the droop-nose device yields a higher stall angle and a significant increase of maximum lift. However, the loss of lift appears more sudden than for the airfoil study, where the slope of the lift curves decreases gradually. This suggests different stall mechanisms for the aircraft model. The analysis that follows begins with a comparison between the lift performance of the two-dimensional airfoil and a representative wing section of the three-dimensional aircraft model. Next, the three-dimensional stall mechanisms are discussed, explaining the differences with respect to the 2D airfoil flow.

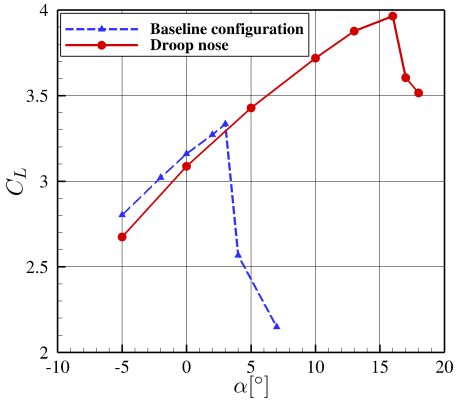

Figure 4.2: Lift curves of the 3D model, droop nose and baseline configuration, $C_\mu = 0.035$, $Re = 12 \cdot 10^6$ and $M = 0.15$.

4.2.1 Performance Comparison between 2D and 3D Results

An important objective of the present three-dimensional study is the investigation of the differences between the two-dimensional flow fields resulting from the airfoil analyses and the three-dimensional mechanisms of the flow around the aircraft model. The comparison of the lift performances is based on the lift generated by the wing section $\eta = 2y/b = 0.6$, where b represents the wing span, and considers the local effective angle of attack. The effective angle of attack, α_e, differs from the global one by the local wing twist and the downwash, which was estimated according to the lifting-line theory of Prandtl. This estimation is therefore based on the assumption of potential flow, which is not valid everywhere for the present case. The accuracy of the induced angle of attack obtained with this approach is affected by the high flow curvature caused by the active flap, the recirculation areas downstream of the flap, as well as the actual lift distribution along the wing span, as explained in Ref. [189]. However, as the induced angle of attack is relatively small at a wing aspect ratio around 10, these data can be used as basis for a comparison between the two geometries, and as starting point for the analysis of the three-dimensional flow fields [18].

Figure 4.3 illustrates the lift performance comparison for $C_\mu = 0.035$. In comparison with the isolated airfoil, the wing section generates a slightly lower lift coefficient already within the quasi-linear range of the lift curves. The difference is about 0.2 for both leading-edge configurations. However, the slopes of the lift curves appear very similar, which suggests that the generation of lift before stall-onset is not significantly affected by three-dimensional phenomena. Once the stall mechanism is triggered, on the other hand, the wing sections seem to behave very differently from the isolated airfoils. Three dimensional flow mechanisms cause a sudden drop of lift much earlier than the two-dimensional flow. Note that the last two points of the wing section curve for the baseline configuration exhibit major

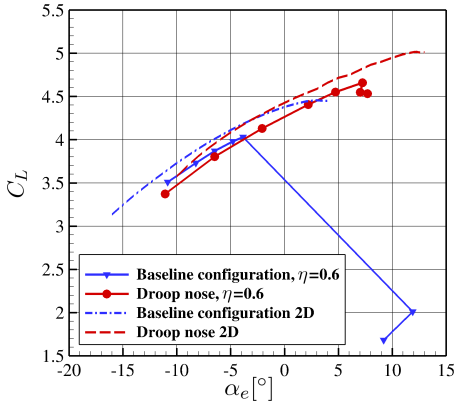

Figure 4.3: Lift curve comparison between 2D simulations and a 3D wing section, $\eta = 0.6$, droop nose and baseline configuration, $C_\mu = 0.035$, $Re = 12 \cdot 10^6$ and $M = 0.15$.

inaccuracy because of the use of the lifting-line method beyond the limits of applicability, as the flow in these cases is highly separated. In the following sections the stall mechanisms of the baseline and the droop-nose wing configurations are investigated in more detail and the reasons of the disagreement with the two-dimensional computations are discussed.

4.2.2 Stall Mechanisms

Baseline Wing Configuration

The investigation of the flow mechanisms can begin by observing the evolution of the non-dimensional circulation distribution in spanwise direction, $\gamma = \Gamma/(b \cdot |U_\infty|)$, for different angles of attack. The circulation appears to gradually increase over the entire wing until the angle of maximum lift. One degree after stall a large deficit of circulation takes place around $\eta = 0.7$ and propagates towards the wing root and tip, if the angle is further increased. The lower deflection of the aileron, however, enables the corresponding portion of the wing to produce reasonable lift even 4° after stall. The wall streamlines and the friction coefficient contours shown in figures 4.6 suggest that the stall mechanism for the baseline configuration is triggered by a leading-edge separation. This can be caused by the high circulation generated by the Coanda flap, which creates a strong suction peak at the leading edge. However, leading-edge separation is observed in two-dimensional computations only for jet momentum coefficients higher than 0.08. A comparison between the boundary layer profiles of 2D and 3D flows downstream of the nose is reported in figure 4.5. The boundary layer in the separation area over the three-dimensional wing appears thicker and more sensitive to angle of attack variations than the one over the isolated airfoil, at the same C_μ and α_e. This different behavior is likely caused by boundary-layer cross flow that occurs at the leading-edge stagnation point and increases with the angle of attack. This effect would also explain the difference in stall angle between the two- and three-dimensional baseline simulations

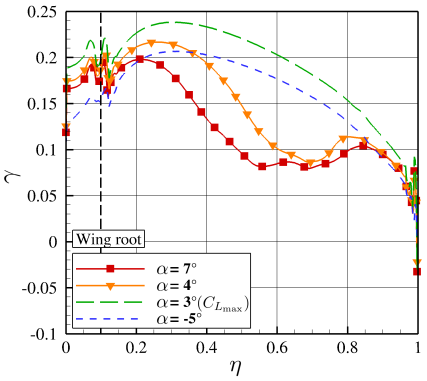

Figure 4.4: Spanwise circulation distribution, baseline configuration, $C_\mu = 0.035$.

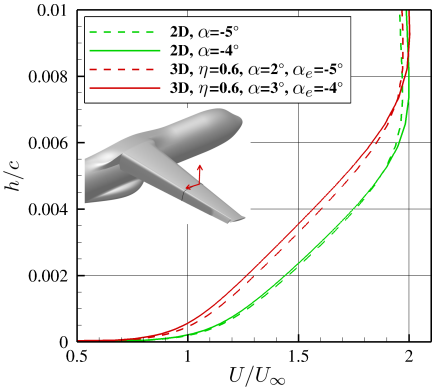

Figure 4.5: Velocity profiles variation with α at 20% chord, 2D and 3D at $\eta = 0.6$, $C_\mu = 0.035$.

mentioned in the previous section. Another possible reason for this early separation might be insufficient grid resolution in the leading-edge area, since no three-dimensional grid-convergence study was carried out.

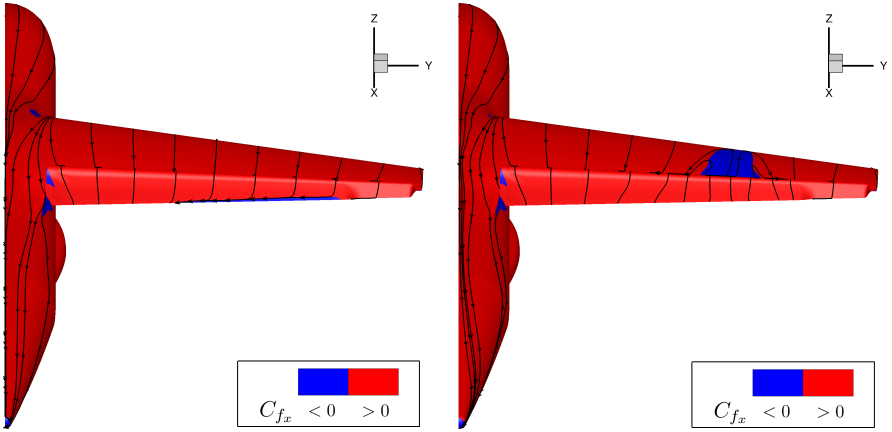

(a) $\alpha = 3°$ $(C_{L_{\max}})$ **(b)** $\alpha = 4°$

Figure 4.6: Surface streamlines and longitudinal friction coefficient close to stall condition for the baseline configuration.

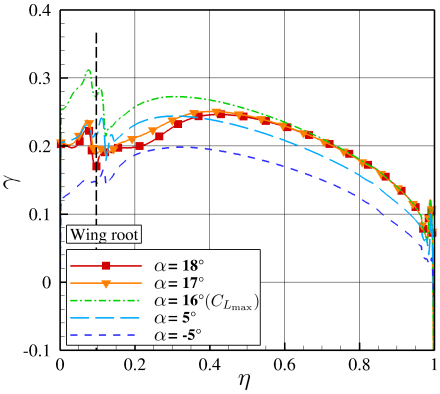

Figure 4.7: Spanwise circulation distribution, droop nose, $C_\mu = 0.035$.

Droop-Nose Wing Configuration

The two-dimensional studies discussed in chapter 3 proved that the suction peak at the leading edge is significantly reduced by the droop nose. This prevents leading-edge separation even at high jet momentum values and 2D stall is caused by a gradual separation between the Coanda jet and the outer flow. The stall mechanism of the 3D wing model equipped with the droop-nose device is therefore expected to be different from the baseline leading-edge configuration described in the previous section.

Figure 4.7 displays the variation of circulation distribution with the angle of attack. The distribution remains similar to the baseline configuration until the angle of maximum lift; whereas for higher angles of attack it appears substantially different. The reduction of circulation at high angles takes place in the proximity of the wing root, while the outer half of the wing maintains attached flow. This behavior can be explained by observing the surface streamlines and pressure coefficient distributions in figure 4.8. The trailing-edge flow separation occurring in the outer half of the flap area does not vary significantly during stall, which suggests that such separation does not play an important role in the lift-drop mechanism. The flow features over the wing root, on the other hand, change rapidly. The surface streamlines show a strong cross flow that directs near-wall fluid from the fuselage towards the wing flap, over the suction side of the wing. The cross flow is induced by the low pressure that exists over the wing and is enhanced by the angle of attack. The thick boundary layer developed over the fuselage reaches the root of the Coanda flap just at the angle of maximum lift and affects its behavior for higher angles of attack. Figure 4.9 displays the flow field at $\eta = 0.2$ at maximum lift and after stall. Until the condition of maximum lift the flow over the flap remains fully attached and the jet provides great flow turning. One degree after stall, however, the fuselage boundary layer reaches the blowing slot causing the Coanda jet to separate from the outer flow. At this point, a large recirculation region appears downstream of the flap, similarly to what observed for the isolated airfoil during the two-dimensional study, and the circulation is drastically reduced, until $\eta = 0.3$.

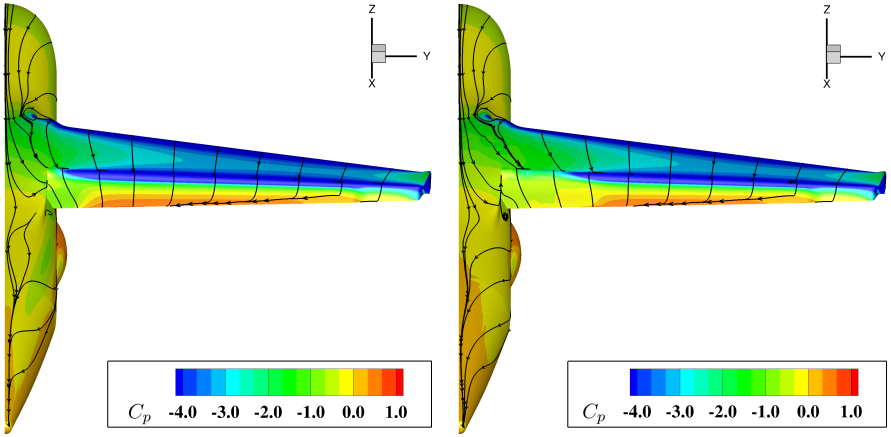

(a) $\alpha = 16°$ $(C_{L_{\max}})$ **(b)** $\alpha = 17°$

Figure 4.8: Surface streamlines and C_p distribution close to stall condition for the droop nose configuration.

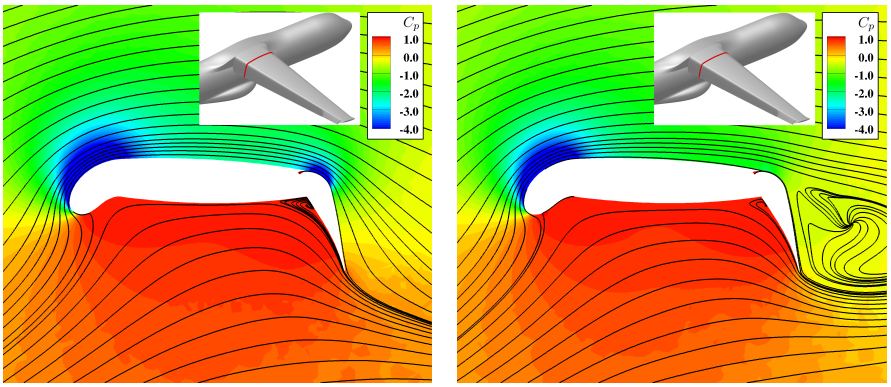

(a) Streamlines and C_p distribution, $\eta = 0.2$, $\alpha = 16°$ $(C_{L_{\max}})$

(b) Streamlines and C_p distribution, $\eta = 0.2$, $\alpha = 17°$

Figure 4.9: Flow field around the wing at $\eta = 0.2$ close to stall condition for the droop nose configuration.

Other examples in which boundary layer cross flow over the wing root degrades so drastically the high-lift system performance are not known to the author. The main cause of this non-conventional behavior is the high level of circulation yielded by the active flap in combination with the droop nose. Further investigations should begin with the validation of these numerical results by means of dedicated numerical simulations (e.g. simulations with a higher grid density in the wing-root area and possibly with a turbulence modeling approach suited for separated flow) and experimental data, in order to highlight possible inaccuracies in the phenomena presented here. Such analyses would also provide a richer description of the flow physics. Of particular interest are the interactions of the near-wall flow with the horse-shoe vortex generated at the leading edge and the dependency of the flow topology on the wing-root geometry. A more thorough understanding of these mechanisms would then allow finding a viable solution to improve the overall performance of the active high-lift configuration under operative conditions, thus approaching the two-dimensional predictions. One possibility to reduce the loss of maximum lift could be the adoption of fences to straighten the flow over the wing and limit the interaction between the fuselage boundary layer and the Coanda flap. Vortex generators could also be used similarly to a slat horn to induce a velocity component towards the center line of the aircraft in the near-wall fluid over the wing root.

5 Synergies of Suction and Blowing for Flow Control

A viable solution to generate the compressed air needed by the active Coanda flap system is using dedicated electric compressors. One design currently developed within the framework of the research center SFB 880 is based on the integration of compact compressors into the wing, behind the rear spar. This set-up can exploit the compressor intakes, located on the wing surface, to improve the boundary layer behavior around the airfoil [17]. In this context, this chapter focuses on the two-dimensional design of the air intake of a hypothetical compact compressor. The design drivers are the airfoil lift performances and the total pressure recovery inside the suction duct. Different suction-slot geometries and locations are tested on the flexible droop-nose configuration described in section 3 in order to investigate the aerodynamic sensitivities of the main geometrical parameters. The final lift gain is then evaluated testing one representative suction configuration for different blowing momentum coefficients.

5.1 Design of the Suction Duct

The design of the suction duct is carried out by investigating the aerodynamic sensitivities of the internal shape and location of the duct. The suction device is added to the configuration with Coanda-flap and droop-nose that results from the droop-nose design work presented in section 3.1. Different intake geometries are therefore tested and the performances are evaluated in terms of maximum lift and total pressure recovery along the duct. The momentum coefficient of the Coanda jet is kept constant at $C_\mu = 0.0356$, which represents the optimal blowing rate for a flap deflection angle of $\delta = 65°$ (see section 3.2.2). The mass flow through the suction slot is determined by the mass flow of the Coanda jet, considering that the jet is generated by compressing the air at the end of the suction duct. The width of the final section of the duct is estimated in order to achieve $M_{\text{inlet}} = 0.1$, which is considered a suitable value for a compressor inlet. The resulting duct width at the end section is 0.6% of the airfoil chord, for a suction slot located at 61% of the chord length. The freestream conditions are $Re = 12 \cdot 10^6$ and $M = 0.15$.

The analysis focuses on the geometrical parameters illustrated in figure 5.1. The aerodynamic sensitivities of the internal shape of the duct, defined by the parameters β and γ, are discussed in section 5.1.1; whereas the effects of the suction slot location, identified by x, are described in section 5.1.2. Finally, in order to evaluate the overall performance and identify the most effective configuration, the two performance indicators, maximum lift coefficient and total pressure recovery along the duct, are combined into one design objective: a balanced lift coefficient, as presented in section 5.1.3.

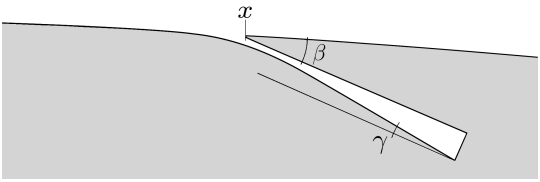

Figure 5.1: Geometrical parameters that define the suction slot shape and location.

5.1.1 Internal Shape Analysis

The sensitivity study of the internal shape of the suction duct is performed by varying the local duct angle β and the diffusion angle γ while the duct location is fixed at $x = 61\%$ of the airfoil chord. In this location, the slot would be positioned upstream of the front edge of a hypothetical spoiler but downstream of the wingbox. Positioning the suction slot in the front of the wingbox would involve the duct passing through the supporting structure of the wing. The minimum duct angle with respect to the local airfoil surface is limited to $\beta = 10°$. Lower angles could slightly enhance the total pressure recovery, but a thinner lip would involve larger deformation when exposed to the pressure difference between the internal and the external flow.

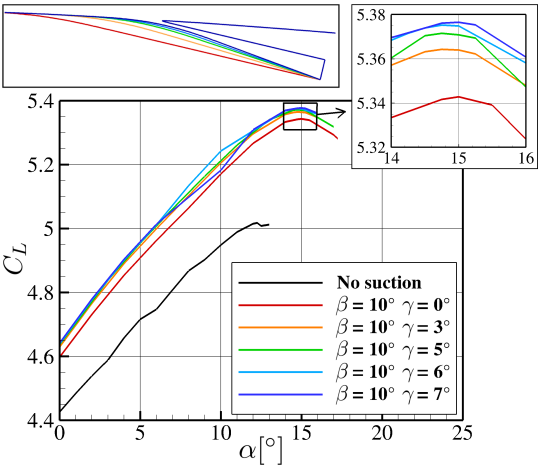

Figure 5.2: Effect of diffuser angle on maximum lift performance, for $\beta = 10°$, $Re = 12 \cdot 10^6$, $M = 0.15$.

According to the lift curves reported in figure 5.2, the suction device at 61% of the airfoil chord enhances the maximum lift coefficient by up to 7% and delays stall by 3°, with respect to the configuration without wall suction. The largest benefit is obtained with the highest diffusion angle, $\gamma = 7°$. Reducing the duct diffusion from 7° to 0° degrades the

maximum lift by about 0.6%, whereas the stall angle remains approximately constant. For a duct angle $\beta = 20°$, the effect of the diffusion angle variation on the lift performance is about 0.3%. The internal duct geometry has also a significant influence on the total pressure recovery. For this reason, the connection between the lower side of the channel and the original airfoil contour is designed to avoid flow separation. The effects of duct and diffusion angles on the pressure recovery are reported in table 5.1 and discussed in section 5.1.3.

5.1.2 Location Analysis

Having assessed the potential of the wall suction at 61% chord length, the suction slot with $\beta = 10°$ and $\gamma = 0°$ is tested in three other locations: 30% chord, 85% chord and 75% chord on the pressure side (figure 5.3). The suction slot locations are selected based on their expected effects on the flow physics, as discussed by the author in Ref. [17]. At 30% chord the flow experiences the strong adverse pressure gradient that occurs after the suction peak at the leading edge. This increases the boundary layer thickness along the suction side of the airfoil, thereby affecting the efficiency of the Coanda flap. For this reason, manipulating the boundary layer in this area may significantly reduce the jet momentum requirements. A similar effect is expected by the suction slot at 61% chord, which will enhance the boundary-layer momentum just upstream of the blowing slot. At 85% chord the suction slot is located on the flap surface. In this location it may be possible to avoid the flow separation that occurs with low jet momentum coefficients, exploiting a mechanism similar to the one described by Chen in Ref. [23]. Finally, a suction slot on the pressure side of the airfoil, at 75% of the chord length, is tested in order to reduce the recirculation area occurring at the flap hinge and to benefit from the high total pressure present in this area.

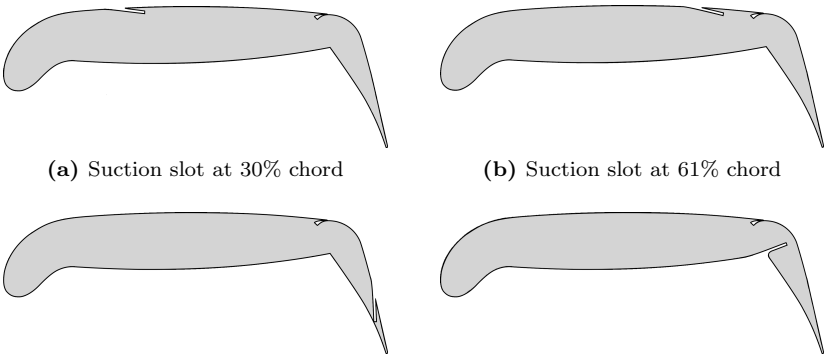

(a) Suction slot at 30% chord

(b) Suction slot at 61% chord

(c) Suction slot at 85% chord

(d) Suction slot at 75% chord on the pressure side

Figure 5.3: Tested suction locations.

The lift curves reported in figure 5.4 show that the location of the suction slot has a larger effect on the lift performance than the internal duct geometry. Positioning the suction slot upstream of the blowing device turns out to be the best choice. In particular, the 30% chord suction yields the highest performance, enhancing lift by 12% and delaying stall by 6°, with respect to the case without suction. A suction slot on the flap surface, on the other hand, appears to have a detrimental effect on lift. In this case the maximum lift coefficient is reduced by 0.7% and the corresponding angle by 1°. Finally, the variation of lift yielded by suction at the flap hinge is negligible. These results are explained in the following sections by investigating the flow mechanisms generated by wall suction at the different locations.

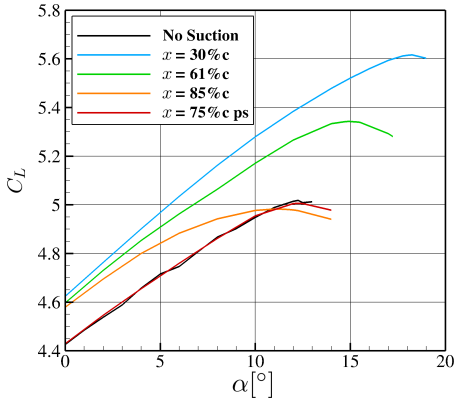

Figure 5.4: Effect of suction location on the lift curve, $C_\mu = 0.0356$, $Re = 12 \cdot 10^6$, $M = 0.15$.

Suction Upstream of the Blowing Slot

Both the suction slots located at 30% and at 61% chord reduce the boundary-layer thickness upstream of the blowing slot. The momentum enhancement of the near-wall fluid in this area brings large benefit to the operation of the Coanda flap, as discussed in section 3.2. The velocity profiles just upstream of the blowing slot, reported in figure 5.5, show that the flow momentum in the case of suction at 30% chord is higher than the other cases. In particular, the non-dimensional momentum thickness of the boundary layer above the blowing slot is $\delta_2/c = 7.8 \cdot 10^{-4}$ for suction at 30% chord, $\delta_2/c = 9.8 \cdot 10^{-4}$ for suction at 61% chord, and $\delta_2/c = 1.3 \cdot 10^{-3}$ for the configuration without suction. The overall effect on the airfoil flow is an increase of circulation, which leads to pressure coefficient distributions similar to an augmentation of jet momentum, as shown in figure 5.6.

Suction on the Flap Surface

The comparison shown in figure 5.4 is obtained with a jet momentum coefficient that assures fully attached flow over the Coanda flap, $C_\mu = 0.0356$. Under these conditions, a slot positioned on the flap surface removes part of the Coanda jet, thereby reducing the

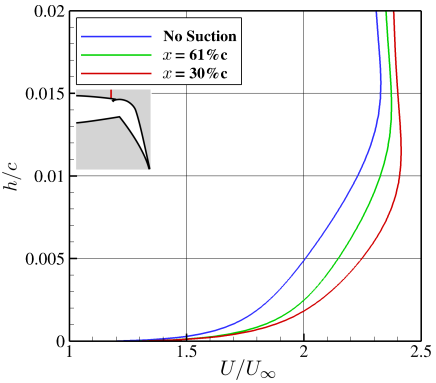

Figure 5.5: Velocity profiles of the boundary layer upstream of the blowing slot, $C_\mu = 0.0356$, $\alpha = 10°$, $Re = 12 \cdot 10^6$, $M = 0.15$.

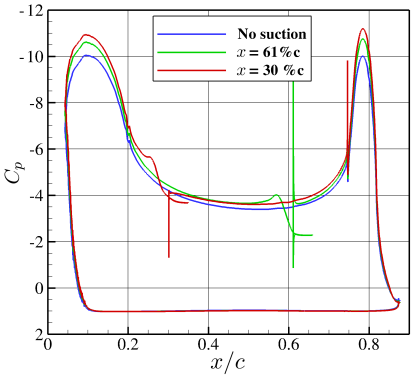

Figure 5.6: C_p distributions for configurations with suction upstream of the blowing slot, $C_\mu = 0.0356$, $\alpha = 10°$, $Re = 12 \cdot 10^6$, $M = 0.15$.

momentum of the flow over the flap [17]. For this reason, it is worth testing wall suction in this location for a lower jet momentum, such that the flow separates from the flap upstream of the suction slot. Figure 5.7a displays the topology of the flow field for $C_\mu = 0.016$ at an angle of attack within the linear range of the lift curve. The large recirculation area occurring downstream of the flap seems to be not significantly affected by wall suction. The authority of the suction device could be enhanced by moving the suction slot towards the separation point. However, the topology of the flow at higher angles of attack changes drastically, as shown in figure 5.7b. At the condition of maximum lift, there occurs no longer a flow separation from the flap surface, as the separation takes place between the outer flow and jet (as explained in section 2.1.1). This makes wall suction again unable to effectively interact with the vortical structures.

Suction at the Flap Hinge

The recirculation area at the flap-hinge corner is characterized by a higher total pressure with respect to the airfoil suction side. The advantage of a suction slot in this location is therefore mostly rooted in a high total pressure at the end of the suction duct. Figure 5.8 shows the effects of suction to the local flow topology. The recirculation structure is no longer present, but this seems to have only minor effects on the lift performance, as shown by the lift curve in figure 5.4. The benefit of the high total pressure inside the suction duct is discussed in the next section, where an approach to translate the total pressure recovery into lift is proposed, thus allowing a comparison among the different configurations based on the overall performance.

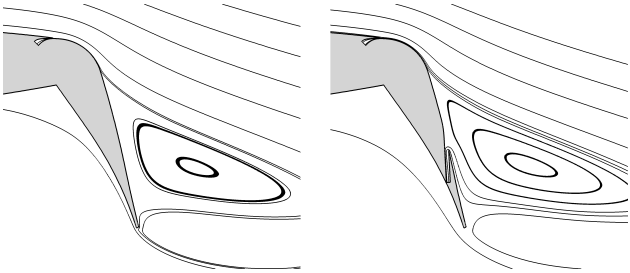

(a) $\alpha = 10°$ without suction (left) and with suction (right)

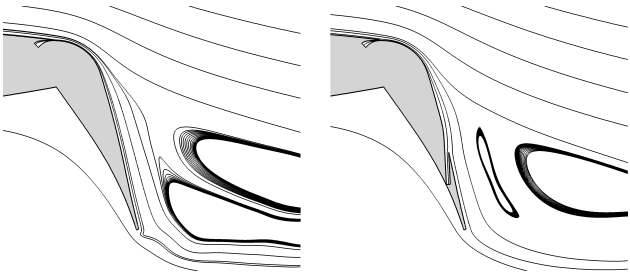

(b) Maximum lift condition without suction at $\alpha_{\text{stall}} = 17°$ (left) and with suction at $\alpha_{\text{stall}} = 15.25°$ (right)

Figure 5.7: Effect of wall suction at 85% chord on the flow over the flap, $C_\mu = 0.016$, $Re = 12 \cdot 10^6$, $M = 0.15$.

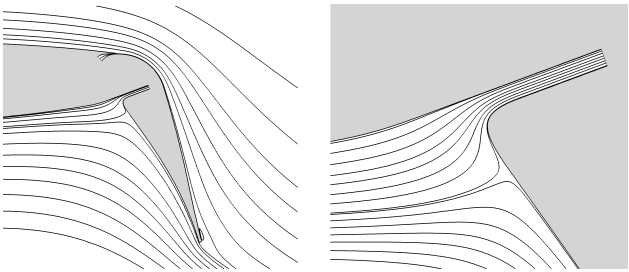

Figure 5.8: Wall suction at the flap hinge, $C_\mu = 0.0356$, $\alpha = 10°$, $Re = 12 \cdot 10^6$, $M = 0.15$.

5.1.3 Overall Suction Performance: Lift Balance

The objectives of the wall suction device are 1) to provide air at high total pressure to the compact compressors, and 2) to improve the maximum lift generated by the airfoil. However, these two objectives follow opposite trends when the geometrical parameters are varied: a narrow suction slot increases lift but also induces high viscous losses to the internal flow, thus reducing the total pressure recovery. For this reason, a combined quantity is needed to evaluate and compare the overall performance of the tested geometries. The approach proposed by the author in Ref. [17] is based on the following considerations:

- With a high inlet total pressure, the compressor needs less power to provide the outlet total pressure required by the Coanda jet. Similarly, for a given compression ratio the compressor provides higher outlet total pressure with respect to a case with low inlet total pressure.
- High total pressure inside the jet plenum (compressor outlet) generates a jet with high momentum.
- The lift coefficient can be considered directly proportional to the jet momentum coefficient, for small variations of C_μ.

It can be deduced that a high total pressure recovery along the suction duct leads to a high lift coefficient, for a given compression ratio. Thanks to this relation, it is possible to balance the lift coefficient with the total pressure obtained at the end of the suction slot. The procedure used to obtain the balanced lift coefficient is reported in the flowchart of figure 5.9. As first step, a new total pressure inside the jet plenum (i.e. the outlet of a hypothetical compact compressor) is calculated by multiplying the total pressure at the end of the suction duct by a reference compression ratio. A new jet momentum coefficient is then obtained from the plenum total pressure. Next, the new jet momentum coefficient is compared to the initial one, employed to compute the flow solution. The difference between the two jet momentum coefficients is used to estimate a variation of lift coefficient based on a database containing C_μ and C_L values. Thanks to the lift coefficient variation, it is finally possible to compute the balanced lift coefficient.

Such procedure does not consider second order effects of a jet momentum variation, e.g. an augmentation of circulation due to a higher jet momentum would further increase the total pressure inside the suction duct. A better estimation could be obtained by performing more than a single iteration; however, the effect would be rather small and it would simply increase the differences among the balanced performances resulting from the first iteration. In order to compute the balanced lift coefficient for the present configurations, a compression ratio was obtained from the total pressure inside the jet plenum and the one at the end of the suction slot, using as reference the geometry with $\beta = 10°$, $\gamma = 0°$, and $x = 61\%$ chord. For this reason, the balanced lift coefficient of this geometry does not differ from the initial one.

Figure 5.10 and table 5.1 report the balanced lift coefficients resulting from the different internal duct geometries introduced in section 5.1.1. Increasing the duct diffusion angle, γ, causes a reduction of the suction slot opening, which accelerates the flow entering the duct. This has a double effect, as it enhances the lift generated by the airfoil but also increases the viscous losses inside the suction duct. The balanced lift coefficient proves that this second effect overcomes the lift benefit for $\gamma > 3°$, where the curves exhibit a substantial decrease of balanced lift. Such drop of the overall performance is caused by the appearance of a small separation bubble on the lower side of the suction slot lip, which causes a significant loss of total pressure inside the duct. As the figure shows, the most effective configuration,

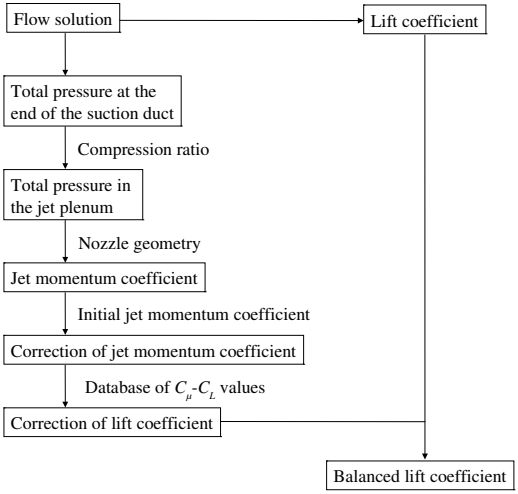

Figure 5.9: Procedure to compute the balanced lift coefficient.

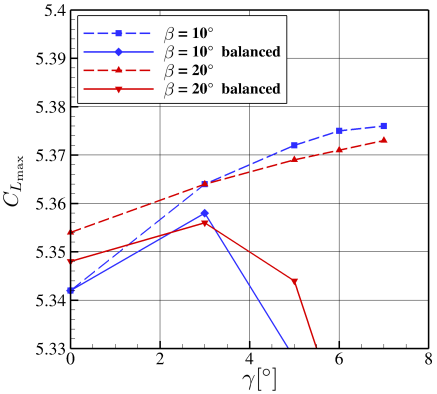

Figure 5.10: Balanced performances for different internal duct shapes.

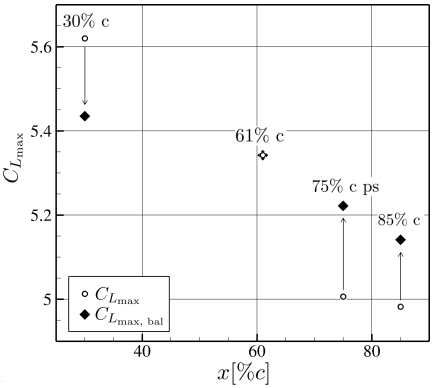

Figure 5.11: Balanced performances for the tested suction slot locations.

Table 5.1: Lift coefficient balance for the internal duct geometries, $x = 61\%$ chord.

Configuration	$C_{L_{\max}}$	p_{ti}/p_∞	$C_{\mu_{\text{bal}}}$	$C_{L_{\max,\ \text{bal}}}$
$\beta = 10°$, $\gamma = 0°$	5.342	0.9664	0.0356	5.342
$\beta = 10°$, $\gamma = 3°$	5.364	0.9652	0.0355	5.358
$\beta = 10°$, $\gamma = 5°$	5.372	0.9578	0.0349	5.328
$\beta = 10°$, $\gamma = 6°$	5.375	0.9348	0.0328	5.214
$\beta = 10°$, $\gamma = 7°$	5.376	0.8548	0.0257	4.735
$\beta = 20°$, $\gamma = 0°$	5.354	0.9652	0.0355	5.348
$\beta = 20°$, $\gamma = 3°$	5.364	0.9649	0.0355	5.356
$\beta = 20°$, $\gamma = 5°$	5.369	0.9615	0.0351	5.344
$\beta = 20°$, $\gamma = 6°$	5.371	0.9556	0.0346	5.316
$\beta = 20°$, $\gamma = 7°$	5.373	0.9371	0.0330	5.224

Table 5.2: Lift coefficient balance for the suction locations, with $\beta = 10°$ and $\gamma = 0°$.

Configuration	$C_{L_{\max}}$	p_{ti}/p_∞	$C_{\mu_{\text{bal}}}$	$C_{L_{\max,\ \text{bal}}}$
$x = 30\%$ c	5.620	0.9302	0.0324	5.435
$x = 61\%$ c	5.342	0.9664	0.0356	5.342
$x = 85\%$ c	4.982	1.0016	0.0387	5.141
$x = 75\%$ c ps	5.006	1.0154	0.0397	5.222

which yields the highest balanced lift coefficient, is obtained with $\beta = 10°$ and $\gamma = 3°$, for the $x = 61\%$ chord case.

The balanced lift coefficient was also computed with wall suction applied in different locations. The effects of the total pressure recovery along the suction duct on the maximum lift coefficients are shown in figure 5.11 and reported in table 5.2. The highest total pressure values are achieved at the end of the ducts located at 75% chord on the pressure side (ps) and on the flap upper surface (85% chord). However, even translating such high total pressure values into an increase of lift, the overall performance remains lower than the cases where wall suction is applied upstream of the blowing slot. In particular, the most effective suction location is 30% of the chord length, although the total pressure recovery turns out to be lower than for the other cases.

5.2 Aerodynamic Performance

This section focuses on the aerodynamic response of a configuration with wall suction to different jet momentum coefficients. The behavior of the airfoil equipped with the suction slot $\beta = 10°$ and $\gamma = 0°$ located at $x = 61\%$ chord is compared with results obtained without suction. The effects of the suction device are also investigated on the baseline leading-edge configuration. The results are plotted in figure 5.12, where the improvements yielded by wall suction on maximum lift coefficient and stall angle can be observed over the

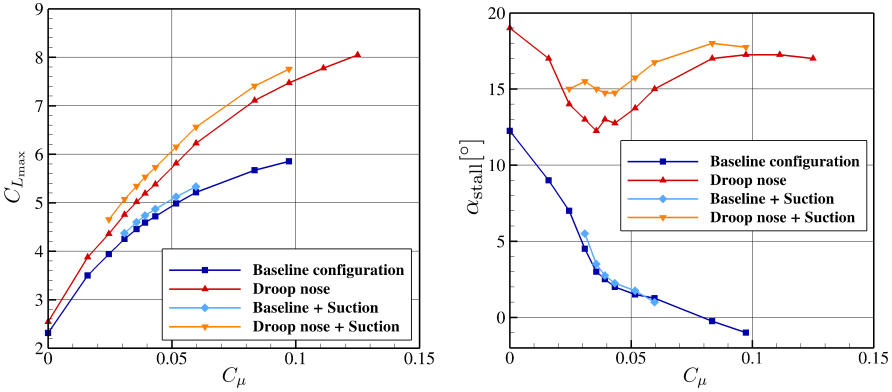

(a) C_μ effect on the maximum lift coefficient, $Re = 12 \cdot 10^6$, $M = 0.15$

(b) C_μ effect on the stall angle of attack, $Re = 12 \cdot 10^6$, $M = 0.15$

Figure 5.12: Effect of the C_μ on the performances at maximum lift.

entire range of tested jet momentum coefficients. In particular, the benefit is significantly larger for the droop-nose configuration. For $C_\mu = 0.0356$, the lift coefficient obtained with droop nose is enhanced by 6.5%, whereas the one of the baseline leading-edge configuration is improved by only 3% (figure 5.12b). Similarly, the stall angle is delayed by 2.75° for the droop-nose configuration, and by only 0.5° for the baseline geometry (figure 5.12a). Wall suction appears to shift the curves of performance upwards, maintaining the curve trends. This suggests that the stall mechanisms of the airfoils are not significantly affected by the suction device.

A further comparison is presented in table 5.3. Here, the jet momentum coefficients of three configurations - baseline leading edge, droop nose, and droop nose with wall suction $\beta = 10°$, $\gamma = 0°$, $x = 61\%$c - are set in order to achieve the target lift coefficient $C_{L_{max}} = 5.0$ at condition of maximum lift. With respect to the baseline geometry, the droop nose device reduces the momentum requirements by about 32%, which becomes about 43% if the wall suction is also employed. By consequence, the lift gain factor obtained with the baseline configuration, 60, is brought to 89 by the leading edge device and to 105 by the combination of droop nose and suction device.

Table 5.3: Blowing requirement and aerodynamic parameters for $C_{L_{max}} = 5.0$.

	C_μ	α_{stall}	$C_{L_{max}}$	$C_{M_{stall}}$	$LGF_{5,\ cruise}$
Baseline	0.0522	1.5°	5.0	-0.880	60.0
Droop nose	0.0353	12.3°	5.0	-0.724	88.7
Droop nose + suction	0.0298	15.4°	5.0	-0.641	105.0

The improvement of the stall angle of attack is also an important achievement, as it is increased to values suitable for landing and takeoff operations: from 1.5° to 12.3° by the droop nose and to 15.4° by the complete configuration. Finally, the pitching moment also benefits from the leading edge device and the wall suction. Thanks to the lower jet momentum and the different load distribution along the chord the pitching moment is improved by about 18% in the droop-nose configuration and by 27% including wall suction.

6 Dynamic Blowing

Mixing between two parallel streams at different velocities can be enhanced by inducing periodic perturbations in the mixing layer (see e.g. [125]). Applying this principle to the Coanda flap application investigated here may improve the mixing between the outer flow and the blowing jet, thus reducing the jet momentum required to avoid flow separation from the flap surface. In this chapter, the efficiency of unsteady actuation for the present configuration is assessed by superposing a periodic forcing signal to the constant momentum of a steady jet. The lift performance obtained by the modulated jet is then compared to the one resulting from a steady jet at the same averaged momentum coefficient.

The validation of the present numerical simulations will be performed with water-tunnel experiments, because of the possibility to achieve a high Reynolds number, $Re \approx 2 \cdot 10^6$. This raises the problem of implementing periodic blowing with an incompressible fluid, as the hammer effect would make high frequency control of the jet total pressure rather difficult with conventional techniques. This problem is addressed in the present work by numerically simulating two possible actuation mechanisms. The first case simulates an oscillating piezo-electric actuator lip installed over the jet nozzle, which controls the jet mass flow by varying the nozzle exit cross-section. The second case simulates the actuation of a valve at the plenum base that directly controls the jet total pressure. The flow interactions between the jet and the outer flow caused by the two actuation mechanisms are thoroughly investigated for two different frequencies and two oscillation amplitudes by means of URANS simulations [14]. Next, a wide range of actuation frequencies and amplitudes is tested, drawing a broad picture of the lift response of a Coanda flap to sinusoidal blowing actuation. The forcing signal is therefore expressed as $C_\mu(t) = \overline{C_\mu} + \langle C_\mu \rangle \sin(2\pi f t)$, and the jet momentum coefficient becomes simply $C_\mu = \overline{C_\mu} \pm \langle C_\mu \rangle$.

6.1 Actuation Technique

This section discusses the results obtained by the two actuation approaches, which generate jets with the same momentum coefficients but different velocities and mass flow rates. The periodic forcing obtained by lip motion is based on mass flow rate fluctuations caused by slot height variations (figure 6.1), while the velocity remains essentially constant. The lip deformation is performed keeping the upper and lower sides of the blowing nozzle parallel to each other at the jet exit, in order to avoid possible local flow separation caused by a divergent nozzle. The second approach varies the total pressure inside the plenum, which causes variations of momentum driven by velocity fluctuations. The mixing mechanisms generated by the two actuation approaches are investigated by means of velocity profiles extracted from the locations shown in figure 6.2.

The results discussed in this section are obtained for $\alpha = 0.0°$, $M = 0.15$, $Re = 12 \cdot 10^6$. The effect of the two actuation principles is analyzed at $F^+ = 0.125$ and $F^+ = 0.5$, for two amplitude levels of the forcing signal. F^+ represents the forcing frequency normalized by the freestream flow velocity and the flap length.

For the dynamic-lip control, the tested peak-to-peak amplitudes of the jet momentum fluctuations are generated by slot-height variations of 0.5 and 2 times the nominal slot height, $h_{s_{ref}} = 0.06\%$ chord, with the middle position set at $1.25\,h_{s_{ref}}$. This motion amplitudes, with a plenum pressure ratio of $p_{tj}/p_\infty = 1.14$, result in $C_\mu = 0.0285 \pm \langle 0.006 \rangle$ for the small amplitude and $C_\mu = 0.0275 \pm \langle 0.0225 \rangle$ for the large amplitude. For the pressure control approach, the total pressure at the plenum boundary condition was varied in order to achieve the same jet momentum fluctuations as obtained with the lip motion. The conclusions drawn by this comparison are similar for all the frequencies and amplitudes, so only one case is reported in detail here ($F^+ = 0.5$ and large amplitude).

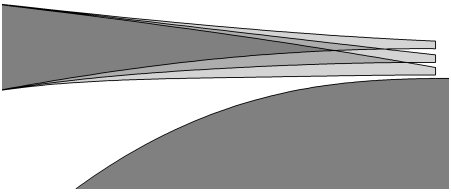

Figure 6.1: Lip deformation during an actuation cycle.

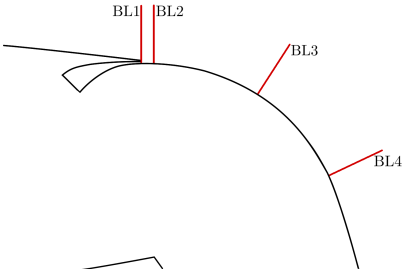

Figure 6.2: Extraction locations of the boundary layer velocity profiles.

The plots of figure 6.1 show that the outer-flow velocity profiles at BL1 have similar distributions for the two approaches, which suggests a limited effect of the actuation type on the outer flow upstream of the blowing slot. The jet velocity profiles at the nozzle exit section, on the other hand, exhibit the different characteristics of the two momentum-control approaches. With the lip-control technique, the jet velocity remains approximately constant throughout the actuation cycle, while the jet thickness varies. In this case, the momentum variations are driven by fluctuations of mass flow, obtained by variations of the slot height. On the other hand, the pressure-control approach generates jet velocity fluctuations, whereas the jet thickness remains constant. Therefore, the jet momentum is now controlled by both velocity and mass flow variations. At BL2, which is located $5h$ from the exit section, the difference of jet velocity and thickness between the two actuation techniques is still clearly visible. Further downstream, the turbulent mixing diffuses the jet momentum in wall-normal direction, resulting in the profiles of locations BL3 and BL4. Here, the velocity profiles obtained by the two actuation methods appear very similar. The large amplitude of the forcing signals causes the jet to reach very low C_μ, which results in a large separation over the flap. During these phases, the velocity profile of the pressure-control actuation at BL4 exhibits reverse flow near the wall. The boundary layer obtained by the lip motion, on the other hand, has always sufficient momentum to overcome the adverse pressure gradient in this area. This difference is slightly larger for the actuation at $F^+ = 0.125$, not shown here, whereas it disappears with smaller actuation amplitudes. For both actuation approaches, the maximum velocity at BL4 is reached after a short delay with respect to the C_μ fluctuations, which does not show significant differences between the two tested frequencies.

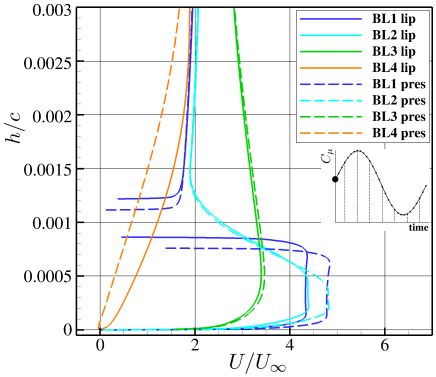

(a) $t = 0$

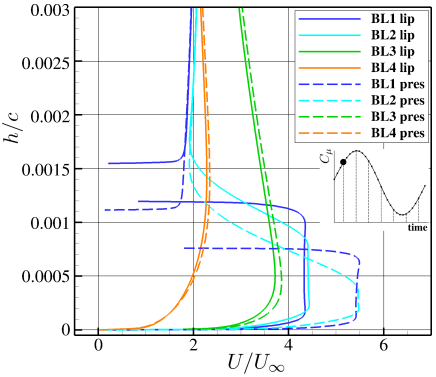

(b) $t = T/8$

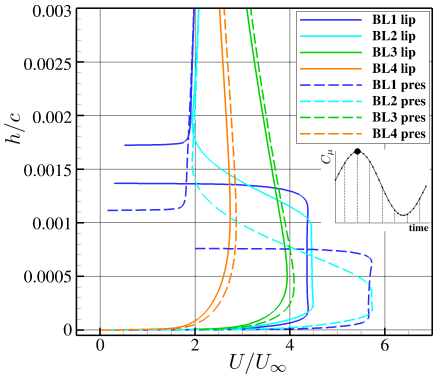

(c) $t = 2T/8$

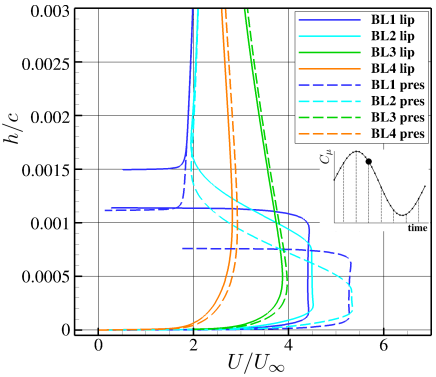

(d) $t = 3T/8$

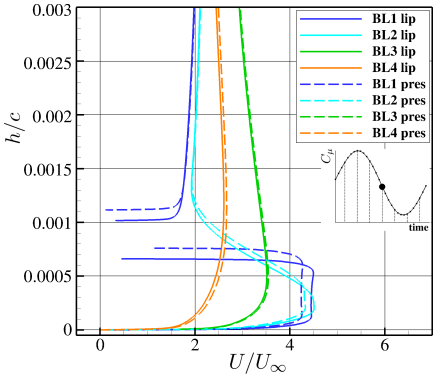

(e) $t = 4T/8$

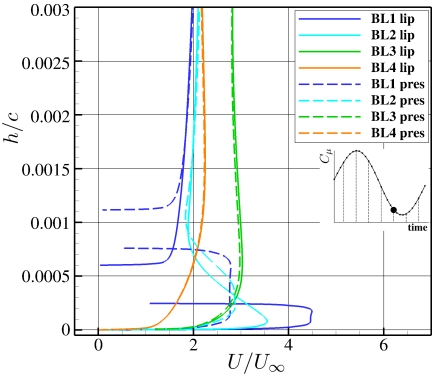

(f) $t = 5T/8$

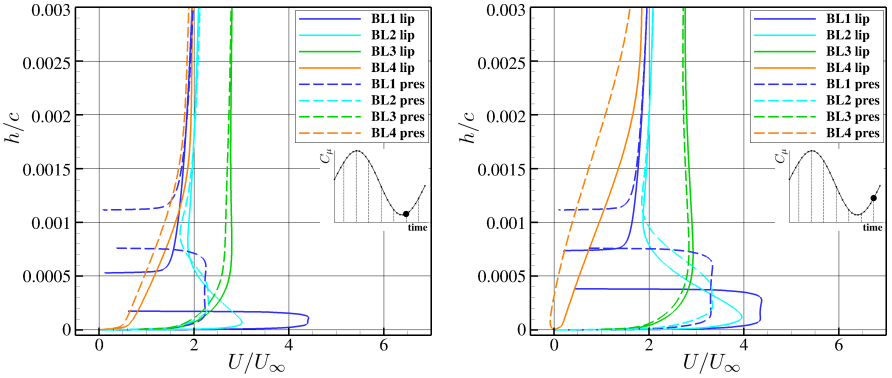

(g) $t = 6T/8$ **(h)** $t = 7T/8$

Figure 6.1: Velocity profiles at the selected locations for the two actuation approaches, $F^+ = 0.5$, large amplitude.

Table 6.1: Average jet momentum coefficient and lift coefficient with the respective standard deviations (SD) for the 4 test cases and two actuation techniques.

	Lip motion		Pressure control	
	$\overline{C_\mu}$ (SD)	$\overline{C_L}$ (SD)	$\overline{C_\mu}$ (SD)	$\overline{C_L}$ (SD)
$F^+ = 0.125$, small amplitude	0.028 (0.004)	3.649 (0.103)	0.028 (0.004)	3.644 (0.155)
$F^+ = 0.125$, large amplitude	0.027 (0.016)	3.304 (0.367)	0.029 (0.015)	3.299 (0.405)
$F^+ = 0.5$, small amplitude	0.029 (0.004)	3.675 (0.034)	0.028 (0.004)	3.666 (0.035)
$F^+ = 0.5$, large amplitude	0.028 (0.016)	3.403 (0.063)	0.029 (0.016)	3.416 (0.057)

The jet momentum coefficients obtained from the two actuation techniques and the resulting lift performances are summarized in table 6.1. The table reports also the amplitude of the fluctuations expressed in terms of standard deviation (SD). For both actuation methods, higher lift is obtained by the smaller blowing amplitudes and the higher frequency, with the amplitude having a larger impact on the resulting performance. The small-amplitude signals yield lift coefficients about 10% higher than the large-amplitude actuation for the $F^+ = 0.125$ case, and about 7.5% for the $F^+ = 0.5$ case. The difference of lift coefficient between the two signal frequencies is limited to about 3% for the large amplitude cases and 0.65% for the small amplitudes. The effects of frequency and amplitude on the lift performance are similar for both the lip-motion and the pressure-control approach, as the difference in average lift between the two approaches is less than 0.5% for all the four test cases.

6.2 Lift Performance of Unsteady Actuation

The efficiency of flow control with unsteady excitation is determined by numerous parameters, such as frequency, amplitude and mean value of the actuation signal, as well as freestream conditions and angle of attack. The response of the flow to these parameters depends on the specific configuration. The natural vortex-shedding frequency, for instance, is an important characteristic of the unactuated flow, as it represents the instabilities that will interact with the superposed forcing signal.

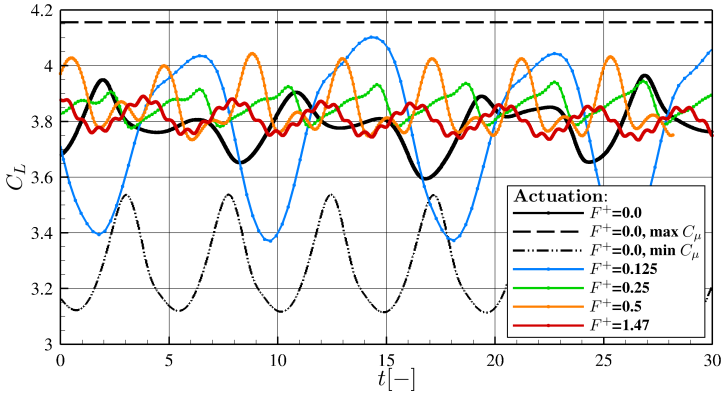

(a) Lift coefficient

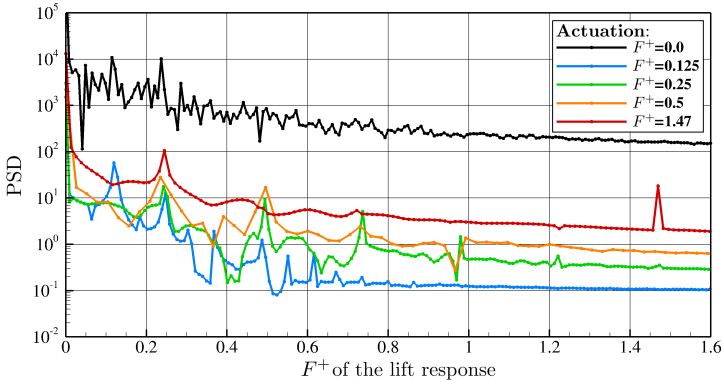

(b) Power Spectral Density of the lift responses

Figure 6.2: Lift responses to different forcing frequencies, $C_\mu = 0.0154 \pm \langle 0.0127 \rangle$, $\alpha = 18.0°$, $Re = 12 \cdot 10^6$, $M = 0.15$.

Figure 6.2 reports the lift response of the present Coanda flap configuration to a sinusoidal blowing with $C_\mu = 0.0154 \pm 0.0127$ at different frequencies. The lift generated by the airfoil with steady maximum, minimum and average jet momentum is reported for reference. The

constant lift at maximum steady blowing suggests that the flow does not present vortex shedding, whereas the lowest steady blowing exhibits a periodic behavior with $F^+ \approx 0.2$. The flow obtained with the lip fixed at middle height, on the other hand, shows a more irregular behavior. Apparently, the smaller separation yielded by the middle C_μ generates a faster vortex dynamics with a larger frequency content, as shown in figure 6.2b. However, two peaks can be observed in the Power Spectrum Density (PSD) of the steady blowing, $F^+ \approx 0.12$ and $F^+ \approx 0.24$. The latter is also visible in the spectrum of the actuated flows, for all the tested frequencies. The natural vortex shedding of the average blowing rate can be observed also in the lift trends of figure 6.2a in the form of a wave with frequency $F^+ \approx 0.24$ superposed to the forcing frequencies. The presence of these two frequencies is particularly visible for the $F^+ \approx 1.47$ actuation. The amplitude of the lift response is dependent on the actuation frequency. Low blowing frequencies cause larger lift fluctuations, as the flow over the Coanda flap has more time to adapt to the instantaneous blowing conditions.

Figure 6.3 shows the effect of frequency and amplitude of the jet momentum fluctuations on the average lift performance. The efficiency of unsteady blowing is here evaluated with respect to the flow obtained with steady blowing at $C_\mu = \overline{C_\mu}$. The smallest lip deformation, corresponding to $C_\mu = 0.015 \pm \langle 0.004 \rangle$, is the most effective, proving that very little perturbations are sufficient to improve the mixing between the jet and the outer flow. The most effective frequency is identified around $F^+ = 0.5$, which is about twice the vortex-shedding frequency of the flow separation with constant blowing.

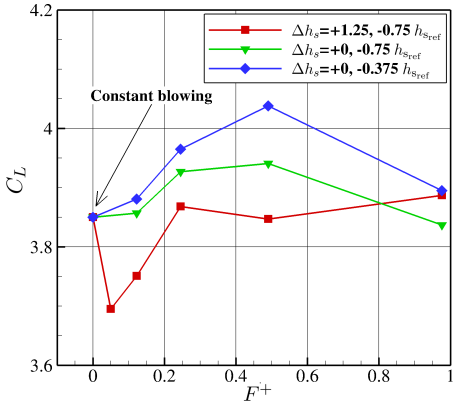

Figure 6.3: Effect of actuation frequency and amplitude on lift, for $\overline{C_\mu} = 0.015$, $\alpha = 18°$, $Re = 12 \cdot 10^6$, $M = 0.15$.

The flow topology over the flap surface plays a primary role in the efficacy of the unsteady excitation. Four flow topologies could be identified for steady blowing actuation, depending on the jet momentum coefficient and the angle of attack, as illustrated in figure 6.4a. Topology 1, 2 and 3 represent a steady URANS-solution (no fluctuations are observed in lift and the flow is steady although a time-resolving simulation is performed), whereas topology 4 results in a inherently fluctuating flow. These topologies react differently to periodic blowing, leading to different lift gains. In particular, topology 4 yields the highest lift-coefficient improvement, thanks to the interaction between the forcing signal and the

existing unsteady vortical structures. The lift improvement predicted by URANS simulations is about 5%, for a periodic forcing at $F^+ = 0.5$ and small amplitude (see figure 6.4b).

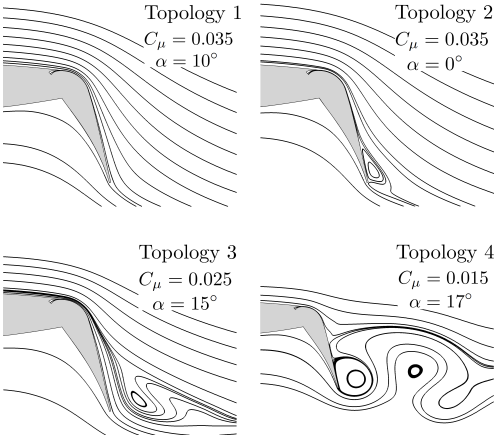

(a) Possible steady-blowing flow topologies over the flap

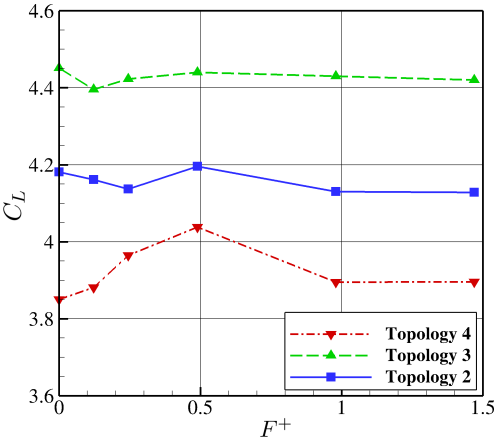

(b) Effect of the steady-blowing flow topology on lift generation with dynamic blowing

Figure 6.4: Effect of the steady-blowing flow topology on the efficacy of the periodic actuation, $Re = 12 \cdot 10^6$, $M = 0.15$.

The need for vortex shedding to efficiently use unsteady blowing limits its applicability to post-stall conditions and very low blowing, as under other conditions the flow field does not present unsteadiness. However, separated vortical structures are characterized by high streamlines curvature and strong pressure gradients, which may significantly affect the accuracy of the Spalart-Allmaras URANS approach employed here. The Reynolds averaging process prevents the numerical solution from resolving small turbulent structures, which may play an important role in such a complex flow. Moreover, the employed turbulence model is calibrated to provide high accuracy with mostly attached flows. Hence, the validity of the results shown here needs to be validated in the next phase of the project by means of experimental data and suited numerical approaches.

Nevertheless, a connection with previous work available in the literature can be made. The review presented in chapter 1 shows that unsteady mixing-layer excitation was successfully tested in many applications. However, only in some cases unsteady tangential blowing yielded a reduction of the required momentum coefficient. In many cases periodic blowing simply led to a reduction of jet mass flow [71, 69, 93, 129]. The reduction of required average mass flow, however, can be seen as the mathematical consequence of varying the jet velocity while maintaining a constant average momentum, as C_μ is directly proportional to the average of the square velocity. Consequently, if the target quantity was the jet power, which is proportional to the third power of the jet velocity, unsteady blowing would appear highly ineffective. From the literature, it seems that an actual gain in terms of C_μ can only be achieved if the blowing requirements are already relatively low. This happens for flap deflection angles until $35° - 40°$ or active Fowler flaps [170, 121, 105, 129, 78, 172, 55, 26]. In these cases, the additional momentum required to compensate the momentum deficit within the boundary layer is relatively low and the flow above the boundary layer can provide a valuable contribution. Therefore, the perturbations generated by unsteady actuation in the shear layer have a beneficial effect, as they enhance the momentum transfer in wall-normal direction. On the other hand, when the C_μ requirements are higher, the contribution of the outer flow momentum is no longer significant and the flow perturbations dissipate the momentum of jet reducing its effectiveness. Such dynamics were observed also in the present work, where a positive effect of unsteady excitation was obtained only when the C_μ was sufficiently low to let the outer-flow momentum bring a beneficial contribution to the boundary layer on the flap surface.

7 Conclusions and Future Developments

The present work focused on the improvement of a previously designed active high-lift system by means of numerical RANS simulations. The baseline high-lift configuration was the transonic DLR-F15 airfoil equipped with an internally-blown Coanda flap, which consisted of a gap-less flap deflected by 65° and a thin air jet tangentially blown over the upper surface of the flap. High lift levels were assured by the jet capability to follow the flap contour (Coanda effect) and deflect the surrounding flow downward. The present project aimed at enhancing the efficiency of the flow control device, which was expressed by the lift gain factor: the ratio between the lift gain yielded by the active system and the jet momentum required to obtained that gain. This was achieved by introducing a flexible droop nose, a wall-suction device and unsteady blowing. The employed freestream conditions represented the typical approach phase of a transport aircraft, with a Reynolds number of $12 \cdot 10^6$ and a Mach number of 0.15.

The state-of-the-art CFD DLR-TAU Code was employed to solve the RANS equations on a hybrid grid with a cell-vertex dual-grid approach. The convective fluxes were discretized using a second order central scheme with a scalar dissipation approach, whereas the convective fluxes of the turbulence model equation were treated with a second order Roe scheme. The implicit Backward-Euler system was solved with a LU-SGS scheme. The Spalart-Allmaras turbulence model was employed with a correction to account for curvature and rotation effects. Previous experimental validation work and a turbulence model analysis presented here showed that the numerical setting predicts the physics of the Coanda-flap flow with acceptable accuracy, including areas of separation and vortex interactions.

The Coanda flap enhances drastically the circulation around the airfoil and generates very high suction peaks over the leading edge. This results in a significant reduction of the stall angle of attack, which limits the capability of the active device to generate higher lift and undermines its potential for practical aircraft applications. This issue was addressed here by developing a flexible droop-nose device, according to the project guidelines to reduce noise emissions by avoiding the use of gaps. The first 20% of the airfoil chord was morphed by gradually increasing the airfoil thickness and the camber of the mean line in order to achieve a more effective pressure distribution. The aerodynamic sensitivities of the main geometrical parameters were investigated and the most effective shape was compared with a conventional slat configuration and a rigid droop nose device. The introduction of a droop nose device resulted in a drastic increase of maximum lift coefficient and stall angle of attack. Such improvements could also be used to reduce the momentum required by the Coanda jet to achieve a target lift. A maximum lift coefficient of 5.0 could be obtained with about 32% less jet momentum thanks to the flexible droop nose, with respect to the baseline configuration. In the same way, the slat device yielded a benefit of 56%, but at the likely increase of airframe noise due to high flow velocities at the slat trailing edge. Both solutions brought the stall angle of attack to values suitable for landing and takeoff operations: the flexible droop nose improved it from 1.5° to 12.3° and the slat device

reached 20.6°. Moreover, thanks to the more effective load distribution along the chord and the lower jet momentum requirement, the flexible droop nose improved the pitching moment by 18% and the slat configuration improved it by 65%. The flexible droop-nose device requires the use of flexible materials, which represent a non-conventional technology in the design and manufacture of aircraft lifting surfaces. Therefore, it was of interest to evaluate the actual gain yielded by the flexible configuration with respect to a rigid droop-nose device. The comparison showed that the target maximum lift coefficient of 5.0 could be achieved by the flexible droop nose with 9% less blowing momentum with respect to the rigid device, and the resulting stall angle was 2.3° higher. These gains increased for higher lift targets. Also, the analysis of stall mechanisms at different jet momentum coefficients highlighted some important phenomena that characterize the flow over the Coanda flap:

- gradual attachment of the wall jet to the flap surface for increasing angle of attack;
- separation between the wall jet and the outer flow in case of low blowing rates, which creates a complex recirculation area between the two flow streams;
- increase of stall angle of attack for increasing blowing rate, yielded by the droop nose device within a certain range of blowing rate.

The flexible droop-nose airfoil was also tested on a three-dimensional transport aircraft configuration. The results showed that three-dimensional flow dynamics affected the behavior of the Coanda flap already within the linear range of the lift curve, causing lower performance with respect to the two-dimensional analyses. The main cause of the observed loss of lift coefficient -about 0.2- was probably the wing sweep and the resulting boundary layer cross flow. This increased the viscous losses of the flow over the wing and reduced the flow turning provided by the Coanda jet. This mechanism was also responsible for the early leading edge stall observed with the baseline leading-edge configuration. A comparison between the performances obtained from the three-dimensional wing and the isolated airfoil showed that a middle section of the 3D wing reached maximum lift at effective angle $\alpha_e = -3°$, which was about 6° less than what observed during two-dimensional analyses. The lift and stall angle improvements yielded by the droop nose were similar to the ones emerged from the airfoil studies, although the stall mechanisms were different. In the case of the 3D droop-nose configuration, a strong cross flow from the fuselage to the wing upper side appeared for angles of attack greater than 16°, due to the very low pressure over the wing. As a consequence, a thick boundary layer reached the Coanda flap and caused separation between the jet and the outer flow, which resulted in a sudden decrease of lift. In order to avoid such three-dimensional flow mechanisms, conventional wing-root configurations need to be adapted to the high level of circulation yielded by active high-lift devices. Therefore, the integration of the active high-lift system must be taken into account in the early phases of the aircraft design.

Providing compressed air to the active flow-control systems is one of the main challenges rising from the integration of an active high-lift device into the synergistic structure of the aircraft systems. One of the solution developed within the framework of the SFB 880 research center is installing electrical compact compressors into the wing. In this configuration, the compressor intakes have the potential to be used as additional flow-control devices to manipulate the flow behavior in the proximity of the airfoil surface. Therefore, the design of a compressor intake is of particular interest and was performed here aiming at maximizing the total pressure recovery along the suction duct and the lift generated by the airfoil. The analyses showed that a narrower slot induces higher lift, but also larger viscous losses along the duct, which reduce the total pressure recovery. For this reason, the two objectives were combined into one single quantity, a balanced lift coefficient,

that allowed evaluating and comparing the overall performance of the different suction-slot configurations. The results highlighted high efficiency of wall suction on the upper side of the airfoil, upstream of the Coanda flap. In this case, wall suction led to a reduction of the boundary layer thickness upstream of the blowing slot, which is beneficial for the operation of the Coanda flap. This proved that better performances can be achieved by exploiting synergies between the two flow control devices. Using suction on the flap surface to avoid flow separation in case of low jet momentum turned out to be ineffective due to the complex flow topology over the flap. The suction slot was also tested near the flap hinge, which is an area of high pressure. In this case, the total pressure at the end of the suction duct was higher than for the other suction locations, but the resulting lift coefficient was significantly lower. In conclusion, thanks to a careful design of the wall suction device, the jet momentum required to achieve $C_{L_{\max}} = 5.0$ was reduced by 16%, with respect to the same configuration without suction, and the maximum angle of attack was increased from 12.3° to 15.4°. Consequently, the lift gain factor was increased from 89 to 105. Moreover, it was observed that wall suction on the configuration with the droop-nose device was about twice as effective as it was on the baseline airfoil.

Figure 7.1 summarizes the improvements yielded by the droop nose and the wall suction at maximum lift conditions. In comparison to the baseline configuration, the lift gain factor corresponding to $C_{L_{\max}} = 5.0$ was improved by 75% and the stall angle of attack was increased from 1.5° to 15.4°. Note that for the droop-nose configurations, the stall angle of attack increases with the jet momentum between $C_\mu = 0.035$ and $C_\mu = 0.1$. This behavior is very convenient for practical applications, as an increase of blowing rate has the double effect of increasing lift and delaying stall, representing a valuable feature for safety during low-speed flight. It is worth reminding that the performances corresponding to non-optimal blowing rates, i.e. $C_\mu \neq 0.036$, would be slightly different if the flap deflection was adapted to the jet momentum. However, the trends presented in figure 7.1 would remain unchanged.

Finally, the response of the Coanda-flap to a periodic forcing implemented through modulation of the jet momentum was assessed. The potential of an unsteady jet is to enhance the turbulent mixing between the outer flow and the blowing jet, which reduces the momentum required to avoid flow separation from the flap surface. Two approaches to implement periodic blowing were compared, where the jet momentum fluctuations were obtained by varying different jet characteristics. The first approach was based on the deformation of the lip of the blowing nozzle, which allowed controlling the jet exit cross-section. As a result, the jet momentum fluctuations were driven by mass flow variations, while the velocity remained approximately constant. With the second technique, the total pressure inside the jet plenum was controlled with a fixed nozzle geometry, thus varying both mass flow and velocity of the jet. Two frequencies and two signal amplitudes were tested, providing a comparison basis for the two techniques. A detailed analysis of the flow development over the Coanda surface showed that prominent differences between the two approaches were limited to a small region near the blowing slot. Only under conditions of very low blowing momentum and low frequency, did the jet with constant velocity present a smaller separation, and thus a slightly larger average lift. The results also showed a similar dynamic response of the flow to the two actuation methods, which suggested that a similar underlying mechanism was behind the enhanced mixing.

The effects of sinusoidal blowing on the lift performance were thoroughly investigated for different actuation signals and angles of attack. The unsteady actuation was compared to constant blowing at the same average jet momentum coefficient. The constant-blowing vortex-shedding frequency was always visible in the power spectrum density of the unsteady-

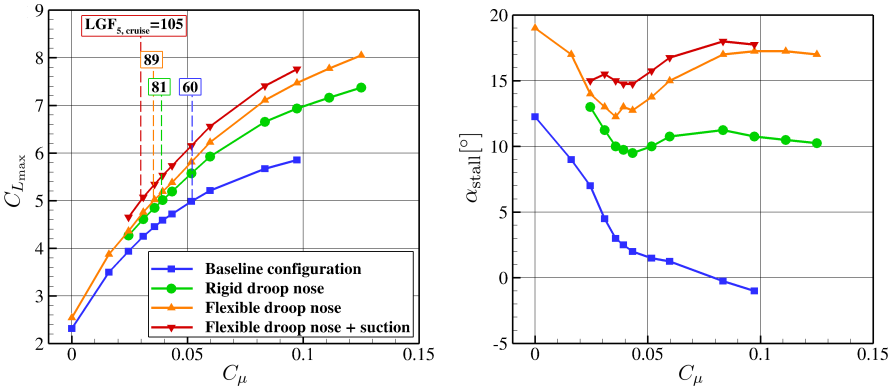

(a) Maximum lift coefficient and Lift Gain Factor for $C_{L_{\max}} = 5.0$

(b) Stall angle of attack

Figure 7.1: Maximum lift performance of the baseline and improved configurations for different blowing rates.

blowing response. The amplitude of the response, however, was related to the actuation frequency and amplitude. Higher frequencies resulted in smaller lift fluctuations. The largest lift gain, with respect to constant blowing, was obtained at $F^+ = 0.5$, which was about twice the vortex-shedding frequency of the steady blowing case. The amplitude effect was also investigated, showing that low signal amplitudes yielded higher lift gains. As a result of this sensitivity analysis, the time-averaged lift could be improved by 5% with respect to constant blowing at the same average momentum coefficient.

Vortex shedding with steady blowing turned out to be an important requirement for the effectiveness of the unsteady actuation, as only in presence of a flow instability it was possible to improve lift by jet momentum fluctuations. With steady blowing, the flow topology over the flap is defined by the blowing momentum and the angle of attack. The Spalart-Allmaras URANS simulations conducted here predicted unsteady flow separation only for very low jet momentum coefficients and high angles of attack, which correspond to post-stall conditions. However, it is possible that more sophisticated simulation approaches would predict flow instability closer to maximum lift conditions, thanks to a richer description of the physics of the turbulent structures. On the other hand, previous studies available in the literature show that gains in terms of jet momentum coefficient were only achieved for low actuation levels, which would support the findings of the present work.

Further research on unsteady excitation of the mixing layer will be conducted in the Research Center SFB880 with the aim of reducing the power requirements of the high-lift system. The first step will be the validation of the results presented here by means of more accurate turbulence models and water-tunnel experiments. Next, unsteady blowing will be investigated on a three-dimensional wing model in order to assess the potentials of span-wise jet-momentum perturbations, obtained by periodically varying the nozzle-lip deformation along the wing span. Finally, close-loop flow control will be implemented to

adapt the blowing rate to the current flow condition, in order to further reduce the overall blowing momentum requirement.

In conclusion, the present work led to substantial improvements of the system efficiency and to a deeper understanding of the operating principle of a Coanda flap. These achievements represent an important step forward in the long process that began several decades ago to increase the technological readiness of active flow-control technologies for a broad application in the aeronautical industry. For instance, within the multidisciplinary framework of the Collaborative Research Center SFB 880, the results presented here are the basis for current and future research carried out by other teams. The numerous simulations performed with different geometrical configurations and blowing rates represent a valuable aerodynamic database for aircraft preliminary design, flight-mechanics models, and lower order aerodynamic prediction methods for aircraft with active high-lift systems. The shapes and loads resulting from the droop-nose design lay down the requirements for the development of the flexible materials and kinematic mechanisms needed for the actual manufacture of the device. The definition of the suction-slot location and geometry, along with the jet momentum requirements, represent the boundary conditions for the design of the compact electric compressors. Finally, the unsteady computations serve as basis for the development of reduced order models able to predict the transient and post-transient flow conditions over the flap with periodic blowing, which are needed to implement close-loop control laws.

Bibliography

[1] B. Allan, G. Jones, and J. Lin. "Reynolds-Averaged Navier-Stokes simulation of a 2D circulation control wind tunnel experiment". In: *49th AIAA Aerospace Sciences Meeting*. AIAA 2011-25. Orlando, FL, USA, 2011 (see pp. 12, 39).

[2] J. S. Attinello. "Design and engineering features of flap blowing installations." In: *Boundary Layer and Flow Control. Its Principles and Application*. Ed. by G. V. Lachmann. Vol. 1. Pergamon Press, New York, 1961, pp. 463–515 (see pp. 5, 6, 19).

[3] Advisory Council for Aviation Research and Innovation in Europe. "Flightpath 2050 - Europe's Vision for Aviation: Report on the High Level Group on Aviation Research". ISBN 978-92-79-19724-6. 2011 (see p. 1).

[4] T. Ball, S. Turner, and D. D. Marshall. "Short takeoff performance using circulation control". AIAA 2008-174. 2008 (see p. 19).

[5] R. Becker et al. "Adaptive Closed-Loop Separation Control on a High-Lift Configuration Using Extremum Seeking". In: *AIAA Journal* 45.6 (2007), pp. 1382–1392 (see p. 18).

[6] L. D. Birckelbaw. "High speed aerodynamics of upper surface blowing aircraft configurations". AIAA-92-2611-CP. 1992 (see p. 8).

[7] J. Blazek. "Computational Fluid Dynamics: Principles and Applications". Ed. by Elsevier Science. 2005 (see p. 37).

[8] P. J. Bobbitt and R. Margason. "Analysis of the take-off and landing of powered-lift aircraft". AIAA 2007-1256. 2007 (see p. 19).

[9] A. J. Bohn and M. D. Shovlin. "Upper surface blowing noise of the NASA Ames quiet shorthaul research airplane". AIAA 80-1064. 1980 (see p. 8).

[10] J. A. Braden, J. P. Hancock, and K. P. Burdges. "Cruise aerodynamics of USB nacelle/wing geometric variations". Tech. rep. NASA-SP-406. Lockheed-Georgia company, 1976 (see p. 8).

[11] P. Bradshaw and F. Y. F. Wong. "The reattachment and relaxation of a turbulent shear layer". In: *Journal of Fluid Mechanics* 52.1 (1972), pp. 113–35. DOI: 10.1017/S002211207200299X (see p. 4).

[12] F.J. Brandsma et al. "Leading edge vortex flow computations and comparison with DNW-HST wind tunnel data". In: *RTO/AVT Symposium on Advanced Flow Management: Part A - Vortex Flows and High Angle of Attack for Military Vehicles*. NLR-TP-2001-238. Loen, Norway, 2001 (see pp. 11, 35, 42).

[13] V. Brunet, J. Dandois, and C. Verbeke. "Recent Onera Flow Control Research on High-Lift Configurations". In: *Aerospace Lab* 6 (2013). Al 06-05 (see p. 1).

[14] M. Burnazzi et al. "Numerical Assessment of two Periodic Actuation Approaches for Flow Separation Control". In: *63. Deutscher Luft- und Raumfahrtkongress 2014, Augsburg.* (2014) (see p. 87).

[15] M. Burnazzi and R. Radespiel. "Assessment of leading-edge devices for stall delay on an airfoil with active circulation control". In: *CEAS Aeronautical Journal* 5.4 (2014). DOI: 10.1007/s13272-014-0112-5 (see pp. 39, 49, 51, 55, 56, 58, 60, 65).

[16] M. Burnazzi and R. Radespiel. "Design and Analysis of a Droop Nose for Coanda Flap Applications". In: *AIAA Journal of Aircraft* 51.5 (2014). DOI: 10.2514/1.C032434 (see pp. 40, 49, 51, 54, 58).

[17] M. Burnazzi and R. Radespiel. "Synergies between suction and blowing for active high-lift flaps". In: *CEAS Aeronautical Journal* 6.2 (2015), pp. 305–318. DOI: 10.1007/s13272-014-0146-8 (see pp. 75, 77, 79, 81).

[18] M. Burnazzi, J. Thiemeier, and R. Radespiel. "Numerical Stall Behavior Investigation of an Aircraft equipped with Coanda Flap and Droop Nose". In: *New Results in Numerical and Experimental Fluid Mechanics X: Contributions to the 19th STAB/DGLR Symposium Munich, Germany, 2014* (2016), pp. 3–16. DOI: 10.1007/978-3-319-27279-5_1 (see pp. 67, 69).

[19] L. M. Butzel et al. "Cabin noise behavior of a usb stol transport". AIAA 77-1365. 1977 (see p. 7).

[20] R. D. Cecora et al. "Differential Reynolds Stress Modeling for Aeronautics". In: *AIAA Journal* 53.9 (2012), pp. 739–755 (see pp. 36, 42).

[21] P. A. Chang et al. “Full Reynolds-stress modeling of circulation control airfoils”. In: *Applications of circulation control technology, Progress in astronautics and aeronautics*. Ed. by R. D. Joslin and G. S. Jones. Vol. 214. American Institute of Aeronautics and Astronautics, 2006, pp. 23–68 (see p. 11).

[22] P. K. Chank. *Control of Separation*. McGraw-Hill, New York. 1976 (see p. 3).

[23] C. Chen, R. Seele, and I. Wygnanski. “Flow Control on a Thick Airfoil Using Suction Compared to Blowing”. In: *AIAA Journal* 51.6 (June 2013). DOI: 10.2514/1.J052098 (see pp. 8, 77).

[24] V. Ciobaca. “Parameter Study for a Slatless 2D High-Lift Airfoil with Active Separation Control Using a URANS Approach”. In: *Notes on Numerical Fluid Mechanics and Multidisciplinary Design*. Ed. by A. Dillmann et al. Vol. 121. Springer, 2013, pp. 135–142 (see p. 18).

[25] V. Ciobaca and J. Wild. “An Overview of Recent DLR Contributions on Active Flow-Separation Control Studies for High-Lift Configurations”. In: *Journal Aerospace Lab* 6 (2013) (see p. 19).

[26] V. Ciobaca et al. “Active Flow Separation Control on a High-Lift Wing-Body Configuration”. In: *AIAA Journal of Aircraft* 50.1 (2013), pp. 56–72 (see pp. 18, 94).

[27] J. A. Cochrane and R. J. Carros. “Hybrid upper surface blown flap propulsive-lift concept for the QSRA”. In: *AIAA Journal of Aircraft* 13.11 (1976) (see p. 7).

[28] J. A. Cochrane, D. W. Riddle, and V. C. Stevens. “Quiet Short-Haul Research Aircraft - The first three years of flight research”. AIAA 81-2625. 1981 (see p. 7).

[29] J. J. Cornish. “Some aerodynamic and operational problems of STOL aircraft with boundary-layer control”. In: *AIAA Journal of Aircraft* 2.2 (1965) (see p. 7).

[30] D. Schwamborn and A. D. Gardner and H. von Geyr and A. Krumbein and H. Lüdeke and A. Stürmer. “Development of the DLR TAU-Code for Aerospace Applications”. Bangalore, India, 2008 (see p. 36).

[31] H.S. Dol, J.C. Kok, and B. Oskam. “Turbulence Modelling for Leading-Edge Vortex Flows”. In: *40th Aerospace Sciences Meeting & Exhibit*. A02-14303. Reno, NV, USA, 2002 (see p. 35).

[32] F. A. Dvorak. "Calculation of turbulent boundary layers and wall jets over curved surfaces". In: *AIAA Journal* 11.4 (1973) (see p. 10).

[33] F. A. Dvorak and R. J. Kind. "Analysis method for viscous flow over circulation-controlled airfoils". In: *AIAA Journal of Aircraft* 16.4 (1979) (see p. 10).

[34] "http://en.wikipedia.org/wiki/Advanced_Medium_STOL_Transport" (see p. 7).

[35] R. J. Englar. "Overview of circulation control pneumatic aerodynamics: blown force and moment augmentation and modification as applied primarily to fixed-wing aircraft". In: *Applications of Circulation Control Technology, Progress in Astronautics and Aeronautics*. Ed. by D. Joslin and G. S. Jones. Vol. 214. AIAA, 2006, pp. 23–68 (see pp. 9, 15).

[36] R. J. Englar. "Circulation Control Pneumatic Aerodynamics: Blown Force and Moment Augmentation and Modification; Past, Present & Future". In: (June 2000). AIAA 2000-2541. DOI: 10.2514/6.2000-2541 (see p. 5).

[37] R. J. Englar and G. G. Huson. "Development of advanced circulation control using high-lift airfoils". In: *AIAA Journal of Aircraft* 21.7 (1984), pp. 476–483 (see p. 9).

[38] R. J. Englar et al. "2-D Circulation Control Airfoil Benchmark Experiments Intended for CFD Code Validation". In: *47th AIAA Aerospace Sciences Meeting Including The New Horizons Forum and Aerospace Exposition*. AIAA 2009-902. Orlando, FL, USA, 2009 (see p. 12).

[39] R. J. Englar et al. "Application of Circulation Control to Advanced Subsonic Transport Aicraft, Part I: Airfoil Development". In: *AIAA Journal of Aircraft* 31.5 (1994), pp. 1160–1168 (see pp. 9, 15, 16).

[40] R. J. Englar et al. "Application of Circulation Control to Advanced Subsonic Transport Aircraft, Part II: Transport Application". In: *AIAA Journal of Aircraft* 31.5 (1994), pp. 1169–1177 (see pp. 9, 10).

[41] R. J. Englar et al. "Development of circulation control technology for application to advanced subsonic transport aircraft". In: *AIAA Journal of Aircraft* 31.7 (1994), pp. 1160–1177 (see p. 9).

[42] J. C. Eppel. *Quiet Short-Haul Research Aircraft familiarization document, revision 1*. Tech. rep. NASA Technical Memorandum 81298. Ames Research Center, 1981 (see p. 7).

[43] A. Esposito et al. “Redesign of Boeing 777-300 with ESTOL capabilities”. AIAA 2007-1045. 2007 (see p. 8).

[44] A. J. A. Favre. “Equations des gaz turbulents compressibles”. In: *Journal de Mécanique* 4.3, 4 (1965) (see p. 29).

[45] J. Flatt. “The History of Boundary Layer Control Research in the United States of America”. In: *Boundary Layer and Flow Control. Its Principles and Application*. Ed. by G. V. Lachmann. Vol. 1. Pergamon Press, New York, 1961, pp. 122–143 (see p. 4).

[46] K. Gersten and R. Lohr. “Untersuchungen uber die Auftriebserhohung eines Tragflugels bei gleichzeitigem Ausblasen an der Hinterkantenklappe und an der Profilnase”. In: *Institutsbericht 62/34, Institut of Fluid Mechanics, Technische Universität Braunschweig* (1962) (see p. 20).

[47] J. S. Gibson. “New developments in blown flap noise technology”. NASA CR-145086. 1976 (see p. 8).

[48] J. S. Gibson and N. Searle. “Characteristics of usb noise”. NASA-SP-406. 1976 (see p. 8).

[49] M. B. Glauert. “The Application of the Exact Methods of Aerofoil Design”. In: *Aeronautical Research Council Reports and Memoranda*. Her Majesty’s Stationery Office, Rept. and Memoranda No. 2683, London. 1955 (see p. 6).

[50] M. B. Glauert et al. “Wind Tunnel Tests on a Thick Suction Aerofoil with a Single Slot”. *Aeronautical Research Council*. RM-2646. 1948 (see p. 6).

[51] D. Greenblatt. “Dual Location Separation Control on a Semi-Span Wing”. In: *23rd AIAA Applied Aerodynamics Conference*. AIAA 2005-5085. Toronto, Canada, 2005 (see p. 15).

[52] D. Greenblatt and I. Wygnaski. “The control of flow separation by periodic excitation”. In: *Progress in Aerospace Sciences*. Vol. 36. Pergamon Press, 2000, pp. 487–545 (see pp. 1, 16, 17).

[53] M. Gad el Hak. *Flow Control, Passive Active Reactive Flow Management*. Ed. by Cambridge University Press. 2000 (see p. 9).

[54] M.Gad el Hak and D. M. Bushnell. “Separation Control: Review”. In: *ASME Journal of Fluids Engineering* 113.1 (1991), pp. 5–30. DOI: 10.1115/1.2926497 (see pp. 1, 3, 4).

[55] F. Haucke and W. Nitsche. “Active Separation Control on a 2D High-Lift Wing Section Towards High Reynolds Number Application”. In: *31st AIAA Applied Aerodynamics Conference*. San Diego, CA, USA, 2013 (see pp. 18, 94).

[56] M. R. Head and D. G. Clark. “Flight experiment on suction for high lift”. AIAA 65-750. 1965 (see p. 7).

[57] W. Heinze, C. M. Österheld, and P. Horst. “Multidisziplinäres Flugentwurfsverfahren PrADO - Programmentwurf und Anwendung im Rahmen von Flugzeug-Konzeptstudien”. In: *DGLR-Jahrbuch 2001*. Vol. 3. Bonn, Germany, 2001, pp. 1701 –1712 (see p. 67).

[58] A. Hellsten. “Some improvements in Menter’s $k - \omega$ SST turbulence model”. AIAA 98-2554. 1998 (see p. 11).

[59] “http://en.wikipedia.org/wiki/Grumman_F9F_Panther” (see p. 6).

[60] “https://en.wikipedia.org/wiki/Boeing_YC-14” (see p. 8).

[61] “https://en.wikipedia.org/wiki/McDonnell_Douglas_YC-15” (see p. 8).

[62] W. L. Sellers III, G. S. Jones, and M. D. Moore. “Flow Control Research at NASA Langley in Support of High-Lift Augmentation”. In: *2002 Biennial International Powered Lift Conference and Exhibit*. AIAA 2002-6006. Williamsburg, VA, USA, 2002 (see p. 17).

[63] S. Jakirlić and K. Hanjalić. “A New Approach to Modelling Near-Wall Turbulence Energy and Stress Dissipation”. In: *Journal of Fluid Mechanics* 459 (2002), pp. 139–166 (see pp. 36, 42).

[64] A. Jameson, W. Schmidt, and E. Turkel. “Numerical Solution of the Euler Equations by Finite Volume Methods Using Runge Kutta Time Stepping Scheme”. In: *14th Fluid and Plasma Dynamics Conference*. AIAA 81-1259. Palo Alto, CA, USA, 1981 (see pp. 37, 39).

[65] A. Jameson and E. Turkel. “Implicit Schemes and LU-Decompositions”. In: *Mathematics of Computations* 37.156 (1981), pp. 385–397 (see p. 38).

[66] C. Jensch, K. C. Pfingsten, and R. Radespiel. “Numerical investigation of leading edge blowing and optimization of the slot and flap geometry for a circulation control airfoil”. In: *New Results in Numerical and Experimental Fluid Mechanics VII (NNFM)*. Ed. by A. Dillmann et al. Vol. 112. Springer, 2010, pp. 183–190 (see pp. 15, 24, 26).

[67] C. Jensch et al. “Design Aspects of a Gapless High-Lift System with Active Blowing”. In: *Deutscher Luft- und Raumfahrtkongress 2009*. Aachen, Germany, 2009 (see pp. 15, 20, 24).

[68] A. Jirásek and O. Amoignon. "Design of a high-lift system with a droop nose device". In: *AIAA Journal of Aircraft* 46 (2009), pp. 731–734 (see p. 15).

[69] G. S. Jones and R. J. Englar. "Advances In Pneumatic-Controlled High-Lift Systems Through Pulsed Blowing". In: *AIAA 21st Applied Aerodynamics Conference*. AIAA 2003-3411. Orlando, FL, USA, 2003 (see pp. 17, 94).

[70] G. S. Jones, C.-S. Yao, and B. G. Allan. "Experimental Investigation of a 2D Supercritical Circulation-Control Airfoil Using Particle Image Velocimetry". In: *3rd AIAA Flow Control Conference*. AIAA 2006-3009. San Francisco, CA, USA, 2006 (see p. 12).

[71] G. S. Jones et al. "An Active Flow Circulation Controlled Flap Concept for General Aviation Aircraft Applications". In: *AIAA 1st Flow Control Conference*. AIAA 2002-3157. St. Louis, MO, USA, 2002 (see pp. 17, 94).

[72] G. S. Jones et al. "Overview of CFD Validation Experiments for Circulation Control Applications at NASA". In: *International Powered Lift Conference, Royal Aeronautical Society*. London, England, 2008 (see p. 12).

[73] M. Kamruzzaman. "Aerodynamic investigation of an airfoil with upper surface blowing using the numerical flow solver TAU". Diploma Thesis at Institut of Fluid Mechanics, Technische Universität Braunschweig. 2005 (see p. 8).

[74] T. S. Keeble. "Development in Australia of a Thick Suction Wing". In: *Proceedings of the fourth Anglo-American Aeronautical Conference*. Vol. 45. Royal Aeronautical Society, 1951 (see p. 6).

[75] D. Keller. "Numerical Approach Aspects for the Investigation of the Longitudinal Static Stability of a Transport Aircraft with Circulation Control". In: *New Results in Numerical and Experimental Fluid Mechanics IX (NNFM)*. Ed. by A. Dillmann et al. Vol. 124. Springer, 2014, pp. 13–22 (see p. 68).

[76] D. Keller. "Numerical Investigation of Engine Effects on a Transport Aircraft with Circulation Control". In: *AIAA Journal of Aircraft* 52.2 (2015), pp. 421–438 (see p. 68).

[77] B. R. Kennedy. "Globemaster III: Acquiring the C-17". Air Mobility Command Office of History. 2004 (see p. 7).

[78] A. Khodadoust and A. Shmilovich. "High Reynolds Number Simulations of Distributed Active FLow Control for a High-Lift System". In: *25th AIAA Applied Aerodynamics Conference*. AIAA 2007-4423. Miami, FL, USA, 2007 (see pp. 18, 94).

[79] S. Kikuhara and K. Tokuda. "A new STOL flying boat design". In: *AIAA Journal of Aircraft* 3.5 (1966) (see p. 7).

[80] J. Kim, S. J. Kline, and J. P. Johnston. "Investigation of a reattaching turbulent shear layer: flow over a backward-facing step". In: *ASME Journal of Fluid Engineering* 102.3 (1980), pp. 302–308. DOI: 10.1115/1.3240686 (see p. 4).

[81] R. J. Kind and D. J. Maull. "An experimental investigation of a low-speed circulation-controlled aerofoil". In: *The Aeronautical Quarterly* 19 (1968), pp. 170–182 (see p. 10).

[82] M. Kintscher et al. "Design of a Smart Leading Edge Device for Low Speed Wind Tunnel Tests in the European Project SADE". In: *International Journal of Structural Integrity* 2.4 (2011) (see p. 14).

[83] D. G. Koenig and K. Aoyagi. "Maximum lift of upper surface blowing STOL aircraft with swept wings". AIAA 75-868. 1975 (see p. 8).

[84] A. G. Kravchenko and P. Moin. "On the effect of numerical errors in large eddy simulations of turbulent flows". In: *Journal of Computational Physics* 131 (1997), pp. 310–322 (see p. 37).

[85] N. Kroll et al. "MEGAFLOW - A Numerical Flow Simulation Tool for Transport Aircraft Design". In: *ICAS Congress*. Toronto, Canada, 2002 (see p. 36).

[86] T. Kühn and J. Wild. "Aerodynamic Optimization of a Two-Dimensional Two-Element High Lift Airfoil with a Smart Droop Nose Device". In: *1st EASN Association Workshop on Aerostructures*. Paris, France, 2010 (see p. 49).

[87] G. V. Lachmann. *Boundary Layer and Flow Control. Its Principles and Application*. Vol. 1. Pergamon Press, New York, 1961 (see p. 6).

[88] G. V. Lachmann. *Boundary Layer and Flow Control. Its Principles and Application*. Vol. 2. Pergamon Press, New York, 1961 (see p. 6).

[89] E. M. Lee-Rausch, V. N. Vatsa, and C. L. Rumsey. "Computational Analysis of Dual Radius Circulation Control Airfoils". In: *36th AIAA Fluid Dynamics Conference*. AIAA 2006-3012. San Francisco, CA, USA, 2006 (see p. 11).

[90] R. J. LeVeque. *Numerical Methods for Conservation Laws*. Ed. by Springer Science & Business Media. 1992 (see p. 38).

[91] J. Li and C. Liu. "Direct Numerical Simulation for Flow Separation Control with Pulsed Jets". In: *41st Aerospace Sciences Meeting and Exhibit*. AIAA paper 2003-0611. Reno, NV, USA, 2003 (see p. 13).

[92] Y. Liu et al. "Numerical Simulations of the Steady and Unsteady Aerodynamic Characteristics of a Circulation Control Wing Airfoil". In: *39th AIAA Aerospace Sciences Meeting and Exhibit*. AIAA 2001-0704. Reno, Nevada, 2001 (see p. 17).

[93] Y. Liu et al. "Computational Evaluation of the Steady and Pulsed Jet Effects on the Performance of a Circulation Control Wing Section". In: *42nd AIAA Aerospace Sciences Meeting and Exhibit*. AIAA 2004-56. Reno, NV, USA, 2004 (see pp. 17, 94).

[94] Jr. L. K. Loftin and D. L. Burrows. "Investigations Relating to the Extension of Laminar Flow by Means of Boundary-Layer Suction through Slots". In: *NACA Technical Note* (1961) (see p. 6).

[95] N. Madavan and M. Rogers. "Direct Numerical Simulation of Flow Around a Circulation Control Airfoil". In: *5th Flow Control Conference*. AIAA 2010-4577. Chicago, IL, USA, 2010 (see p. 14).

[96] M. Maita. "Jet-wing/flap interaction noise from external upper surface blowing configuration". In: *Proceedings of the Japan National Congress for Applied Mechanics*. Tokyo, 1978 (see p. 8).

[97] M. Maita, H. Fujieda, and M. Morita. "Powered lift aerodynamics of usb stol aircraft". AIAA 83-1848. 1983 (see p. 7).

[98] M. Maita and T. Torisaki. "Acoustic characteristics of the external upper surface blowing propulsive-lift configuration". AIAA 80-1063. 1980 (see p. 8).

[99] M. Mani, J. A. Ladd, and W. W. Bower. "Rotation and Curvature Correction Assessment for One-and Two-Equation Turbulence Models". In: *Journal of Aircraft* 41.2 (2004), pp. 268–273 (see p. 11).

[100] J. L. Martin. "The Quiet Short-Haul Research Aircraft (QSRA)". NASA Ames Research center. 1980 (see p. 7).

[101] E. C. Maskell. "Flow Separation in Three Dimensions". In: *Royal Aircraft Establishment RAE Report* Aero.-2565 (1955) (see pp. 3, 4).

[102] F. W. May and G. E. Bean. "Aerodynamic design of the Boeing YC-14 advanced medium STOL transport". AIAA 75-1015. 1975 (see p. 7).

[103] J. D. McLean et al. “Study of the Application of Separation Control by Unsteady Excitation to Civil Transport Aircraft”. NASA/CR-1999-209338. 1999 (see p. 20).

[104] E. T. Meleason. “Effects of nozzle design and power on cruise drag”. NASA-SP-406. 1976 (see p. 8).

[105] LT. P. Melton, N. W. Schaeffler, and C.-S. Yao. “Active Control of Flow Separation from Supercritical Airfoil Leading-Edge Flap Shoulder”. In: *AIAA Journal of Aircraft* 42.5 (2005) (see pp. 17, 94).

[106] F. R. Menter. “Two-Equation Eddy-Viscosity Turbulence Models for Engineering Applications”. In: *AIAA Journal* 32.8 (1994), pp. 1598–1905 (see pp. 34, 42).

[107] M. Meunier. “Simulation and Optimization of Flow Control Strategies for Novel High-Lift Configurations”. In: *AIAA Journal* 47.5 (May 2009). DOI: 10.2514/1.38245 (see p. 9).

[108] W. E. Milholen et al. “High-Reynolds number circulation control testing in the national transonic facility (Invited)”. In: *50th AIAA Aerospace Sciences Meeting*. AIAA 2012-0103. Nashville, TN, USA, 2012 (see p. 9).

[109] J. B. de la Montanya and D. D. Marshall. “Circulation Control and Its Application to Extreme Short Take-Off and Landing Vehicles”. In: *45th AIAA Aerospace Sciences Meeting and Exhibit*. AIAA 2007-1404. Reno, NV, USA, 2007 (see p. 19).

[110] S. Munro, K. Ahuja, and R. Englar. “Noise Reduction Through Circulation Control Technology”. In: *39th Aerospace Sciences Meeting and Exhibit*. AIAA Paper 2001-0666. Reno, NV, USA, 2001 (see p. 10).

[111] S. Munro and K. K. Ahuja. “Aeroacoustics of a High Aspect-Ratio Jet”. In: *9th AIAA/CEAS Aeroacoustics Conference and Exhibit*. AIAA paper 2003-3323. Hilton Head, SC, USA, 2003 (see p. 10).

[112] S. Munro and K. K. Ahuja. “Development of a Prediction Scheme for Noise of High-Aspect Ratio Jets”. In: *9th AIAA/CEAS Aeroacoustics Conference and Exhibit*. AIAA paper 2003-3255. Hilton Head, SC, USA, 2003 (see p. 10).

[113] S. Munro and K. K. Ahuja. “Fluid Dynamics of a High Aspect-Ratio Jet”. In: *9th AIAA/CEAS Aeroacoustics Conference and Exhibit*. AIAA paper 2003-3129. Hilton Head, SC, USA, 2003 (see p. 10).

[114] T. C. Nark. "Design, development and flight evaluation of the Boeing YC-14 USB powered lift aircraft". Tech. rep. AGARD CP 515. Boeing Defense & Space Group, 1993 (see p. 7).

[115] "NASA blueprint strategic vision 2013". In: *NASA Whitepaper* (2012). URL: `http://www.aeronautics.nasa.gov/pdf/armd_strategic_vision_2013.pdf(2013)` (see p. 1).

[116] B. G. Newman. "The deflection of plane jets by adjacent boundaries - Coanda effect". In: *Boundary Layer and Flow Control. Its Principles and Application.* Ed. by G. V. Lachmann. Vol. 1. Pergamon Press, New York, 1961, pp. 232 –264 (see p. 21).

[117] R. H. Nichols. "Algorithm and turbulence model requirements for simulating vortical flows". AIAA 2008-337. 2008 (see p. 11).

[118] J. N. Nielsen and J. C. Bigger. "Recent progress in circulation control aerodynamics". In: *25th AIAA Aerospace Sciences Meeting.* AIAA Paper 87-001. Reno, NV, USA, 1987 (see p. 1).

[119] T. Nishino, S. Hahn, and K. Shariff. "Calculation of the Turbulence Characteristics of Flow Around a Circulation Control Airfoil Using LES (Invited Paper)". In: *In 48th AIAA Aerospace Sciences Meeting Including the New Horizons Forum and Aerospace Exposition, Aerospace Sciences Meetings.* AIAA 2010-347. Orlando, FL, USA, 2010 (see p. 13).

[120] T. Nishino and K. Shariff. "Numerical Study of Wind-Tunnel Sidewall Effects on Circulation Control Airfoil Flows". In: *AIAA Journal* 48.9 (2010), pp. 2123–2132 (see p. 13).

[121] B. Nishri and I. Wygnanski. "Effects of Periodic Excitation on Turbulent Flow Separation from a Flap". In: *AIAA Journal* 36.4 (April 1998). DOI: `10.2514/2428` (see pp. 16, 94).

[122] B. Norton. "Boeing C-17 Globemaster III". Speciality Press. ISBN 1-58007-061-2. 2001 (see p. 7).

[123] C. J. Novak and K. C. Cornelius. "An LDV investigation of a circulation control airfoil flowfield". In: *AIAA 24th Aerospace Sciences Meeting.* AIAA 86-0503. Reno, NV, USA, 1986 (see p. 10).

[124] C. J. Novak, K. C. Cornelius, and R. K. Roads. "Experimental investigations of the circular wall jet on a circulation control airfoil". In: *AIAA 25th Aerospace Sciences Meeting.* AIAA 87-0155. Reno, NV, USA, 1987 (see p. 10).

[125] D. Oster et al. “The effects of initial condition on the two-dimensional, turbulent mixing layer.” In: *Structure and mechanics of turbulence. Lecture Notes in Physics*. Ed. by H. Fiedler. Vol. 75. Springer, Berlin, 1978, pp. 48–64 (see p. 87).

[126] T. Oyler and W. Palmer. “Exploratory Investigation of Pulse Blowing for Boundary Layer Control”. In: *North American Rockwell Report* (1972). NR72H-12 (see p. 16).

[127] P. Pajayakrit and R. J. Kind. “Assessment and Modification of Two-Equation Turbulence Models”. In: *AIAA Journal* 38.6 (2000), pp. 955–963 (see p. 11).

[128] K. Paschal et al. “Circulation Control Model Experimental Database for CFD Validation”. In: *50th AIAA Aerospace Sciences Meeting*. AIAA 2012-0705. Nashville, TN, USA, 2012 (see p. 12).

[129] R. Petz and W. Nitsche. “Active separation control on the flap of a two-dimensional generic high-lift configuration”. In: *AIAA Journal of Aircraft* 44.3 (2007), pp. 865–874 (see pp. 17, 18, 94).

[130] K. C. Pfingsten, R. D. Cecora, and R. Radespiel. “An Experimental Investigation of a Gapless High-Lift System Using Circulation Control”. In: *CEAS/KATnet II Conference*. Bremen, Germany, 2009 (see pp. 2, 41, 42, 44).

[131] K. C. Pfingsten et al. “Numerical Simulation of the Flow Around Circulation Control Airfoils”. In: *First CEAS European Air and Space Conference*. Berlin, Germany, 2007 (see p. 36).

[132] K. C. Pfingsten and R. Radespiel. “Experimental and numerical investigation of a circulation control airfoil”. In: *47th AIAA Aerospace Sciences Meeting Including The New Horizons Forum and Aerospace Exposition*. AIAA 2009-0533. Orlando, FL, USA, 2009 (see pp. 14, 24, 41).

[133] K. C. Pfingsten, R. Radespiel, and M. Kamruzzaman. “Use of Upper Surface Blowing and Circulation Control for Gapless High Lift Configurations”. In: *CEAS/KATnet Conference on Key Aerodynamic Technologies*. Bremen, Germany, 2005 (see p. 8).

[134] P. Poisson-Quinton and L. Lepage. “Survey of French research on the control of boundary layer and circulation”. In: *Boundary Layer and Flow Control. Its Principles and Application.* Ed. by G. V. Lachmann. Vol. 1. Pergamon Press, New York, 1961, pp. 21–73 (see pp. 5, 6, 20, 21).

[135] M. Pott-Pollenske, J. Alvarez-Gonzalez, and W. Dobrzynski. "Effect of Slat Gap on Farfield Radiated Noise and Correlation with Local Flow Characteristics". In: *9th AIAA/CEAS Aeroacoustics Conference*. AIAA 2003-3228. Hilton Head, SC, USA, 2003 (see p. 1).

[136] M. Pott-Pollenske and K. C. Pfingsten. "Aeroacoustic Performance of an Airfoil with Circulation Control". In: *16th AIAA/CEAS Aeroacoustics Conference* (2009). DOI: 10.2514/6.2010-3881 (see p. 10).

[137] M. Pott-Pollenske et al. "Slat Noise Reduction by means of Adaptive Leading-Edge Devices". In: *Aircraft Noise Reduction by Flow Control and Active/Adaptive Techniques*. Vilnius, Litauen, 2014 (see pp. 15, 49).

[138] L. Prandtl. "Über Flüssigkeitsbewegung bei sehr kleiner Reibung". In: *Proceedings of the Third International Mathematical Congress*. Heidelberg, Germany, 1904, pp. 484–491 (see p. 4).

[139] L. Prandtl. "The Generation of Vortices in Fluids of Small Viscosity". In: *Journal of the Royal Aeronautical Society* 31 (1927) (see p. 4).

[140] A. Probst. "Reynoldsspannungsmodellierung für das Überziehen in der Flugzeugaerodynamik". Doctoral dissertation at Institut of Fluid Mechanics, Technische Universität Braunschweig. 2013 (see p. 36).

[141] S. Queen and J. Cochrane. "Quiet Short-Haul Research Aircraft joint navy/NASA sea trials". In: *AIAA Journal of Aircraft* 19.8 (1982) (see p. 7).

[142] R. Radespiel and W. Heinze. "SFB 880: fundamentals of high lift for future commercial aircraft". In: *CEAS Aeronautical Journal* 5.3 (2014), pp. 239–251 (see pp. 19, 20).

[143] R. Radespiel, K.-C. Pfingsten, and C. Jensch. "Flow Analysis of Augmented High-Lift Systems". In: *Notes on Numerical Fluid Mechanics and Multidisciplinary Design*. Ed. by R. Radespiel, C.-C. Rossow, and B. W. Brinkmann. Vol. 102. Springer, 2007, pp. 168–189 (see p. 20).

[144] A. Raspet, J. D. Cornish, and G. D. Bryant. "Delay of the stall by suction through distributed perforations". In: *Aeronautical Engineering Review* 15.8 (1956) (see p. 6).

[145] D. P. Raymer. "Aircraft design: a conceptual approach". In: *AIAA Educational Series* (1999) (see p. 51).

[146] O. Reynolds. “An experimental invstigation of the circumstances which determine whether the motion of water shall be direct and sinuous, and the law of resistance in parallel channels”. In: *Phylosophical Transactions of the Royal Society* 174 (1883) (see p. 29).

[147] L. F. Richardson. “The approximate arithmetical solution by finite differences of physical problems including differential equations, with an application to the stresses in a masonry dam”. In: *Philosophical Transactions of the Royal Society* (1911). DOI: 10.1098/rsta.1911.0009 (see p. 39).

[148] L. F. Richardson and J. A. Gaunt. “The Deferred Approach to the limit”. In: *Phylosophical Transactions of the Royal Society* (1927). DOI: 10.1098/rsta.1927.0008 (see p. 39).

[149] A. Rudenko, H. P. Monner, and M. Rose. “A Process Chain for Structural Optimization of a Smart Droop Nose for an Active Blown High Lift System”. In: *22nd AIAA/ASME/AHS Adaptive Sctructures Conference*. Washington DC, USA, 2014 (see p. 14).

[150] C. L. Rumsey, T. B. Gatski, and J. H. Morrison. “Turbulence Model Predictions of Strongly Curved Flow in a U-Duct”. In: *AIAA Journal* 38.8 (2000) (see p. 11).

[151] C. L. Rumsey and T. Nishino. “Numerical study comparing RANS and LES approaches on a circulation control airfoil”. In: *International Journal of Heat and Fluid Flow* 32.5 (2011), 847–864 (see p. 13).

[152] C. L. Rumsey and R. C. Swanson. “Turbulence modelling for active flow control applications”. In: *International Journal of Computational Fluid Dynamics* 23.4 (Apr- May 2009). DOI: 10.1080/10618560902776794 (see pp. 12, 44).

[153] M. Salikuddin, W. H. Brown, and K. K. Ahuja. “Noise from a circulation control wing with upper surface blowing”. AIAA 85-3083. 1985 (see p. 8).

[154] K. Sawada and S. Takanashi. “A numerical investigation on wing/nacelle interferences of usb configuration”. AIAA 87-0455. 1987 (see p. 8).

[155] M. Schildknecht, J. A. Miller, and G. E. A. Meier. “The influence of suction on the structure of turbulence in fully developed pipe flow”. In: *Journal of Fluid Mechanics* 90.01 (1979), pp. 67–107. DOI: 10.1017/S0022112079002081 (see p. 7).

[156] H. Schlichting. “Boundary-layer theory”. Ed. by Mc-Graw Hill Publications. New York, 1960 (see p. 4).

[157] M. Schmalzel, P. Varghese, and I. Wygnanski. “Steady and Oscillatory Flow Control Tests for Tilt Rotor Aircraft”. In: *Active Flow Control*. Ed. by R. King. Vol. 95. Springer, Berlin, 2006, pp. 190–207 (see p. 9).

[158] A. Schmitz and P. Horst. “Numerical mdelling of the change in stiffness properties of cross-ply laminates subjected to large bending curvatures”. In: *Key Engineering Materials* 577-578 (2013), pp. 173–176 (see p. 14).

[159] A. Schmitz and P. Horst. “A finite element unit-cell method for homogenised mechanical properties of heterogeneous plates”. In: *Composites Part A: Applied Science and Manufacturing* 61 (2014), pp. 23–32 (see p. 14).

[160] A. Schmitz and P. Horst. “Bending deformation limits of corrugated unidirectionally reinforced composites”. In: *Composite Structures* 107 (2014), pp. 103–111 (see p. 14).

[161] P. Scholz et al. “Influencing the Mixing Process in a Turbulent Boundary Layer by Pulsed Jet Actuators”. In: *Notes on Numerical Fluid Mechanics and Multidisciplinary Design*. Ed. by H. J. Rath et al. Vol. 92. Springer, 2006, pp. 265–272 (see p. 18).

[162] P. Scholz et al. “Leading-Edge Separation Control by Means of Pulsed Vortex Jets”. In: *AIAA Journal* 46.4 (2008), pp. 837–846 (see p. 18).

[163] P. Scholz et al. “Active Control of Leading-Edge Separation within the German Flow Control Network”. In: *47th AIAA Aerospace Sciences Meeting*. Orlando, FL, USA, 2009 (see p. 18).

[164] O. Schrenk. “Versuche mit einem Absaugeflügel”. In: *Zeitschrift für Flugtechnik und Motorluftschiffahrt* 22 (1931) (see p. 4).

[165] O. Schrenk. “Grenzschichtabsaugung und Senkenwirkung”. In: *Zeitschrift für angewandte Mathematik und Mechanik* 13 (1933) (see p. 5).

[166] O. Schrenk. “Grenzschichtabsaugung”. In: *Luftwissen* 7 (1940) (see p. 5).

[167] D. Schwamborn, T. Gerhold, and R. Heinrich. “The DLR TAU-Code: Recent Applications in Research and Industry”. In: *ECCOMAS CFD*. Egmond aan Zee, The Netherlands, 2006 (see p. 36).

[168] F. Schwarz and W. Wuest. "Flugversuche am Baumuster Do 27 mit Grenzschichtabsaugung zur Steigerung des Höchstauftriebs". Forschungsbericht Nr. 63-02, Aerodynamische Versuchsanstalt Göttingen. 1963 (see p. 7).

[169] W. Schwier. "Auftriebsänderung Durch einen auf der Flügeldruckseite Ausgeblasene Luftstrahl". 1944. DOI: UM31912 (see p. 5).

[170] A. Seifert, A. Darabi, and I. Wygnanski. "Delay of Airfoil Stall by Periodic Excitation". In: *AIAA Journal of Aircraft* 33.4 (1996). DOI: 10.2514/3.47003 (see pp. 15, 16, 94).

[171] A. Shmilovic and Y. Yadlin. "Flow control techniques for transport aircraft". In: *AIAA Journal* 49 (2011), pp. 489–502 (see p. 14).

[172] A. Shmilovic and Z. Yadlin. "Flow control for the systematic buildup of high lift systems". In: *AIAA Journal of Aircraft* 45.5 (2008) (see pp. 14, 18, 94).

[173] M. D. Shovlin. "Effects of inlet airframe integration on the inlet of a usb four engine STOL airplane". AIAA 78-959. 1978 (see p. 8).

[174] M. L. Shur et al. "Turbulence Modeling in Rotating and Curved Channels: Assessing the Spalart – Shur Correction". In: *AIAA Journal* 38.5 (2000). DOI: 10.2514/2.1058 (see pp. 11, 33, 36).

[175] R. L. Simpson. "Turbulent boundary layer separation". In: *Annual Review of Fluid Mechanics* 21 (1989), pp. 205–234 (see p. 4).

[176] R. L. Simpson. "Aspects of turbulent boundary layer separation". In: *Progress in Aerospace Sciences* 32.5 (1996), pp. 457–521 (see p. 4).

[177] J. F. Slomski et al. "Numerical Simulation of Circulation Control Airfoils as Affected by Different Turbulence Models". In: *40th AIAA Aerospace Sciences Meeting and Exhibit*. AIAA paper 2002-0851. Reno, NV, USA, 2002 (see p. 11).

[178] P. R. Spalart and S. R. Allmaras. "A One-Equation Turbulence Model for Aerodynamic Flows". In: *30th Aerospace Sciences Meeting and Exhibit*. AIAA 92-0439. Reno, NV, USA, 1992 (see pp. 32, 36, 42).

[179] P. R. Spalart and M. Schur. "On the Sensitization of Turbulence Models to Rotation and Curvature". In: *Aerospace Science and Technology* 1.5 (1997), 297–302. DOI: 10.1016/S1270-9638(97)90051-1 (see pp. 11, 33, 36, 42).

[180] G. G. Stokes. "On the Theories of Internal Friction of Fluids in Motion". In: *Transactions of the Cambridge Philosophical Society* 8 (1845) (see p. 28).

[181] J. Stüper. "Flugerfahrungen und Messungen an zwei Absaugeflugzeugen". Forschungsbericht Nr. 1821, Zentrale für Wissenschaftliches Berichtswesen der Luftfahrtforschung des Generalluftzeugmeisters (ZWB), Berlin-Adlershof (see p. 5).

[182] J. Stüper. "Entwiklung eines Absaugeflugzeugs und erste Flugmessungen". Bericht der Lilienthal-Gesellschaft Nr. 099/006. 1938 (see p. 5).

[183] J. Stüper. "Flight Experiences and tests on two airplanes with suction slots". In: *NACA Technical Memorandum* (1950). NACA TM 1232 (see p. 5).

[184] M. B. Sussman et al. "USB environment assessment based on YC-14 flight test measurements". AIAA 77-593. 1977 (see p. 7).

[185] R. C. Swanson and C. L. Rumsey. "Numerical Issues for Circulation Control Calculations". In: *3rd AIAA Flow Control Conference*. AIAA 2006-3008. San Francisco, CA, USA, 2006 (see pp. 11, 42).

[186] R. C. Swanson and C. L. Rumsey. "Computation of circulation control airfoil flows". In: *Computers & Fluids* 38.10 (2009), pp. 1925–1942 (see p. 13).

[187] Y. Tanaka. "Search and rescue amphibious aircraft in Japan". In: *Advanced Marine Vehicles Conference*. 89-1500-CP. Arlington, VA, USA, 1989 (see p. 7).

[188] D. P. Telionis. "Review - Unsteady boundary layers, separated and attached". In: *ASME Journal of Fluids Engineering* 101.1 (1979), pp. 29–43. DOI: 10.1115/1.3448732 (see p. 3).

[189] J. Thiemeier. "Numerische Untersuchung des 3D-Abreißsverhaltens eines Verkehrsflugzeugs mit Coanda-Klappe und formvariabler Vorderkante". Master thesis at Institut of Fluid Mechanics, Technische Universität Braunschweig. 2014 (see pp. 67–69).

[190] F. Thomas. "Untersuchungen uber die Grenzschichtbeeinflussung durch Ausblasen zur Erhohung des Auftriebes". Doctoral dissertation at Institut of Fluid Mechanics, Technische Universität Braunschweig. 1962 (see p. 20).

[191] V. Togiti et al. “Numerical Simulation of Steady Blowing Active Flow Control Using a Differential Reynolds Stress Model”. In: *CEAS/KATnet II*. Bremen, Germany, 2009 (see p. 13).

[192] E. Turkel, R. Radespiel, and N. Kroll. “Assessment of preconditioning methods for multidimensional aerodynamics”. In: *Computers & Fluids* (1997). DOI: 10.1016/S0045-7930(97)00013-3 (see p. 39).

[193] R. E. Walters, D. P. Myer, and D. J. Holt. “Circulation Control by Steady and Pulsed Blowing for a Cambered Elliptical Airfoil”. West Virginia University, Aerospace Engineering. TR-32. 1972 (see p. 16).

[194] A. Walz and F. Ehlers. “Experimental Profile Investigations with Boundary Layer Control”. In: *AVA Monographs (E7)* (1947). Ed. by London Ministry of Supply (see p. 5).

[195] T. Wang. “Upper surface blown powered lift system for aircraft”. United States Patent 4447028. 1984 (see p. 7).

[196] M. Waters et al. “Propulsion system modeling and takeoff distance calculations for a powered-lift aircraft with circulation-control wing aerodynamics”. AIAA 2009-1258. 2009 (see p. 19).

[197] K. A. Weinman. “Vortical Modeling in the DLR TAU Code”. In: *Notes on Numerical Fluid Mechanics and Multidisciplinary Design*. Ed. by A. Dillmann et al. Vol. 121. Springer, 2013, pp. 439–446 (see p. 11).

[198] T. W. Weiss and W. Heinze. “Multidisciplinary Design of a CESTOL Aircraft with Powered Lift System”. In: *SFB 880 - Fundamentals of High-Lift for Future Commercial Aircraft, Biennial Report*. Ed. by R. Radespiel and R. Semaan. Braunschweig, Germany, 2013 (see p. 67).

[199] O. D. Wells et al. “Wind tunnel and analytical investigation of over-the-wing propulsion / air frame interferences for a short-haul aircraft at Mach numbers from 0.6 to 0.78”. NASA CR-2905. 1977 (see p. 8).

[200] C. Werner-Spatz et al. “Multidisciplinary conceptual design for aircraft with circulation control high-lift systems”. In: *CEAS Aeronautical Journal* 3.2 (2012), pp. 145–164 (see p. 19).

[201] D. C. Wilcox. “Reassessment of Scale-Determining Equation for Advanced Turbulence Models”. In: *AIAA Journal* 26.11 (1988), pp. 1299–1310 (see p. 11).

[202] D. C. Wilcox. “Turbulence modeling for CFD”. Ed. by Inc. DCW Industries. California, USA: La Canada, 1993 (see pp. 31, 33, 36).

[203] D. C. Wilcox. "Multiscale Model for Turbulent Flows". In: *AIAAJournal* 26.11 (1998), pp. 1311–1320 (see p. 11).

[204] J. Wild. "Mach and Reynolds number dependencies of the stall behavior of high-lift wing sections". In: *AIAA Journal of Aircraft* 50.4 (2013), pp. 1202–1216 (see pp. 14, 15, 55).

[205] J. Wild et al. "Large scale separation flow control experiments within the German Flow Control Network". In: *47th AIAA Aerospace Sciences Meeting Including The New Horizons Forum and Aerospace Exposition.* AIAA 2009-530-249. Orlando, FL, USA, 2009 (see p. 18).

[206] J. Williams. "A brief history of British research on boundary layer control for high lift". In: *Boundary Layer and Flow Control. Its Principles and Application.* Ed. by G. V. Lachmann. Vol. 1. Pergamon Press, New York, 1961, pp. 74–103 (see p. 5).

[207] A. Wöckner. "Zu der Entwicklung des Absaugeflugzeuges". In: *Bericht der Lilienthal-Gesellschaft 099/006* (1938) (see p. 5).

[208] H. Yamato, N. Okada, and T. Bando. "Flight test of the Japanese USB STOL experimental aircraft ASKA". AIAA 88-2180. 1988 (see p. 7).

[209] H. Yamato, N. Okada, and T. Bando. "Flight test of the japanese upper surface blowing STOL experimental aircraft ASKA". In: *AIAA Journal of Aircraft* 28.10 (1991) (see p. 7).

[210] Z. Y. Yang and P. R. Voke. "Large-eddy simulation of boundary-layer separation and transition at a change of surface curvature". In: *Journal of Fluid Mechanics* 439 (2001), pp. 305–333 (see p. 13).

[211] S. Ying et al. "Investigation of Confluent Boundary Layers in High-Lift Flows". In: *AIAA Journal of Aircraft* 36.3 (1999). DOI: 10.2514/2.2490 (see pp. 15, 66).

[212] K. B. M. Q. Zaman and A. K. M. F. Hussain. "Turbulence Suppression in Free Shear Flows by Controlled Excitation". In: *Journal of Fluid Machanics* 103 (1981), pp. 133–159 (see p. 16).

[213] G.-C. Zha et al. "Effect of injection slot size on the performance of coflow jet airfoil". In: *AIAA Journal of Aircraft* 43.4 (2006) (see p. 8).

[214] G.-C. Zha et al. "High performance airfoil using co-flow jet flow control". In: *AIAA Journal* 45.8 (2007) (see p. 8).